Catalytic microchannel reactor development for the removal of carbon monoxide from hydrogen-rich gas streams

KC Musavuli

orcid.org/ 0000-0002-8863-7721

Dissertation accepted in fulfilment of the requirements for the degree *Master of Science in Engineering Sciences with Chemical Engineering* at the North West University

Supervisor:	Mr. N Engelbrecht
Co-Supervisor:	Prof. RC Everson
Co-Supervisor:	Prof. DG Bessarabov

Graduation:	June 2021
Student number:	31685757

DECLARATION

I, Kyatsinge Cédric Musavuli, hereby declare that the dissertation entitled: "***Catalytic microchannel reactor development for the removal of carbon monoxide from hydrogen-rich gas streams*",** submitted in fulfilment of the requirements for the degree Master of Science in Chemical Engineering, is my own work, except where acknowledged in the text, and has not been submitted to any other tertiary institution in whole or in part.

Signed at North-West University (Potchefstroom Campus)

_____ _____

ACKNOWLEDGEMENTS

This project could not be done without the help and support of persons who contributed directly or indirectly to its completion. To all of them, I would like to extend my deepest gratitude.

First, I would like to thank God almighty for all the graces bestowed from the beginning of my life to this very day. Without him, I would do nothing.

My sincere gratitude also goes to my inspiring supervisors for their numerous encouragements and the priceless lessons learned during the course of the project.

- To Mr. Nicolaas Engelbrecht for his incredible kindness and his presence when I needed urgent assistance with administrative formalities, equipment set-up, clarifications on project-related questions and introduction to CFD modelling.
- To Prof. Raymond Everson, for his amazing patience, determination, perseverance and insightful ideas shared during the very productive weekly meetings. The lessons I learned during the many meetings show me the path to follow in order to be a researcher.
- To Prof. Dmitri Bessarabov, for giving me the honour to be part of the HySA NWU research team and for always ensuring that all the technical and administrative conditions for good progress of this project was met.

Many thanks to the people who assisted me with their expertise in special tasks that were critical in the evolution of the project. Here, I would like to acknowledge the help of Prof. Andrei Kolesnikov (Tshwane University of Technology), for many tips and precious advices CFD on COMSOL; Dr. Gerrit Grobler for assistance during the parameter optimization and goodness of fit calculations; Dr. Frikkie Conradie ensuring the availability of COMSOL software; Ted Paarlberg for technical assistance regarding the apparatus, Mr. Phillimon Modisha for his help during TPR.

To Lara Kroeze, Tony Morgado and Dr. Neels le Roux, I would like to express my thankfulness for the support in all administrative formalities.

I would like to thank my former supervisor, Prof. Hilary Rutto; and colleagues, Jean-Claude Banza and Pascal. Mwenge, from the Vaal University of Technology for showing me the benefit of doing scientific research and without whom I would probably not be pursuing my postgraduate studies.

My gratitude extends to all friends and colleagues at the NWU, whose attitude, priceless advices, words of encouragements and various help gave me mental strength and support during this project. Special thanks to Prof. Frik van Niekerk, Faan du Preez, Patrick Sekoai, Cecil Ouma, Kingsley Obodo, Boitumelo Mogwase, Marina du Toit, Rudaviro Garidzirai, Gerhard Human, Faan Oelofse, Alexander Malakhov, Alina Kuzokhova, Henning Buitendach, Ashleigh Townsend, Leandri Vermaak, Renier Potgieter, Carel Minnaar, Christiaan Martinson, Maha Rhandi, Pieter van Niekerk, Sam Modise, Sam Mamathuntsha, Ivan Mavinjwa, Marc Yorinda, Celina Cachucho, Franck Muteba.

Last but not least, I would like to express my gratitude to my family members, Pontien M. Muhindo, Yolande K. Muhugho, Landry Mbale, Rose & Rosine Lwanzo, Gracia Lukogho, Mercy, Ignatius and Ignatia Mapothoma for their immense emotional support throughout the project.

Mentioning all the people who positively contributed to the completion of this project would fill an entire book. To all unmentioned contributors, I would like to say *thank you!*

ABSTRACT

Currently, hydrogen (H_2) fuel cells are among the fastest emerging clean power generation technologies worldwide. The emergence of H_2 energy and fuel cells for power generation originates from the renewable energy sector, and the storage of renewable energy in the form of a chemical energy carrier to provide power grid balancing. At the moment, H_2 production is still dominated by fossil fuel processing, leading to carbon-based impurities such as carbon monoxide (CO) in the H_2 streams—which is known to deactivate fuel cell anode catalysts. Selective methanation and preferential oxidation of CO are two common methods of catalytic CO removal from H_2-rich gas streams.

In this work, three of the most popular catalysts used for CO abatement (Ni-Pt/Al_2O_3, Au/Al_2O_3, and Ru-Cs/Al_2O_3) were tested for their ability to remove ca. 1.4 vol.% CO from a synthetic H_2-rich gas stream. Stainless steel microchannel reactors, containing the three respective washcoated catalysts, were used during the experimental work. Due to micro-scale dimensions of the channels, limit gas diffusional effects were expected, with the channels providing close contact between the bulk gas phase and the catalytic layer. Experiments were conducted isothermally at reaction temperatures of 80–400°C (depending on the CO abatement reaction applied), and space velocities of 32.6–130.4 $NL.g_{cat}^{-1}.h^{-1}$. The Ru-Cs/Al_2O_3 catalyst was found to be the most suitable catalyst. CO concentrations lower than 100ppm were obtained via CO preferential oxidation at reaction temperatures of 120–180°C, with a peak CO conversions of more than 99.7% at 120–140°C and space velocities of 65.2–97.8 $NL.g_{cat}^{-1}.h^{-1}$. This corresponds to CO levels as low as 42 ppm in the product gas. The conversion of H_2 did not exceed 6.5%.

Additionally, the inability to characterise the dynamic region and the transport phenomena within the microchannels led to a theoretical study of the preferential CO oxidation process. A full three-dimensional model (using COMSOL Multiphysics® V4.4 software) showed that CO oxidation was the dominant reaction in a temperature range of 80–160°C. At temperatures above 160°C, the effects of the RWGS reaction was more pronounced, leading to a noticeable decrease in the CO conversion. Kinetic approximations were used to validate the reactor model to the full set of experimental data, and the model fit was noticed to yield accurate approximations of CO conversion in the simulated microchannel reactor over the range of reaction parameters.

It has been demonstrated that microchannel reactor technology is suitable for CO removal from H_2-rich gas streams by preferential oxidation, at relatively low reaction temperatures (below 200°C) and high gas throughput compared to the reactor's physical size. H_2 originating from fossil or bio-based processes can be successfully treated to near complete CO purification standards, before fuel cell technology is applied for power generation purposes.

Keywords: Microchannel reactor, selective methanation, preferential oxidation, Ru/Al_2O_3 catalyst, Computational Fluid Dynamics (CFD) modelling, kinetic parameter estimation.

TABLE OF CONTENTS

LIST OF TABLES

LIST OF FIGURES

LIST OF SYMBOLS

Abbreviations

BACAS	Belgian Academy of Applied Sciences
CFD	Computational Fluid Dynamics
CO_x	Carbon oxides
EUR	Euro
g_{cat}	Gram of catalyst
HID	Helium ionisation detector
IEA	International Energy Agency
IRENA	International Renewable Energy Agency
ISO	International Organization for Standardization
NO_x	Nitrogen oxides
PEM	Proton exchange membrane
PEMFC	Proton exchange membrane fuel cell
ppm	Part per million
PROX	Preferential oxidation
PSA	Pressure swing adsorption
RWGS	Reverse water gas shift
SELMET	Selective methanation
SO_x	Sulfur oxides
TCD	Thermal conductivity detector
USD	United States dollar
vol.%	Volume percent
WGS	Water gas shift
wt.%	Weight percent

Nomenclature

a, b, c	Orders of reaction
C_F	Forchheimer drag coefficient
C_i	Molar concentration of species i in the mixture, $mol.m^{-3}$
D_{ij}	Binary diffusion coefficient of species i in species j, $m^2.s^{-1}$
$D_{ij\ eff}$	Effective binary diffusion coefficient of species i in species j, $m^2.s^{-1}$
e	Residuals between calculated experimental CO conversions
E	Activation energy, $kJ.mol^{-1}$
F_i	Volumetric flow rate of species i, $m^3.s^{-1}$
k	Thermal conductivity, $W.m^{-1}.K^{-1}$
K_1, K_2, K_3	Equilibrium constants

k_i	Reaction rate pre-exponential constant of reaction *i*
K_i	Adsorption constant of component *i*, $m^3.mol^{-1}$
M	Mean molar mass, $kg.mol^{-1}$
Ma	Mack Mach number
M_i	Molar mass of species *i*, $kg.mol^{-1}$
n	Vector normal to the symmetry plane
N_i	Number of moles of species *i*
P	Pressure, Pa
P_{atm}	Atmospheric pressure, Pa
P_i	Partial pressure of species *i*, Pa
R	Universal gas constant, $Pa.m^3.mol^{-1}.K^{-1}$
r	Rate of reaction, $mol.m^{-3}.s^{-1}$
R_r	Rate of reaction, $mol.kg^{-1}.s^{-1}$
S_{CO}	Selectivity towards CO conversion, %
T	Temperature, K
T_o	Reference temperature, K
u	Linear velocity, $m.s^{-1}$
X_{CO}	CO conversion, %
$X_{g,h}$	CO conversions at temperature *g* and flow rate *h*, %
ΔH	Enthalpy of reaction, $kJ.mol^{-1}$
ΔH_i	Adsorption enthalpy of species *i*, $kJ.mol^{-1}$

Greek symbols

α	Significance level, used in the F-test
ε	Porosity of the catalyst
κ	Permeability of the catalyst, m^2
λ	Oxygen excess factor ($2N_{O_2}/N_{CO}$)
ρ	Gas density, $kg.m^{-3}$
ρ_s	Solid catalyst density, $kg.m^{-3}$
θ	Parameters used during optimization
μ	Viscosity, Pa.s
v_i	Atomic volume of species *i*, $cm^3.mol^{-1}$
ω_i	Weight fraction of species *i*, $cm^3.mol^{-1}$

Subscripts

g	Number of temperatures used in the model (1, 2, …,6)
h	Number flow rates used in the model (1, …, 4)
i, j	Component *i* or *j*
in	Reactor inlet
out	Reactor outlet
wall	Reactor wall

CHAPTER 1. INTRODUCTION

1.1. Background

The rise in the global population, technological development and higher living standards are expected to increase energy production and consumption worldwide in the near to mid-term (BP, 2017:5–6; Midilli *et al.*, 2005:256). The current manner of energy production from fossil fuel has led to several environmental costs with regard to air pollution (CO_2, CH_4, CO, NO_x, SO_x, O_3, particulates, etc.), leading to global warming as well as many health-related problems (Chauhan & Singh, 2015:63). The global increased energy consumption also led to the accelerated depletion of fossil fuel resources. At the current consumption rate, oil and natural gas are likely to be exhausted before the end of the 21st century (Shafiee & Topal, 2009:186). As a consequence, increases in the cost of energy might generate energy conflicts around the world. A shift to renewable energy is therefore crucial for energy security and sustainability (Midilli *et al.*, 2005:256).

Several renewable energy alternatives already exist. They include hydropower, geothermal, solar, wind energy and biomass. Some of these sources (e.g. solar and wind) are considered intermittent and unpredictable. An exciting prospect is the storage of excess renewable energy when the supply surpasses the demand, and use thereof when the supply is limited (Edwards *et al.*, 2008:4356–4357). On the other hand, biofuels derived from renewables (biodiesel, bioethanol and biogas) have great potential, at least in the transport sector, but have their round trip energy efficiencies limited by the Carnot efficiency of combustion engines, similar to fuels derived from fossil resources (Chunshan, 2010:10). A promising solution to these problems exists in using hydrogen (H_2) as a clean fuel. Instead of the usual direct fuel combustion, H_2 can be used in a fuel cell where it is electrochemically bonded with oxygen (O_2) to produce electricity and pure water (H_2O) as a by-product. Health, as well as environmental benefits will be gained since the H_2 fuel cell releases no CO_x, NO_x, SO_x or particulates. Edwards *et al.* (2008:4358) stated that H_2 fuel cells operate at higher efficiencies (50–65%) than conventional combustion engines fed with fossil fuels, which have efficiencies of around 25%. When heat generated in fuel cells is used in combined heat and power systems, the efficiency can rise up to 85% (Edwards *et al.*, 2008:4358). On the other hand, depending on the fuel cell technology applied, the quality of heat is also a factor to consider.

Today, a significant portion of H_2 (ca. 95% of total global H_2 production) is still produced from fossil fuels. Fossil fuel processing techniques, including steam reforming, partial oxidation, and autothermal reforming (Moharana *et al.*, 2009:1–2), take advantage of the economy of scale and established infrastructure for large-scale H_2 production (Edwards *et al*., 2008:4357). Unprocessed non-renewable H_2 comes with several major impurities which can include: CO, CO_2, N_2, CH_4, and small amounts of nitrous and sulphurous compounds. Impurities such as nitrous, sulphurous and CO gas have devastating effects on fuel cell performance, especially low temperature proton exchange membrane fuel cells (PEMFC). CO is especially known to decrease the durability of fuel cells by occupying Pt active sites on the catalyst surface, thus reducing the electrochemically-active surface area of the fuel cell anode (Qi *et al.*,2002:239).

In order to reduce the amount of CO in the H_2 stream to acceptable levels of 10 ppm or 100 ppm for Pt and higher CO-tolerant Pt-Ru anodes, respectively (Mohaideen *et al.*, 2015:8). Mishra & Prasad (2011:2) suggested that the most well-known CO clean-up technologies include: Pressure Swing Adsorption (PSA), membrane separation, CO selective methanation (SELMET) and CO preferential oxidation (PROX). PSA and membrane separation are very selective processes and perform well for H_2 purification. PSA is also well established for industrial scale operations. H_2 embrittlement and high cost are the foremost challenges encountered in pressurised membrane separation processes, while electrochemical membrane separation is not yet a mature technology (Mishra & Prasad, 2011:2; Moharana *et al.*, 2009:7). CO SELMET and CO PROX are simpler catalytic processes, which are cost-effective at large-scale, yet can also be implemented in much smaller systems, and can be executed at atmospheric pressure (Laguna *et al*., 2014:177; Mishra & Prasad, 2011:2). Catalysts such as Rh, Ru, Pd, Ir, Ni, Fe and Co have been reported for CO methanation (Abu Bakar *et al*., 2012:525; Kuznecova & Gusca, 2017:258), while Pt-group metals, Cu and Au catalysts are reportedly active for CO PROX (Laguna *et al*., 2014:177).

A lot of research has been conducted in the area of CO abatement from H_2 gas streams by SELMET and PROX. Due to the exothermic nature and the typical sub-second contact times of these catalytic processes, adequate management of heat and mass transfer is crucial (Laguna *et al.*, 2013:182). Microchannel reactor technology is often referred to as *process intensifying* (Men *et al*., 2007:82). Microchannel reactors not only increase mass transfer due to intimate contact between the gas and the catalyst surface; they also increase heat transfer through limited thermal resistances between the bulk gas phase and the reactor wall material (Atkinson & McDaniel, 2010:97; Jensen, 2001:295). Lerou *et al.* (2010:381–383) added that microchannel

reactor technology enable more environment-friendly processes by increasing the efficient use of raw materials and energy. This technology finds an interesting application with CO SELMET and CO PROX processes, as a result of it sufficing in the heat and mass transfer requirements of these reactions, as well as being well-suited and modular for small and medium-scale applications in the fuel cells sector.

1.2. Problem statement

CO SELMET and CO PROX are not 100% selective towards CO conversion. In the CO methanation case, CO_2 could also be hydrogenated, whereas CO PROX doesn't occur without some H_2 being oxidised in a secondary reaction too. In both processes, the occurrence of a third side reaction, the reverse water gas shift (RWGS) reaction, will lower total CO conversion. To limit side reactions, respective catalysts with high selectivity towards the favoured reaction is mandatory. Reaction temperature is also a parameter that strongly affects reaction selectivity. In this work, there exists a need to fundamentally investigate the effects of reaction temperature, gas hourly space velocity and O_2/CO ratio (in the oxidation case), on the performance metrics of CO conversion, product concentration and selectivity. This will be achieved using a microchannel reactor, which supports narrow temperature control (isothermal), to preferentially convert CO within a model H_2-rich gas stream, typical of the product gas from an industrial water gas shift (WGS) reactor. The H_2 product gas, which contains other impurities such as CO_2, CH_4, and N_2, would still facilitate fuel cell applications, provided that enough H_2 fuel is fed to the fuel cell. Bearing in mind the stringent levels of CO which can cause fuel cell degradation, this work largely aims to demonstrate a very selective CO conversion process using both experimental and computational methods. Finally, global kinetic rate expressions are not readily applied to microchannel reactors due to their vastly different process characteristics; in particular their fast mass transport rates. As part of this work, there exists a need to perform kinetic parameter estimation to validate the computational reactor model to the experimentally-evaluated reactor.

1.3. Motivation

H_2 fuel cells are key to a transition towards an energy system with a low CO_2 footprint (Edwards *et al.*, 2007:1044). Their advantages include a high efficiency, low temperature operation, high scalability and decrease in pollution (Midilli *et al.*, 2005:263–266; Edwards *et al.*, 2008:4358). Fuel cells have proved to be efficient both in stationary and transport applications. Up to 2018, the installed capacity for large stationary fuel cells (>200 kW)

accounted for more than 800 MW worldwide (Weidner *et al.*, 2019:2). By 2030, predictions show that that the technology improvements of fuel cell technology will result in its market competitiveness in capital and operating cost to internal combution engines (Manorahan *et al.*, 2019:2). The supply of large quantities of H_2 is vital. Fossil fuels remain the most economical resource to produce H_2 at an industrial scale in the near and mid-terms (Chunshan, 2010:6). H_2 produced from fossils has a relatively high CO concentration after the WGS process, varying between 0.5 and 2 vol.% (Arzamendi *et al.*, 2011:588), which needs to be decreased to less than 10 or 100 ppm in order to maintain the catalytic durability of Pt or Pt-Ru fuel cell anodes, respectively (Gao *et al.*, 2016:5484). Ultimately, it is envisioned that H_2 will be produced sustainably using renewable energy and water electrolysis technology. In this project however, a typical fossil fuel-derived and H_2-containing syngas will be used to address the uncertainties of CO removal from H_2-rich gas streams to supply small-scale and off-grid fuel cells, using microchannel reactor technology.

SELMET and PROX are considered simple and cost-effective ways to reduce CO levels from H_2-rich gas streams. A lot of research has been done to prove that CO methanation is possible on supported Ni- and Ru-based catalysts and that Ru-based and Au-based catalysts perform well for CO PROX. However, there exists a lack of studies which compare the performance of catalysts such as Ru-Cs/Al_2O_3, Ni-Pt/Al_2O_3 and Au/Al_2O_3 in microchannel reactors of identical geometries, for these processes. This work will study these catalysts for the CO SELMET and PROX reactions, firstly with experiments, but also using a numerical modelling technique.

The small geometric features of microchannel reactors make it difficult to study the transport phenomena inside the channels. Because the catalysts are typically not 100% selective, and different reaction mechanisms take place depending on the CO concentration within the microchannels (i.e. CO oxidation, H_2 oxidation and WGS equilibrium), it is essential to understand and validate the reaction and transport phenomena with numerical methods, in addition to the experimental data obtained. Computational Fluid Dynamic (CFD) modelling has proven to be appropriate for describing such dynamic systems. However, reports on CFD modelling for CO SELMET and CO PROX in microchannel reactors are scarce in the literature. Ultimately, the CFD model of the microchannel reactor will assist in describing the different reaction mechanisms on the micro-scale, which leads to the experimental CO conversion and selectivity obtained at different reactor operating conditions.

1.4. Aim and specific objectives

The aim of this work is to demonstrate the effective conversion of CO contained in a H_2-rich gas, simulating a reformate gas stream from a WGS reactor, with SELMET and PROX techniques. A microchannel reactor coated with a suitable catalyst will be used. Ultimately, the resulting H_2-rich product gas is intended for applications of PEMFC technology, sensitive to CO content in the H_2 fuel.

The specific objectives of this work include:

1. to review the relevant literature on the use of different techniques for CO removal from H_2-rich streams. To devote special attention to the methods involving chemical reaction.
2. to do reactor catalyst screening on the performance of three catalysts (Au-, Ni- and Ru-based) supported within a microchannel reactor, in order to select the most suitable for further investigation.
3. to study the effects of operational parameters including reaction temperature, gas flow rate and small variations in the feed gas composition on the performance of the reactor with the identified best catalyst.
4. to accurately describe the various reaction mechanisms occurring in the dynamic microchannel space with CFD modelling, and validate the model with CO conversion and selectivity data from the experimental microchannel reactor.

1.5. Research Questions

Throughout this work, the following research questions will be answered:

1. What is the current state of development and modelling of processes aiming at CO abatement from H_2-rich gas streams?
2. Which among the selected catalyst (Au-, Ni- and Ru-based) is the most suitable for CO removal from a gas stream, simulating the product from a WGS reactor?
3. For which process and under which operating conditions does the selected catalyst perform best for CO clean-up in H_2-rich gas streams?
4. What set of reactions could be used to model the process in the chosen operational conditions?

5. Can CFD modelling, using the chosen kinetics, be used to describe the process theoretically and give a better understanding of the transport phenomena inside the microchannel reactor?

1.6. Scope of the work

The current chapter consists of an introduction and relevance of the present work to the field of H_2 fuel cells and H_2 gas processing—in particular CO removal techniques—using catalytic reactor technologies with process-intensifying characteristics. The aim and specific objectives of the project are summarised in this chapter.

Chapter 2 gives an overview of the importance of H_2 as an energy carrier, its current production methods, the necessity for CO abatement from H_2-rich gas streams, as well as the different techniques and reactor technologies used for selective CO catalytic conversion. An overview of literature based on the kinetics and modelling of these catalytic processes concludes the chapter.

Chapter 3 describes the microchannel reactors used during this work, as well as the catalysts coated in the three reactor cases. Then, the experimental equipment, as well as the operational parameters that were varied during the experiments, are conferred—for both CO SELMET and PROX. Lastly, the procedures followed during the reaction equilibrium calculations are summarised.

Chapter 4 reports the experimental performance of the three catalyst coated microchannel reactors (Au, Ni and Ru-based) used during the screening test, and later reports on the investigation of the preferred Ru catalyst-coated reactor for the most efficient CO abatement technique, which was identified as CO oxidation. The experimental results report the effects of the reactor operational parameters introduced in Chapter 3 on the conversion of CO, as well as the selectivity towards CO removal.

In Chapter 5, a CFD modelling investigation of the microchannel reactor is presented for the CO oxidation process, and validated on the experimental data presented in Chapter 4. Kinetic parameter estimation are reported in this Chapter to accurately describe the experimental CO conversions, as a function of reaction temperature and space velocity. Finally, the mass transport phenomena within the dynamic region of the microchannel are presented in this Chapter.

Chapter 6 summarises the conclusions from this work, and proposes recommendations and areas of future research on the topic of CO abatement from H_2-rich gas streams to be explored.

CHAPTER 2. LITERATURE REVIEW

Before the year 2050, energy production and consumption are predicted to rise significantly because of the increase in the global population, technological development and improved living standards (Midilli *et al*., 2005:258). Predictions reported by Capellán-Perez *et al.* (2014:5–7) also showed that the extraction of fossil fuels such as oil, natural gas and coal, as well as uranium, is expected to peak before the year 2050. Besides, the use of fossil fuels has had several negative impacts on the environment. The emission of air pollutants such as CO_x, NO_x, SO_x, O_3, etc., and particulates constitute critical environmental issues that require more sustainable solutions (Chauhan & Singh, 2015:63; IRENA, 2017:17; Midilli *et al.*, 2005:260).

The use of renewable energy sources is growing rapidly. According to a 2017 IRENA report, more than 170 countries have clear renewable energy targets, and about 18% of the total final energy consumption came from renewable sources in 2016 (IRENA, 2017:9). Several of these energy sources, such as wind and solar energy, are intermittent in nature, which decreases its capacity factor. Other sources such as biodiesel and biogas have limited efficiencies when burned in combustion engines or turbines (Edwards *et al.*, 2008:4358). H_2 gas is considered as one of the most promising renewable energy carriers. H_2 can be produced, stored, and transported, and supports various end-use applications (IEA, 2019:3). This concept is called power-to-gas technology, to store renewable energy when the power supply exceeds the demand (Lambert, 2018:3–5). It can be converted into methane (CH_4), or other fuels and specialty chemicals, or simply used to regenerate electricity when the power supply from the renewable sources are low; i.e. a grid balancing technique (IEA, 2019:3). To generate power, H_2 finds application through gas turbines, internal combustion engines and fuel cells. Simply put, the power generation step using H_2 emits near-zero emissions (ppms of NO_x during turbine and combustion engine use), while the only other by-product is H_2O. With the assistance of carbon capture technology during the upstream processing of H_2, the future of H_2 as a low carbon fuel looks bright.

2.1. Hydrogen as energy carrier

Despite being the most abundant element in the universe, H_2 is relatively rare in its pure form in the Earth's atmosphere, with a concentration of only 0.5 ppm (Bennaceur *et al.*, 2005:30). Producing pure H_2 therefore requires a primary source of energy such as fossil or biofuels, solar, wind, and nuclear energy, etc. During periods of peak supply, excess renewable energy

could be used to produce H_2 via H_2O electrolysis (IEA, 2019:3). H_2 can be stored and transported as an energy carrier, and subsequently used in fuel cells to regenerate electricity when the supply of renewables does not meet the demand (BACAS, 2006:11). Fuel cells can achieve efficiencies of up to 60% (Chauhan & Singh, 2015:65), depending on operating conditions. On the other hand, combustion engines have average efficiencies around 25% (Edwards *et al.*, 2008:4538).

H_2 fuel cell technology presents interesting advantages when compared to other energy storage technologies (Fig. 2.1). For instance, a comparison between batteries and fuel cells shows that batteries are meaningful for stationary applications (very heavy, leading to a low power density: ~300 W/kg) where high efficiency (70–85%) and discharge times in the order of hours or days are sufficient. Energy storage using H_2 has a lower round-trip efficiency (30–45%), but very high storage capacity (in the order of GWh) and extended storage periods of several days or weeks (in liquid form or gas pipelines).

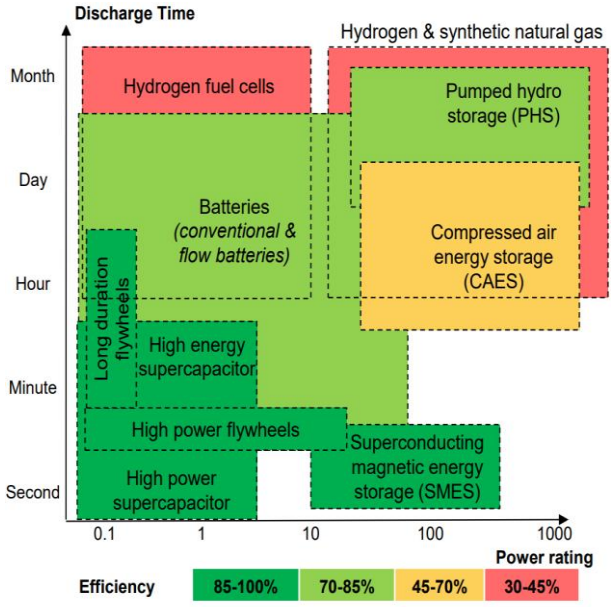

Fig. 2.1. A comparison of energy storage technologies based on discharge time, power rating and efficiency (*SBC Energy Institute, 2013:25)*

Furthermore, using H_2 as fuel will reduce carbon dioxide (CO_2) emissions and other environmental impacts associated with the use of fossil fuels for energy supply (NO_x, SO_x, particulate emissions and fossil fuel depletion). H_2 is also expected to contribute to distributed and small-scale power generation in current off-grid areas, while its production is facilitated by using various energy sources at different geographic locations around the world (Chauhan & Singh, 2015:63). In the African context, the production of H_2 using abundant renewables

sources such as solar and wind energy affords the opportunity to fossil scarce regions such as the Sahara and South-Western Africa to generate GDP from the export of H_2, which was not possible with fossil-based energy in previous years.

2.2. Hydrogen production and usage

According to IRENA (2019:9), the current annual production of H_2 is about 120 million tonnes. A vast majority (95%) of this H_2 is produced from coal and natural gas, and two thirds of the total production is used in the production of petrochemicals and ammonia (IRENA, 2019:9). Other industrial uses of H_2, to name just a few, include its use as a reducing agent during metal ore processing, float glass manufacturing and as a cooling fluid due to its high thermal conductivity (especially is nuclear power applications). Currently, with carbon capture, use and storage technology, H_2 produced from fossil fuels (~1.5–3 USD/kg H_2) comes at a lower cost than renewable H_2 (~2.5–6 USD/kg H_2) (IEA, 2019:53). The cost of renewable H_2, however, could change significantly by 2030 with a decrease in renewable energy costs and a scale-up in H_2 production technology (IEA, 2019:14).

2.2.1. Hydrogen production methods

2.2.1.1. Hydrogen from fossil fuels

Fossil fuels constitute the most economical source of H_2 in the near and mid-term (Song, 2010:6). Below are the most important techniques used during the production of H_2 from fossil fuels.

- Steam reforming of hydrocarbons is a process where syngas (H_2/CO) is produced from the endothermic reaction between steam and a hydrocarbon, typically CH_4, and at high reaction temperature (>800ºC). The H_2 content in the syngas produced by steam reforming can be further increased by the WGS reaction (Dufour *et al.*, 2011:2195). During steam reforming, heat is provided from an external combustion reaction.
- Autothermal reforming uses atmospheric O_2 in the same reactor as steam reforming, to burn some of the fuel and provide heat to the steam reforming reaction. The heat released is a function of the amount of O_2 fed to the reactor (Song, 2010:5). Generally, autothermal reforming yield slightly lower ratios of H_2/CO in the syngas.
- Coal gasification consists of a complex series of reactions in which solid carbon is converted into a gaseous mixture, by contacting coal particles with O_2, steam and CO_2.

The overall process is exothermic, while sulphur treatment and ash handling also becomes important downstream processes (Dufour *et al.*, 2011:2196).

- Partial oxidation is a process in which more O_2 is added compared to autothermal reforming, while steam might also not be present during this process. Partial oxidation still happens in an O_2-lean environment, otherwise total oxidation of the hydrocarbon occurs. The process is exothermic and occurs at high temperature (1300–1500°C). This method produces more CO than steam reforming (Bicakova & Straka, 2010:177).
- Pyrolysis of fossils or biomass involves the heating and degasification of volatile organic material in the absence of O_2 at pressures between 0.1 and 0.5 MPa, and at temperatures between 500 and 900°C. Lower CO_2 emissions are resultant of the fact that no O_2 is fed to the reactor (Bicakova & Straka, 2010:179).
- Plasma cracking is the process in which a plasma generated using electricity is used to provide energy and generate the free radicals to facilitate the cracking reaction (Bicakova & Straka, 2010:181).

The following table summarises the chemical reactions involved in the most popular processes of H_2 production from fossil fuels.

Table 2.1. Processes of hydrogen production from fossil fuels (Song, 2010:5)

Process	**Reaction**
Steam reforming	$C_mH_n + mH_2O = mCO + (m + \frac{n}{2})H_2$
Autothermal reforming	$C_mH_n + \frac{m}{2}H_2O + \frac{m}{4}O_2 = m\,CO + (\frac{m}{2} + \frac{n}{2})\,H_2$
Gasification of carbon	$C + H_2O = CO + H_2$ $C + O_2 = CO_2$ $C + ½\,O_2 = CO$ $C + CO_2 = 2\,CO$
Partial oxidation	$C_mH_n + \frac{m}{2}O_2 = mCO + \frac{n}{2}H_2$
Pyrolysis	$C_mH_n = mC + \frac{n}{2}H_2$
Methane decomposition	$CH_4 = C + 2H_2$
Water gas shift	$CO + H_2O = H_2 + CO_2$

2.2.1.2. Hydrogen from renewable sources

a. Water splitting

H_2 is produced from the splitting of H_2O by using electricity, heat or living microorganisms. Currently, electrolysis accounts for roughly 4% of the total H_2 production worldwide (Kumar & Himabindu, 2019:443). Riis *et al*. (2006:9–14) summarised the main techniques of H_2O splitting, which include: PEM electrolysis, alkaline electrolysis, solid oxide electrolysis, photo-electrolysis, thermochemical H_2O splitting and biophotolysis.

Alkaline, PEM and solid oxide electrolysis are the three principal electrolysis technologies used today (IRENA, 2018:19). Alkaline electrolysis (Fig. 2.2a) is a mature and commercial technology, which makes use of cells containing an alkaline electrolyte (i.e. KOH, NaOH) by which OH^- from the decomposition of H_2O migrate from the cathode (where H_2 is formed) to the anode where they produce H_2O, O_2 and electrons (Kumar & Himabindu, 2019:443; IRENA, 2019:7). During PEM electrolysis (Fig. 2.2b), H_2O splits at the anode into O_2, protons and electrons. The protons migrate to the cathode through a solid membrane, while to electrons flow to the cathode via an external electric circuit (Kumar & Himabindu, 2019:446; IRENA, 2019:7). At the cathode, the protons and electrons combine to form H_2 gas. A solid oxide electrolyser (Fig. 2.2c) uses a solid ceramic membrane as an electrolyte. At the cathode, H_2 and an O^{2-} anion are produced after H_2O combines with electrons. The O^{2-} anions are transported through the membrane towards the anode where they react to produce electrons and O_2 (Kumar & Himabindu, 2019:445; IRENA, 2019a:7).

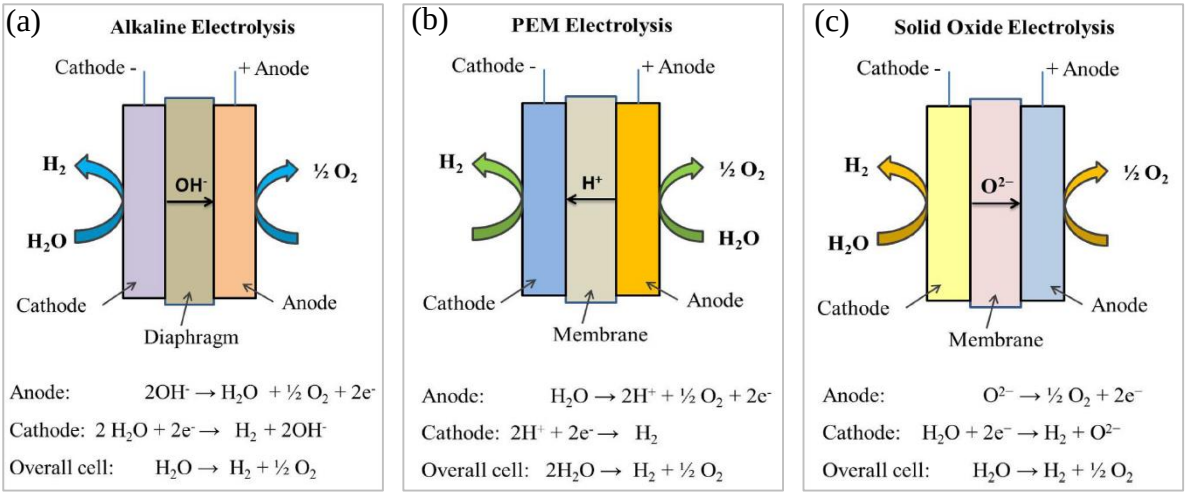

Fig. 2.2. Comparison of the working principles of (a) alkaline, (b) PEM and (c) solid oxide electrolysis (Kumar & Himabindu, 2019:444–446)

Of these electrolysis techniques, solid oxide electrolysis is the least mature and most expensive. High temperature (700–800°C) operation is used to ensure anion conductivity through the ceramic membrane. On the contrary, due to the high temperature operation, the thermoneutral voltage of the H_2O splitting process is slightly lower compared to low temperature electrolysis (80°C), which causes some improvements in the electric efficiency of the solid oxide electrolyser (IRENA, 2019a:23). The ceramic membrane is very fragile, and sensitive to pressure disruptions, mechanical vibrations and rapid thermal fluctuations. A brief comparison of the advantages and disadvantages of alkaline and PEM electrolysis is given in Table 2.2.

Table 2.2. Comparison between alkaline and PEM electrolysis technologies (Kumar & Himabindu, 2019:444–446; IRENA, 2018: 19–21; IRENA, 2019a:19)

Electrolysis technology	**Advantages**	**Disadvantages**
Alkaline	- Commercial applicability since the 1920s. - High durability (~60 000 h) of recent (Gen II) technology. - Relatively low capital expenditure (about EUR 750/kW_e in 2017). - Low operating temperature (30–80°C).	- Not very flexible: difficult to adapt to load changes in electricity generated by variable renewable energies. - Cold start-up time of roughly 1 h. - Limited current density (<400 mA/cm^2). - Low H_2 discharge pressure (<30 bar).
PEM	- Commercial applicability, with recent MW-scale applications. - Compact design due to high current density (1–6 A/cm^2) - Low operating temperature (20–80°C). - High H_2 discharge pressure (Commercial 30 bar operation, with recent R&D of up to 100 bar). - Cold start-up time of 10 min. - High flexibility during operation (0 to 100% load achieved under a min).	- Higher costs: about EUR 1 200/kW in 2017. - State-of-the-art noble metal catalyst required (Pt/Pd; IrO_2/RuO_2). - Durability (~40 000 h) lower than that of alkaline electrolysers.

Photoelectrolysis uses semiconductors immersed into an aqueous electrolyte and which absorbs sunlight. A voltage is generated that is required for the decomposition of H_2O into O_2 and H_2 (Chaubey *et al.*, 2013:453). Thermochemical H_2O splitting uses high temperatures (ca. 2500°C) to decompose H_2O into H_2 and O_2 (Bicakova & Straka, 2010:183). Chaubey *et al.* (2013:456) added that microorganisms can also split H_2O molecules in direct or indirect biophotolysis processes. In the direct process, algae (e.g. Anabaena cylindrical) use sunlight to decompose H_2O directly into O_2 and H_2. In the indirect process, certain green algae and cyanobacteria convert the glucose produced via photosynthesis to H_2 and CO_2 using H_2O and sunlight energy (Chaubey *et al.*, 2013:456).

b. Other methods of renewable hydrogen production

H_2 can also be produced using processes such as biomass gasification and anaerobic digestion. Biomass gasification involves the production of syngas, with a mixture of air and steam fed to the gasifier. The process has a low thermal efficiency (35–50%) due to the relatively high moisture content of the biomass feedstock (Kalamaras & Efstathiou, 2013:5). Biological H_2 production is a technique which uses anaerobic microorganisms to decompose non-toxic organic matter, rich in carbohydrate, into organic acids and H_2 during anaerobic digestion. H_2 is a by-product of the process and its yield can be improved by manipulating the conditions in the acidogenic phase, or with pre-treatment of the microbial-rich slurry (Chaubey *et al.*, 2013:445).

2.2.2. Hydrogen use in fuel cells

Fuel cells are devices which produce electricity, H_2O and heat by inverse electrolysis (Owens & McGuiness, 2016:13). A fuel cell typically consists of an electrolyte in contact with porous electrodes. The anode continuously receives fuel that is oxidised (i.e. H_2-containing compound), while O_2 is reduced to H_2O is supplied at the cathode (Edwards *et al.*, 2008:4358). At the anode, the electrochemical oxidation reaction with the fuel ultimately produces electrons which migrate to the cathode via an external electric circuit to the electrolyte, thus generating a direct current (Edwards *et al*., 2008:4358-4359).

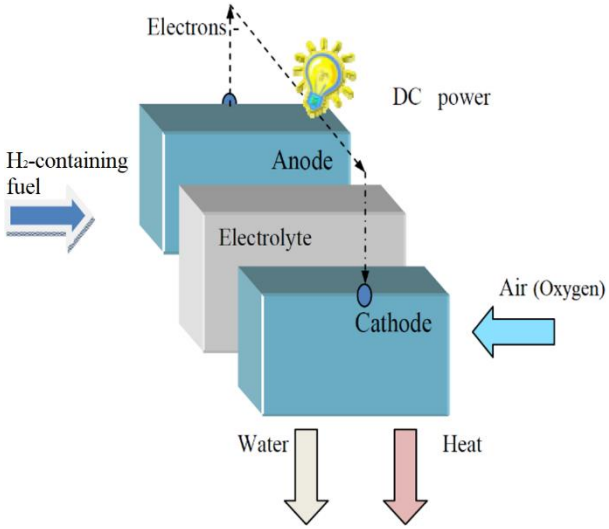

Fig. 2.3. Schematics of a typical fuel cell system (Giorgi & Leccese, 2013:3)

2.2.2.1. Fuel cell types

According to Akinyele *et al.* (2020:9), fuel cells are divided according to the nature of the electrolyte used, into six technological groups. Molten carbonate fuel cells (MCFC) and solid oxide fuel cells (SOFC) use a molten carbonate salt and non-porous solid ceramic as electrolytes, respectively. They operate at high temperatures (600–800°C and 800–1000°C, respectively) and have efficiencies greater than 60%, which can reach 80% when heat is harnessed in a combined heat power system. SOFC and MCFC's high operating temperatures allow them to use relatively cheap catalysts (e.g. Ni-based catalysts) at the electrodes (Akinyele *et al.*, 2020:11–12; Giorgi & Leccese, 2013:14–15). Besides, the need to convert light hydrocarbons to hydrogen is eliminated, as internal reforming takes place inside the fuel cell. High temperature also render the technologies less susceptible to CO poisoning. These advantages of SOFC and MCFC due to high temperature are offset by the long start-up times, fast corrosion and low material durability (Giorgi & Leccese, 2013:14–15).

Operating at medium temperatures (180–200°C), phosphoric acid fuel cells (PAFC) use H_3PO_4 as an electrolyte and have an efficiency of about 40%. They are relatively more tolerant to impurities in H_2-rich gas such as CO, despite the fact that Pt-based catalyst are used at the electrodes (Felseghi *et al.*, 2019:16; Akinyele *et al.*, 2020:12). The use of expensive catalysts, the long start-up periods and the sensitivity to sulphur are their main disadvantages.

Fuel cells operating in the low temperature range (70–120°C) include direct methanol fuel cells (DMFC), alkaline fuel cells (AFC) and proton exchange membrane fuel cells (PEMFC).

DMFC uses an aqueous methanol solution as fuel and operate at temperatures between 70 and 100°C (Giorgi & Leccese, 2013:10). They use Nafion membranes as an electrolyte and Pt-based catalysts as their electrodes. According to Akinyele *et al.* (2020:13), the main drawback of the technology is the efficiency which is the lowest among fuel cells (35–40%). AFC operate around 70°C using an aqueous alkaline (KOH) solution as electrolyte and H_2 as fuel (Giorgi & Leccese, 2013:11). Their advantages include their quick start-up, the use of relatively inexpensive catalysts (Ni, Ag) and their relatively high efficiency (around 60%). The main drawbacks are the corrosive nature of the electrolyte as well as the tendency for CO_2 adsorption which reduces the electrolyte's ionic conductivity (Felseghi *et al.*, 2019:16). Lastly, PEMFC uses a thin and highly proton conductive polymeric membrane as electrolyte. The most common membrane used in PEMFC is the Nafion membrane, but other types include polymer-zeolite nanocomposite PEM, the bisbenzoxazole high temperature ion-conducting membrane and the sulfonated polyphosphazene based membrane (Giorgi & Leccese, 2013:7). Mishra & Parsad (2010:1) mentioned the PEMFC as an attractive clean and efficient technology for both stationary and non-stationary power applications due to the low-temperature operation (80°C). According to Giorgi & Leccese (2013:8), PEMFC's low operation temperatures allow for the use of a variety of low-cost component materials, and the mechanical strength of the supported electrolyte allows for high operating pressure differences between the electrodes. Other advantages include low start-up times, high specific power (>1 000 W/kg fuel cell), relatively high efficiency (40–60%) (Akinyele *et al.*, 2013:12). The major drawbacks of PEMFC technologies are the low recovery of waste heat, the required management of humidified hydrogen to the membrane for appropriate ionic conductivity, and the high intolerance to contaminants (especially CO) present in H_2-rich gas streams (Giorgi & Leccese, 2013:8).

2.2.2.2. Contaminants in hydrogen intended for PEMFC applications

H_2 produced industrially is not free from impurities. According to Cheng *et al.* (2007:741), the most common contaminants include nitrogen (N_2), CO_2, CH_4, CO, NH_3, nitrogen oxides, sulfur compounds, Cl_2 and other organic substances. Most of these have undesirable effects on the performance of fuel cells. N_2, CO_2 and CH_4 dilute the H_2 fuel and decreases fuel cell performance (Wang *et al.*, 2014:19702). Li *et al.* (2003:A1599) suggested that CO adsorbs directly onto the Pt active sites of the fuel cell anode, effectively reducing the active area of the anode; this may happen at CO concentrations as low as 10 ppm (Wang *et al.*, 2014:19702). NH_3 forms NH_4^+, which replaces the protons on the sulfonic terminals of a common Nafion membrane (PEMFC), and decreases the membrane's conductivity towards proton transfer

(Noda *et al.*, 2017:3282). Sulfur compounds such as H_2S dissociate on the Pt electrode, resulting in linearly bonded Pt-S or bridge-bonded $(Pt)_2$-S (Sethuraman & Weidner, 2010:5684).

CO is one of the most undesirable impurities when contained in H_2 gas intended for fuel cell applications. CO can be either linearly- or bridge-bonded to Pt atoms, thus reducing the number of active sites available for H_2 electrochemical oxidation. Cheng *et al.* (2007:742) stated that the poisoning effect of CO is dependent on the fuel cell operating temperature, the duration of the exposure to CO, the nature of the catalyst and the concentration of CO. PEMFC using Pt anodes and operating at low temperature (<100°C) are most vulnerable to CO poisoning, even at concentrations as low as 10 ppm (Cheng *et al.*, 2007:744). More CO tolerance can be achieved using Pt-Ru anodes, which are able to tolerate up to 100 ppm CO in H_2-rich gas streams. This is as a result of the Ru active sites' ability to oxidise CO towards CO_2 (to a certain extent of CO concentration), which is then desorbed (Park *et al.*, 2008:280; Mohaideen *et al.*, 2015:8). The kinetics supported by high temperature fuel cells (e.g. 1000°C for solid oxide fuel cells) and the fact that they do not support Pt catalysts allow them to use CO as a fuel. This technology however will not be discussed further.

2.3. Hydrogen purification and CO abatement technologies

Industry requirements for H_2 purity are quite strict. For instance, for fuel cell vehicles, the International Organization for Standardization (ISO) specifies H_2 gas containing less than 0.2 ppm CO as a quality standard (Noda *et al.*, 2017: 3282). In order to decrease the CO level in H_2 gas from a typical WGS reactor, several methods can be used. They include: H_2 purification using a selective membrane, Pressure Swing Adsorption (PSA), CO selective methanation (SELMET), CO preferential oxidation (PROX), cryogenic distillation and electrochemical H_2 pumping (Mishra & Prasad, 2011:2–5; Pasierb & Rekas, 2011:1–2).

2.3.1. Purification of hydrogen using selective membranes

Membrane purification is a pressure driven process which takes advantage of the fact that only H_2 atoms are able to permeate through a H_2 separation membrane which separates the mixture into a H_2-rich stream (permeate) and a stream of the impurities (retentate) (Edlund, 2010:358).

Edlund (2010:359) listed four types of commonly used membranes: polymeric membranes, porous membranes, dense metal membranes and ion conductive membranes. Polymeric membranes consist of polyimide cellulose acetate; they operate at relatively low temperature

(<110°C) and moderate to high permeability. Nanoporous membranes, consisting of materials such as alumina, silica, zeolites and carbon, operate at higher temperature ($\leq$ 1000°C) and have low to moderate permeability for H_2. The last two membrane types have great H_2 selectivities and moderate permeabilities. Dense metal membranes, made of palladium alloys, operate at temperatures between 150 and 700°C, whereas ion conductive membranes, known for their use in fuel cells, operate in a wider range from below 180°C to 1000°C, depending on the material of construction (Edlund, 2010:359).

Membrane separation can be used in small to large-scale H_2 production (Grashoff *et al.*, 1983:157). High H_2 purities (>99.99%) can be achieved during a single stage of dense metal membrane separation, and with multiple stages using polymeric membranes (Edlund, 2010:363). However, the mechanical strength of the membranes is often low and they are sensitive to swelling and compacting. Metallic membranes are also subject to H_2 embrittlement at low temperatures (Mishra & Prasad, 2011:2).

2.3.2. Pressure Swing Adsorption (PSA)

About 85% of the H_2 produced worldwide is purified using PSA technology. Sircar & Golden (2010:414) explain that the process consists of selectively adsorbing, at high pressure, the impurities from a H_2-rich gas on mircoporous or mesoporous solid adsorbents such as zeolites, activated carbon, silica and alumina gels. The adsorption rate depends on the molecular characteristics of the gas and its affinity with the adsorbent. Once the adsorption step is complete, desorption of the gas from the adsorbent is done by reducing the pressure of the gas inside the adsorption column (Sircar & Golden, 2010:414–415). Continuous operation is possible with a multicolumn system operating in precise cycles, which involve steps of adsorption and desorption, which are designed to optimise process efficiency, gas production rate and H_2 purity (Sircar & Golden, 2010:415).

Purity levels of 98 to 99.999% and a recovery ranging of 70–90% can be achieved using PSA. The CO concentration can often be reduced from 4% to 1.4 ppm (Mishra & Prasad, 2011:4). The design of a PSA H_2 purification unit is fairly complex; it involves the use of high compression ratios and multicolumn adsorption systems (Sircar & Golden, 2010:415), making PSA suited for large-scale processes and stationary applications (Grashoff *et al.*, 1983:158).

2.3.3. Cryogenic processes

Dehghani *et al.* (2012:2199) noted that H_2 can be separated from light hydrocarbons by partial condensation of these hydrocarbons at temperatures ranging between -153 and 0°C. The process is only feasible due to the even lower condensation point of H_2 (-252.88 °C), ensuring that H_2 stays in the gas phase during process operation. Cryogenic processes can include a distillation column, which result in higher product recoveries and H_2 purities (up to 99.5%), but increases cost and energy consumption (Dehghani *et al.*, 2012:2199).

2.3.4. Electrochemical hydrogen pump

Electochemical H_2 purification is one of the most efficient ways to separate H_2 from a gas mixture at low current densities. In the region of high current densities and constant voltage, the mass-transfer overpotential results in a decrease in current densities (Nordio *et al.*, 2019:434).

A H_2 pump uses a direct electric current to split H_2 on the anode, and drive the protons through the proton conducting membrane to the cathode, where the protons are reduced to H_2 (Pasierb & Rekas, 2011:1–2). Importantly, this proton conducting membrane is not permeable for H_2 gas itself, making it possible to pressurise H_2 at the cathode side, in addition to purifying it. The types of membranes can include: polymer, metallic, ceramic/glass, ion transport and mixed ionic-electronic transport membranes (Pasierb & Rekas, 2011:1). Equations (2.1 and 2.2) summarize the mechanism of electrochemical H_2 purification.

$$H_2\,(\text{gas mixture}) \rightarrow 2H^+\,(\text{solid electrolyte}) + 2e^- \qquad \textit{(anode reaction)} \qquad (2.1)$$

$$2H^+\,(\text{solid electrolyte}) + 2e^- \rightarrow H_2\,(\text{purified}) \qquad \textit{(cathode reaction)} \qquad (2.2)$$

Water management during electrochemical H_2 purification is crucial in order to avoid problems such as water clogging or dehydration of the membrane (Nordio *et al.*, 2019:438).

2.3.5. CO selective methanation

This process consists of selectively converting the CO contaminating the H_2-rich gas stream into CH_4. CH_4 does not pose any harmful effects on fuel cell anode catalysts or proton conducting membranes of PEMFC (Dagle *et al.*, 2007:213). The CO methanation process is considered simple and not costly because it does not involve other process gas streams or an external supply of air (Panagiotopoulou *et al.*, 2008:45). However, the H_2 consumption in this process may be very high, since three moles of H_2 are consumed for every mole of CO

converted. The presence of CO_2 in the H_2-rich gas significantly increases H_2 consumption if the CO methanation reaction does not occur selectively. Temperature control (Dagle *et al.*, 2007:214) and the use of a highly selective catalyst (Gao *et al.*, 2016:5485) are essential in order to maintain a high selectivity towards CO methanation and limiting H_2 consumption. Obviously, CO methanation is not feasible when CO abatement of significant amounts of CO (>3%, but to the discretion of the engineer) is required, due to the extent of H_2 consumption it would induce.

2.3.6. CO preferential oxidation

CO PROX is a process which uses O_2 from an additional feed stream to the reactor, to selectively convert CO into CO_2. The high heat of combustion of this process ensures that, at low temperature, active catalysts towards CO oxidation is a promising prospect. This relates to the equilibrium effect of combustion at low temperature (<200°C). On the other hand, the relatively high amounts of H_2 in a WGS reformate stream renders H_2 oxidation almost unavoidable (Castaldi, 2010:332). Generally, the CO oxidation process is cheap and effective. It can be performed at atmospheric pressure and at temperatures close to the operating temperature of PEMFC. It is a method suitable for small-scale fuel processors and auxiliary power units (Laguna *et al.*, 2014:177).

2.4. Thermodynamics and literature on CO removal from hydrogen-rich gas streams by chemical reaction

The most mature physical methods of H_2 purification such as PSA and membrane separation technologies present several drawbacks in their applicability to small-scale or on-site processes. Elevated pressures, high energy requirements, intricacy of the process and high cost have already been mentioned as shortcomings for these processes. CO removal from H_2–rich gas streams by means of catalytic reactions has the potential to offset these disadvantages. CO SELMET and PROX can be applied at atmospheric pressures, with relatively low energy requirements. Besides, there is lower need for cooling since the operating temperature of fuel cells (~ 80°C) is close to the operation temperature of catalytic CO clean-up techniques. Furthermore, as it will be demonstrated in this work, CO SELMET and PROX processes are suitable for small scale process-intensifying applications such as microchannel reactor technologies.

2.4.1. CO removal by selective methanation

2.4.1.1. Reactions involved in the CO selective methanation process

Three main reactions occur during the process of SELMET, namely: the methanation of carbon monoxide, the methanation of CO_2 and the reversible WGS reaction (Garbis *et al*., 2019:2). All three reactions are exothermic in nature, whereas the reverse reaction (RWGS) of the WGS is endothermic; possibly occurring in a higher temperature range. In a CO SELMET system, equilibrium thermodynamics (as a function of temperature, pressure and feed composition) in the reactor are considered very important, and will determine the extent at which each of the reactions take place.

$$CO + 3H_2 = CH_4 + H_2O \qquad \Delta H = -206 \text{ kJ/mol} \qquad (2.3)$$

$$CO_2 + 4H_2 = CH_4 + 2H_2O \qquad \Delta H = -165 \text{ kJ/mol} \qquad (2.4)$$

$$CO + H_2O = H_2 + CO_2 \qquad \Delta H = -41 \text{ kJ/mol} \qquad (2.5)$$

Gao *et al.* (2011:2359–2367) studied the thermodynamic equilibrium effects of the methanation of carbon oxides. To calculate equilibrium compositions at different reaction temperatures and pressures, the Gibbs free energy minimization method was used in CHEMCAD software. A feed gas containing a $CO/CO_2/H_2$ mixture in a ratio of 1/1/7 was simulated, while the possible products were considered as CO, CO_2, H_2, N_2, H_2O, CH_4 and C_2H_6. The results (Fig. 2.4) showed that at low temperatures, a high H_2/CO_x ratio and high pressures are favourable conditions for CO_x methanation. These results are in accord with the Le Chatelier principle, which suggests that exothermic reactions are favoured at lower reaction temperatures. In addition, higher pressures are advantageous for gaseous reactions in which the total number of moles decrease as the reactions progress. Figure 2.3 illustrates that near complete conversion of CO is possible, especially at temperatures below 300°C. However, at this temperature and at one atmosphere pressure, CO_2 conversion is also in the range of ~90%. Careful consideration of the experimental conditions is therefore necessary in order to avoid high H_2 consumption by CO_2 methanation, while still being able to convert CO via the methanation and WGS pathways.

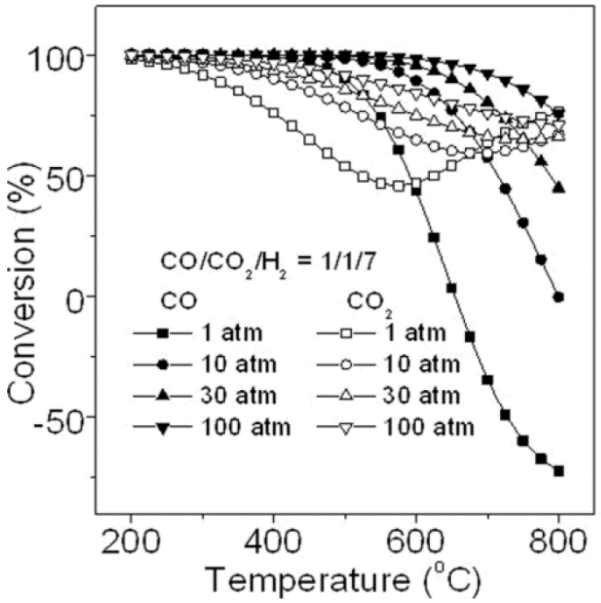

Fig. 2.4. CO and CO_2 equilibrium conversion in the 200–800°C temperature and 1–100 atm pressure range. The results correspond to a $CO/CO_2/H_2$ inlet feed ratio of 1/1/7 (Gao et al., 2011:2366)

2.4.1.2. Parameters affecting CO selective methanation

a. Reaction temperature

Reaction temperature is a key factor in the selectivity towards CO methanation. A kinetic investigation by Garbis *et al.* (2019:5–15) showed that, for a feed gas consisting of 1.13 vol.%CO, 13 vol.% CO_2, 10 vol.% H_2O, 55 vol.% H_2 and N_2, the CO methanation light-off temperature was lower than that of the CO_2 methanation reaction. In their experiments, at a temperature of 220°C, the CO and CO_2 conversions were approximately 90% and 1.5%, respectively. Liu *et al.* (2014a:134) studied Ni-based catalysts, and showed that CO methanation occurred selectively on the catalyst at temperatures between 180 and 240°C, whereas CO_2 methanation noticeably occurred above 220°C. Liu *et al*. (2008:271–273), investigated the performance of a Ni/ZrO_2 catalyst, and reported that the temperature range for an increase in CO conversion was 220–300°C. The CO levels started increasing again at higher temperatures due to the RWGS reaction, which produces CO and H_2O, while consuming CO_2 and H_2. On a 1.6 wt.% Ni/ZrO_2 catalyst, maximum CO conversion with minimal H_2 consumption was achieved between 260 and 280°C. Mohaideen *et al*. (2015:12–13) studied a Ru/Ni-Al catalyst and found that the catalyst performed best for CO SELMET at temperatures ranging between 150 and 250°C. Above 250°C, similar observations of increasing CO content due to the effects of the RWGS reaction was made (Mohaideen *et al*., 2015:11). Panagiotopoulou *et al*. (2009:470–478) studied the SELMET of CO on a Ru catalyst supported

on Al_2O_3, TiO_2, CeO_2 and SiO_2 in a quartz tube reactor. In their experiments, temperature was found to play an important role. On a 5 wt.% Ru/Al_2O_3 catalyst, the selectivity towards CO methanation increased from 75 to 100%, comparing temperatures of 200 and 260°C, respectively. This caused a sharp decline in the selectivity towards by-products of hydrogenation (C_2H_6, C_2H_4 C_3H_8 and C_3H_6). These by-products amounted to 2–9 vol.% of the product gas at 200°C.

b. Pressure

Le Chatelier's principle suggests that methanation reactions (Eqs. 2.3 and 2.4) are affected by reactor pressure. In large-scale reactors, high pressures were reported to favour CO and CO_2 conversions (10–15% increase) and improve selectivity towards the production of CH_4. Reaction pressure can be as high as 10 to 30 atm (Lazdans *et al.*, 2016:542). Most of the studies on CO SELMET in the literature did not consider pressure as critical process parameter.

c. Space velocity

The space velocity (specific gas flow rate) is an important factor influencing the methanation reaction. Lower space velocities increase the residence time of the gas in the reactor, which in turn improves the yield of the reaction (Lazdans *et al*., 2016:542). In a study on a 0.5 wt.% Ru/Al_2O_3 catalyst, an increase in space velocity from 12 000 h^{-1} to 48 800 h^{-1} resulted in a shift of maximum CO conversions towards a higher temperatures (from 280 to 320°C). (Panagiotopoulou *et al.*, 2009:476).

d. Feed composition

Castaldi (2010:331) stated that typical reformate gas contained about 1 vol.% CO, 10 vol.% CO_2, 25 vol.% H_2O, 30 vol.% or more H_2 (depending on the origin of the reformate gas) and N_2 as balance. The undesirable effects of some of the components of the feed gas is obvious. The reaction of CO_2 methanation (Eq. 2.4) consumes 4 moles of H_2 for every mole of CO_2. Also, in the presence of significant amounts of CO_2 and H_2 compared to that of CO, the reaction system will favour RWGS (Eq. 2.5) and produce undesired CO. The effects of steam in the feed gas has been investigated in many reported studies. Abdel-Mageed *et al.* (2018:5411) reported that the presence of 5 vol.% H_2O in the feed gas did not result in noticeable changes in the activity of Ru/TiO_2. Panagiotopoulou *et al.* (2009:477) studied the effects of increasing H_2O (from 0 to 30 vol.%) on a 5 wt.% Ru/TiO_2 catalyst, and concluded that the H_2O had insignificant effects on CO methanation, while it shifted minimum temperatures for CO_2 conversion from ~ 250 to 300°C.

2.4.1.3. Catalysts

The choice of catalyst is essential in selective CO methanation. According to Mohaideen *et al.* (2015:8), good catalysts should satisfy the following requirements:

- High activity. The catalyst must be able to reduce CO content from 0.5–1 vol.% to a few ppm CO at mild operating conditions.
- High selectivity. The catalyst must hinder the CO_2 methanation reaction, which consumes undesirable amounts of H_2.
- To allow an acceptable operating temperature window which provides stable operation in the fuel processor.

A lot of research has been done on the methanation of carbon oxides (CO_x) as an efficient method for storing excess power from renewable energy in a gas (power-to-gas concept). Several catalysts, mostly from group 8 and 10, have proved to be efficient for the conversion of CO_x to CH_4. According to Ronsch *et al.* (2016:284), the most active catalysts include Ru, Fe, Ni, Co, Rh; and the most selective catalysts include Pd, Pt, Ir and Ni. On the other hand, for the purpose of this work, there has to be a distinction between the methanation of CO and that of CO_2. CO methanation has to occur selectively, as mentioned as one of the prerequisites to retain as much H_2 as possibly in the ultimate fuel.

Ru and Ni are considered amongst the most promising catalysts for SELMET for CO removal from H_2-rich gas streams (Mohaideen *et al.*, 2015:8–9). Panagiotopoulou *et al.* (2009:471) and Abdel-Mageed *et al.* (2018:5399) suggested that Ru was one of the most active catalysts for CO methanation; its activity being a few orders of magnitude higher than those of Rh and Pd (Panagiotopoulou *et al.*, 2009:471). Ni is mainly considered for its fair activity in a wider temperature window, as well as its high availability and low cost (Cheng *et al.*, 2017:419). Men *et al.* (2007:84) compared several Ni-based catalysts with Ru-based catalysts and found that Ni catalysts were able to achieve much higher conversions at lower temperatures compared to Ru catalysts.

The size characteristics of the catalyst have an effect on its performance during CO SELMET. Panagiotopoulou *et al*. (2009:471–473) reported that the performance of Ru- catalysts also depend on the active metal particle size. The authors stated that Ru performed 17 times better when particle size increased from 1.3 to 17 nm. Abdel-Mageed *et al*. (2018:5412) used a Ru-based catalyst and concluded that a decrease in catalytic activity and selectivity towards CO

methanation was attributed to particle size growth of the active metal. The argument was that larger Ru particles decreased the surface area of the support (TiO_2), thus decreasing metal-support interaction. Gao *et al.* (2013:2014) studied the effect of Ni particle size on the methanation of CO for syngas production. Ni particles of size 10–20 nm performed better than smaller (5–10 nm) or larger particles (20–35 nm). The medium-size particles exhibited in higher catalytic activity and were less prone to carbon deposition.

From the literature, it is evident that catalyst activity depends on active metal loading. Galletti *et al*. (2010:593–595) have studied the effect of the metal loading using 3 to 5 wt.% Ru/Al_2O_3 for CO SELMET. Complete CO conversion was achieved on the 5 wt.% Ru/Al_2O_3, in the temperature range of 280–340°C. The 4 wt.% Ru/Al_2O_3 catalyst achieved higher selectivity towards CO methanation at a larger temperature range (300–340°C) than the 3 and 5 wt.% Ru/Al_2O_3 catalysts. Panagiotopoulou *et al*. (2009:472–473) reported that an increase in Ru metal loading from 0.5 to 5 wt.% on Al_2O_3 or TiO_2 support materials shifted the conversion of CO towards lower temperatures. A CO conversion of 95% was achieved at 260°C on 5 wt.% Ru/Al_2O_3. On a Ni-based catalyst, Gao *et al*. (2016:5489) found that an increase in catalyst loading resulted in an increase in CO conversion at the expense of the selectivity.

Abdel-Mageed *et al*., (2018:5399) mentioned that the nature of the metal support plays an important role in the activity of the catalyst. In a study on CO and CO_2 methanation, Le *et al.* (2017:89–96) compared the performance of Ni catalyst over SiO_2, TiO_2, CeO_2, and ZrO_2, and concluded that CeO_2 showed the best performance because of the high dispersion of Ni and its strong interaction with the support. Panagiotopoulou *et al.* (2009:475) investigated activities of Ru-based catalysts on different supports including Al_2O_3, TiO_2, CeO_2 and SiO_2. This study showed that the performance of Ru supported by TiO_2 and Al_2O_3 was superior to the other catalysts for CO methanation, while Ru/SiO_2 was only active for the RWGS reaction.

The preparation method is an important factor that influences the activity of the catalyst. Galletti *et al*. (2010:593) reported very good performances of catalysts containing 3–5 wt.% Ru supported by Al_2O_3. CO methanation conversions were near complete for temperatures between 280 and 360°C. Tada *et al.* (2011:151–152) compared the performance of 0.5 wt.% Ru supported on Al_2O_3 and TiO_2 in a fixed bed quartz reactor, investigating the role of the reduction pre-treatment method on the activity of the catalyst. On the Ru/Al_2O_3 catalyst, the increase in reduction temperature from 300°C to 600°C resulted in a decrease in CO methanation activity, as well as a shift in CO_2 methanation towards higher temperatures. Gao

et al. (2016:5489) found that increasing the Ni reduction temperature in the preparation steps resulted in an increase in metallic Ni, which increased both the activities of CO and CO_2 methanation.

A summary of the performance of Ni and Ru-based catalysts for CO methanation is reported in Table 2.3.

Table 2.3. A summary of literature on the SELMET of CO on Ru- and Ni-based catalysts

Reference	Catalyst used	Reactor technology	Feed composition (vol.%)	Temperature	Space velocity	Performance
Dagle *et al*. (2007:214–218)	1–7 wt.% Ru/Al_2O_3	Fixed bed quartz	0.9% CO, 24.5% CO_2, 68.9% H_2 and H_2O	200–290°C	13 500 h^{-1}	On 3% Ru/Al_2O_3, CO product concentration: <100 ppm from 240 to 280°C. H_2 consumption: <10%
Djinovic *et al*. (2011:283–286)	1, 3 & 5 wt.% Ru/Al_2O_3 and 1, 3 & 5 wt.% Ru/CeO_2	Fixed bed quartz	0.56% CO, 42.2% H_2, 21.7% CO_2 and N_2	150–450°C	19.8 $L.g_{cat}^{-1}.h^{-1}$	CO conversion: almost 100% from 210 to 244°C on 5 wt.% Ru/Al_2O_3. For Ru/Al_2O_3 catalysts, ratio $\frac{CH_4 formed}{CO\ converted}$ <1.3 was obtained in a temperature range >210°C.
Galletti *et al*. (2010:591–595)	3–5 wt.% $Ru/\gamma\text{-}Al_2O_3$	Fixed bed quartz	0.5% CO, 40% H_2, 18% CO_2, 15% H_2O and N_2	150–420°C	19.8 $L.g_{cat}^{-1}.h^{-1}$	CO concentrations: <2 ppm from 290 to 340°C. On 4% Ru/Al_2O_3, ratio $\frac{CH_4 formed}{CO\ converted}$ <1.3 from 300 to 340°C.

Table 2.3. A summary of literature on the SELMET of CO on Ru- and Ni-based catalysts (continued)

Reference	Catalyst used	Reactor technology	Feed composition (vol.%)	Temperature	Space velocity	Performance
Galletti *et al*. (2011:617–619)	3 wt.% Ru/γ-Al_2O_3 and 3 wt.% Ru/CeO_2	Fixed bed (FBR) and Microchannel (MCR)	0.5% CO, 40% H_2, 18% CO_2 and 15% H_2O and N_2	150–400°C	19 $L.g_{cat}^{-1}.h^{-1}$	CO conversion on Ru/Al_2O_3: 98% in the MCR at 310°C; almost complete in the FBR from 240 to 280°C CH_4 product concentration: <0.2% in the MCR.
Gao *et al*. (2013:921–924)	10 wt.% Ni/Al_2O_3	U-shaped fixed bed quartz	60% H_2, 20% CO and N_2	300–600°C	120 $L.g_{cat}^{-1}.h^{-1}$	CO conversion: 97.8% at 400°C; CH_4 selectivity: 92.9%.
Gorke *et al*. (2005:136)	44.3 wt.%Ru/Al_2O_3 and 80.2 wt.% Ru/SiO_2	Microchannel	1% CO, 1% O_2, 25% H_2 and N_2	100–350°C	447 $L.g_{cat}^{-1}.h^{-1}$	CO conversion: 95% on Ru/SiO_2 at 285°C and on Ru/Al_2O_3 at 350°C. CH_4 selectivity: > 90% on Ru/SiO_2 at 300°C (some CO_2 formed because of CO oxidation).

Table 2.3. A summary of literature on the SELMET of CO on Ru- and Ni-based catalysts (continued)

Reference	Catalyst used	Reactor technology	Feed composition (vol.%)	Temperature	Space velocity	Performance
Le *et al*. (2017:90-95)	10, 25–75 wt.% Ni supported on CeO_2, and 10%Ni supported on Al_2O_3, SiO_2, TiO_2, ZrO_2	Fixed bed quartz	1% CO or CO_2, 50% H_2 and He	150–400°C	60 $L.g_{cat}^{-1}h^{-1}$	Complete CO and CO_2 conversions on 58 wt.% Ni/CeO_2 from 210°C.
Lee *et al*. (2014:422–424)	Pt/A-zeolite; Ru/TiO_2	Hybrid microchannel	1% CO, 0.5–1% O_2, 20% CO_2, 15% H_2O, 60% H_2, and N_2	60–260°C	30 000 h^{-1}	CO product concentration: <10 ppm from 92 to 235°C. H_2 consumption: < 7%
Liu *et al*. (2014b:39–44)	20 wt.% Ni/Al_2O_3 and 5 wt.% V_2O_3/20 wt.% Ni/Al_2O_3	Fixed bed quartz	60% H_2, 20% CO, and N_2 or 60% H_2, 15% CO_2 and N_2.	260–500°C	120 $L.g_{cat}^{-1}.h^{-1}$ & 90 $L.g_{cat}^{-1}.h^{-1}$ for CO and CO_2 methanation respectively	CO conversions: almost 100% from 300 to 400°C on both catalysts. CO_2 conversion: 82% on V_2O_3-Ni/Al_2O_3 at 420°C.
Liu *et al*. (2008:269–271)	0.6–15 wt.% Ni/ZrO_2	Packed bed	74.8% H_2, 1.14% CO, 21.43% CO_2, 1.80% H_2 and N_2	200–340°C	10 000 h^{-1}	On 1.16 wt.% Ni/ZrO_2, CO product concentration: 20 ppm, H_2 conversion below 7% at 260–280°C.

Table 2.3. A summary of literature on the SELMET of CO on Ru- and Ni-based catalysts (continued)

Reference	Catalyst used	Reactor technology	Feed composition (vol.%)	Temperature	Space velocity	Performance
Liu *et al*. (2009:498–501)	30 wt.% Ni/Ru/B/ZrO_2 (Ru/Ni ratio: 0.15)	Fixed bed	78.15% H_2, 1.08% CO, 23.68% CO_2, 0.52% H_2O and N_2	170–250°C	12 000 h^{-1}	CO conversion: 99.93% from 210 to 250°C CO_2 conversion: < 2.7%.
Liu *et al*. (2014a:132–134)	1.9–18.6 wt.% Ni/ZrO_2	Fixed bed quartz	1% CO, 3% H_2O, 23% CO_2, 70% H_2 and N_2	160–320°C	23 $L.g_{cat}^{-1}.h^{-1}$	CO conversion: > 98% from 240 to 280°C. CO_2 conversion: <11%.
Men *et al*. (2007:82–86)	43 wt.% Ni/CaO/Al_2O_3, 5–10 wt.% Ru/Al_2O_3 and 5 wt.% Ru/Y/ZrO_2	Microchannel	37.5% H_2, 1.6% CO, 12.5% CO_2, 25% H_2O and N_2	150–350°C	180 $L.g_{cat}^{-1}.h^{-1}$	CO conversion: 93% at 300°C on Ni/CaO/Al_2O_3. Selectivity: 64% at 300°C.
Mohaideen *et al*. (2015:9–12)	1 wt.% Ru/NiAl mixed oxide, NiAl mixed oxide and 30% Ni/Al_2O_3	Fixed bed quartz	1.15% CO, 15% H_2O, 23% CO_2,72% H_2 and N_2	130–320°C	2 400 h^{-1}	CO product concentration: <100 ppm from 150 to 250°C on Ru/NiAl mixed oxide.

Table 2.3. A summary of literature on the SELMET of CO on Ru- and Ni-based catalysts (continued)

Reference	Catalyst used	Reactor technology	Feed composition (vol.%)	Temperature	Space velocity	Performance
Panagiotopoulou *et al.* (2009:471–476)	1 to 5 wt.% Ru/Al_2O_3 Ru supported on TiO_2, SiO_2, CeO_2	Fixed bed quartz	1% CO, 15% CO_2, 50% H_2 (10 – 30% H_2O) and He	170–470°C	12 200 to 48 800 h^{-1}	CO conversion: >90% on above 260°C, and above 220°C on Ru/Al_2O_3 and Ru/TiO_2 CO_2 conversion: <40% CH_4 selectivity: >95% above 260°C.
Tada *et al*. (2011:149–152)	0.5 wt.% Ru/Al_2O_3 & Ru/TiO_2	Fixed bed quartz	0.154% CO, 15.5% CO_2, 63.3% H_2 and 22.0% H_2O	150–300°C	11 000 h^{-1}	CO product concentration: <500 ppm from 192 to 215°C (Ru/Al_2O_3) and from 191 to 253°C (Ru/TiO_2). CO_2 conversion: < 1%.
Tada *et al*. (2014:60–65)	10 wt.% Ni/TiO_2 and 0.5 wt.% Ru/10 wt.% Ni/TiO_2	Fixed bed tubular	0.2% CO, 16.1% CO_2, 65.3% H_2 and 18.4% H_2O	150–300°C	2 500 h^{-1} for Ni/TiO_2 and 10 000 h^{-1} for $Ru/Ni/TiO_2$	CO and CH_4 respective product concentrations were <100 ppm and <1% at from 40 to 50°C.

2.4.1.4. Kinetics of the reactions involved in the CO selective methanation process

Several kinetic expressions have been reported for the methanation of carbon oxides. According to Inoue and Funakoshi (1984:603–604), the hydrogenation of CO on Ni metal is described by a Langmuir rate equation, with the rate varying proportionally to the square root of the partial pressure of CO. The rate laws for CO (Eq. 2.3) and CO_2 consumption (Eq. 2.4) via methanation are as follows:

$$-r_{CO} = \frac{k_{CO}\, P_{H_2} {P_{CO}}^{1/2}}{1+K_{CO}P_{CO}} \tag{2.6}$$

$$-r_{CO_2} = \frac{k_{CO_2}\, P_{H_2} {P_{CO_2}}^{1/3}}{\left(1+K_{CO_2}P_{CO_2}+k_{H_2}\, P_{H_2}+k_{H_2O}P_{H_2O}\right)^2} \tag{2.7}$$

Xu and Froment (1989:92) studied steam reforming of CH_4, WGS and methanation of carbon oxides over a $Ni/MgAl_2O_4$ catalyst. The rates of CO methanation (Eq. 2.8), WGS (Eq. 2.9) and CO_2 methanation (Eq. 2.10) reactions were found to be:

$$-r_{CO} = \frac{\frac{k_{CO}}{{P_{H_2O}}^{2.5}}\left(P_{CH_4}P_{H_2O}-\frac{{P_{H_2}}^3\, P_{CO}}{K_1}\right)}{DEN^2} \tag{2.8}$$

$$-r_{WGS} = \frac{\frac{k_{WGS}}{P_{H_2}}\left(P_{CO}P_{H_2O}-\frac{P_{CO_2}\, P_{H_2}}{K_2}\right)}{DEN^2} \tag{2.9}$$

$$-r_{CO_2} = \frac{\frac{k_{CO_2}}{{P_{H_2}}^{3.5}}\left(P_{CH_4}{P_{H_2O}}^2-\frac{{P_{H_2}}^4 P_{CO_2}}{K_3}\right)}{DEN^2} \tag{2.10}$$

$$DEN = 1 + K_{CH_4}P_{CH_4} + K_{CO}P_{CO} + K_{H_2}P_{H_2} + \frac{K_{H_2O}P_{H_2O}}{P_{H_2}} \tag{2.11}$$

Liu and Hinrichsen (2014:9350) modelled the fluid dynamics and kinetics of CO methanation over a $Ni/\gamma\text{-}Al_2O_3$ catalyst. The rate expressions used for CO methanation (Eq. 2.12) and WGS (Eq. 2.13) were respectively:

$$-r_{CO} = \frac{k_{CO}\, K_{CO}\, {P_{H_2}}^{1/2} {P_{CO}}^{1/2}}{1+\left(K_{CO}P_{CO}K_{OH}+\frac{P_{H_2O}}{{P_{H_2}}^{1/2}}\right)^2} \tag{2.12}$$

$$-r_{WGS} = \frac{k_{\mathrm{WGS}}\left[\left(K_{\alpha}P_{CO}P_{H_2O} - \left(P_{CO_2}\frac{P_{H_2}}{K_2}\right)\right)\right]}{{P_{H_2}}^{1/2}\left(1+K_{CO}{P_{CO}}^{1/2}+K_{OH}\frac{P_{H_2O}}{{P_{H_2}}^{1/2}}\right)^2} \quad (2.13)$$

Sun *et al.* (2018:38) simulated the production of syngas from CO using a fluidised-bed reactor containing a Ni/Al_2O_3 catalyst. Only CO methanation and WGS reactions (Eq. 2.14 & Eq. 2.15, respectively) were considered in the study, and are respectively:

$$-r_{CO} = \frac{\frac{k_{CO}}{{P_{H_2}}^{2.5}}\left(P_{CH_4}P_{H_2O} - \frac{{P_{H_2}}^3 P_{CO}}{K_1}\right)}{DEN^2} \quad (2.14)$$

$$-r_{WGS} = \frac{\frac{k_{WGS}}{P_{H_2}}\left(P_{CO}P_{H_2O} - \frac{P_{CO_2}P_{H_2}}{K_2}\right)}{DEN^2} \quad (2.15)$$

Garbis *et al.* (2019:3–6) studied the kinetics of CO and CO_2 methanation (Eq. 2.16 and Eq. 2.17, respectively) on Ru/Al_2O_3 and concluded that these reactions follow a Langmiur-Hinshelwood kinetic approach:

$$-r_{CO} = \frac{k_{CO}(T).C_{CO}.C_{H_2O}}{\left(1+K_{CO}.C_{CO}+K_{H_2O}.C_{H_2O}\right)^2} \quad (2.16)$$

$$-\mathrm{r}_{\mathrm{CO_2}} = \frac{k_{CO_2}(T).C_{CO_2}.C_{H_2}}{\left(1+K_{CO_2}(T).C_{CO_2}+K_{CO}(T).C_{CO}+K_{H_2O}.C_{H_2O}\right)^2} \quad (2.17)$$

2.4.2. CO removal by preferential oxidation

2.4.2.1. Reactions involved in the CO preferential oxidation process

In this process, the reformate gas from a WGS reactor is mixed with a controlled amount of air. CO is preferentially oxidised (Eq. 2.18) in a low temperature-operating reactor, while a limited fraction of H_2 also undergoes oxidation (as a secondary and undesired reaction, Eq. 2.19). Other secondary reactions that could take place include CO and CO_2 methanation (Eqs. 2.3 & 2.4), WGS and RWGS (Eq. 2.5), which will affect the composition of the product gas (Rosso *et al.* 2004:477–478; Laguna *et al.*, 2014:177; Han *et al.*, 2001:393).

$CO + ½\ O_2 = CO_2$ $\quad \Delta H = -282.98$ kJ/mol (2.18)

$H_2 + ½\ O_2 = H_2O$ $\quad \Delta H = -241.82$ kJ/mol (2.19)

Oxidation reactions (Eqs. 2.18 & 2.19) are both highly exothermic; therefore the equilibrium of these reactions are favoured at low temperatures. On the other hand, the reaction temperature needs to be sufficiently high to ensure fast kinetic rates towards the equilibrium conversion.

2.4.2.2. Parameters affecting CO preferential oxidation

As in the case of SELMET, the operating conditions of the reactor should be chosen as to treat CO in the gas mixture, yet minimise H_2 consumption by oxidation, which would decrease the energy content of the ultimate fuel.

a. Reaction temperature

CO oxidation and WGS are the desired reactions in the CO PROX process. The reaction temperature plays an important role in the activity and selectivity of the process, considering the number of possible secondary reactions at non-ideal operating temperatures. Caputo *et al*. (2007:335), observed that the CO oxidation light-off temperature (70°C) was lower than that of H_2 oxidation (120°C) on 4.2 wt.% CuO/CeO_2 catalyst. On a Pt-based catalyst, at low temperatures, CO covered most of the Pt-based catalyst surface and exerted an inhibitory effect to the oxidation of H_2 (Castaldi, 2010:334–336). Optimal reaction temperatures should therefore be between the CO light-off temperature and that of H_2. These temperatures vary according to the type of catalyst used. On a 1.5 wt.% Au/Al_2O_3 catalyst, Zou *et al.* (2007:785) showed that near-complete CO conversion could be achieved at a reaction temperature as low as -28°C. Laguna *et al.* (2014:182–184) studied CO PROX on a Au/Ce/Cu catalyst, and reported that the CO conversion reached a maximum in a temperature range of 100–200°C. In their work, the CO reaction selectivity decreased with an increase in temperature and O_2 content in the feed gas. At a O_2/CO ratio of 3/4, increasing the temperature from 100 to 200°C decreased the selectivity by roughly 30% (Laguna *et al*., 2014:183). Han *et al.* (2002:391) performed a kinetic study of CO PROX on a 5 wt.% Ru/Al_2O_3 catalyst, and reported that an increase in temperature from 125 to 175°C resulted in a CO conversion increase from less than 20% to 90% at an O_2/CO molar ratio of 1. Further increases in temperature at the same molar ratio resulted, first in a decrease in CO conversion, and then in an increase, due to the RWGS and methanation reactions, respectively.

b. Space velocity

Volumentric flow rates are essential so as to obtain the suitable residence times within the reactor. Cipti and Recupero (2009:127–128) theoretically studied the effects of different space

velocities (ranging from 4 000 to 8 000 h^{-1}) on Pt/Al_2O_3, and calculated that the best selectivities and CO product concentrations were found at low space velocities. Xu and Zhang (2006:70) investigated both CO oxidation and methanation on 0.5 wt.% Ru/Al_2O_3 and showed that at low space velocities (i.e. 4.25 $L.g_{cat}^{-1}.h^{-1}$), CO concentration could be reduced from about 1% to below 100 ppm. It was explained that increasing the space velocity would require higher amounts of O_2 in order to maintain the same CO conversion.

c. Feed composition

Components in the feed gas, such as O_2, H_2O and CO_2, have been reported to affect the performance of the catalyst in the removal of CO from H_2-rich gas streams. The O_2/ CO ratio, also expressed as O_2 excess factor $\lambda = 2O_2/CO$, is a parameter which determines the amount of air to be supplied to the system. On Pt/Al_2O_3 and $Ru/\alpha\text{-}Al_2O_3$ catalysts, it was observed that an excessive O_2/CO ratio resulted in a noticeable decrease in selectivity for CO oxidation (Cipti & Recupero, 2009:133-134; Kim & Park, 2010:49). In particular, Ru-based catalysts are susceptible to decreased catalyst performance with excess O_2, due to Ru having various metallic oxidation states (Castaldi, 2010:344).

H_2O is believed to act as a promoter of CO PROX. Its high heat capacity is an advantage in CO PROX since it prevents the reaction temperature to reach H_2 light-off temperature; thus keeping the selectivity towards CO oxidation high (Castaldi, 2010:341). Kung *et al.* (2002:429) reported that Au/Al_2O_3 loses its activity easily, and that the activity can be maintained when the gas stream is passed through a H_2O saturator at ambient temperature.

The presence of CO_2 in the feed gas is known to negatively affect the effectiveness of the CO PROX process. Laguna *et al*. (2014:183) studied $Au/CuO_x\text{-}CeO_2$ catalysts and reported that higher CO_2 in the inlet gas decreased the CO conversion at temperatures lower than 150°C. Li *et al.* (2013:3) also observed the CO_2 inhibiting effect at 80°C, on nanoporous gold particles; where the CO conversion decreased from 95% (CO_2-free gas) to 92% (10 vol.% CO_2 in the feed gas). Ruling out the possibilities of the RWGS reaction and catalyst deactivation by formation of carbonate species on the support, the possible cause for the lower performance was reported to be the inhibitory effect of the adsorption of CO_2 onto the catalyst active sites. For Xu and Zhang (2006:73) however, CO_2 did not greatly affect the performance of Ru/Al_2O_3 catalysts studied for CO oxidation or methanation.

2.4.2.3. Catalysts

A catalyst suitable for the PROX of CO should have the following characteristics (Li *et al.*, 2013:1; Mishra & Prasad, 2011:5):

- High CO oxidation activity
- Low H_2 oxidation activity
- Provide acceptable kinetic turn-over rates at low temperature
- Stability and tolerance to CO_2 and H_2O

Estifaee *et al.* (2014:1156) identified five groups of CO PROX catalysts: supported Pt catalysts, supported Pd catalysts, supported Ru catalysts, supported Au catalysts and non-noble metal oxides. A lot of research has been done on Pt-based and non-noble metal oxides such as CuO/CeO_2, which are known to be highly active at certain operating conditions (Laguna *et al.*, 2014:177; Xu & Zhang, 2006:65). Ru-based catalysts are commonly available and more efficient to use than Pt, Pd, Rh and Co at atmospheric pressure conditions (Han *et al.*, 2002:389; Xu & Zhang, 2006:65). Kim and Park (2010:46–49) investigated CO oxidation on Ru, supported on different crystalline phases of Al_2O_3. A Ru-based catalyst (0.696 wt.% Ru/α-Al_2O_3) was reported to have the ability to chemisorb the smallest amount of CO and CO_2. This catalyst displayed the highest performance for CO PROX under realistic conditions (50 vol.% H_2, 1 vol.% CO, 1 vol.% O_2, 10 vol.% H_2O, 20 vol.% CO_2 and He). CO product concentrations of less than 10 ppm were obtained reaction temperatures between 110 and 130°C. In the same temperature range, the CO_2 selectivity was close to 80%, while CH_4 yield was negligible (<3%).

Au-based catalysts are well-known for their good oxidation performance at low temperatures (Zou *et al.*, 2007:785; Miao *et al.*, 2016:24603). Miao *et al.* (2016:24604–24605) further stated that Au nanoparticles have a tendency to agglomerate, subsequently limiting its practical application. During CO oxidation experiments, it was observed that promoting Au with Cu increased the temperature window for near complete CO conversion; this did not necessarily improve the resistance towards added CO_2 and H_2O in the feed gas.

The particle size of the catalyst has considerable importance in the oxidation of CO. Soliman (2019:2398) noted that during CO oxidation, catalyst activity generally increases with a decrease in catalyst particle size, until an optimum size is reached. For some time, Au-based catalysts have been considered inactive for CO oxidation. However, remarkable activity is

observed when Au particle sizes are below 4 nm, and the activity tends to increase with a decreasing dimension of the Au clusters (Overburry *et al*., 2006:56; Soliman, 2019:2398–2399). On a Ru/Al_2O_3 catalyst however, the CO oxidation activity tends to increase with the particle size, because of a weaker tendency of metallic Ru to oxidise (Kim *et al.*, 2012:132–134; Soliman, 2019:2399).

Catalyst loading is an important factor in the activity of CO oxidation. Zhu *et al*. (2007:93) studied CO oxidation on Au/SiO_2 and estimated the optimum Au loading to be between 1.1 and 2.5 wt.%. Further increase in the catalyst loading resulted in a decline in catalytic activity. Rosso *et al*. (2004:478) compared two Ru/Al_2O_3 catalysts of different loadings (0.5 and 1.0 wt.% Ru), and concluded that the activity and reaction selectivity was higher on the 0.5 wt.% Ru/Al_2O_3 catalyst, which was less prone to catalyse undesired side reactions; i.e. RWGS and methanation.

The mutual interactions between the catalyst support, the active metal and the reacting gas mixture have often been reported to influence the efficiency of the CO removal process. Some of the most popular supports used for CO PROX catalysts include Al_2O_3, $CuO\text{-}CeO_2$, Fe_2O_3, SiO_2, TiO_2, ZiO_2 and zeolites (Mishra & Prasad, 2011:5; Uriz *et al*., 2013:284; Zhu *et al.*, 2007:89). Al_2O_3 is commonly used as a support material in industrial catalytic processes because of its porous nature, high surface area and stability (Zou *et al.*, 2010:307). For CO oxidation, Au/Al_2O_3 catalysts can exhibit high or low activities depending on the preparation method of the active site (Kung *et al.*, 2003:425). One of the disadvantages of Al_2O_3-supported Au catalysts is its deactivation with reaction time. This is caused by the formation of an inactive carbonate intermediate that the noble metal forms with CO_2 (Zou *et al.*, 2007:785; Li *et al*., 2013:3). H_2O addition can prevent this type of deactivation by favouring the formation of an active bicarbonate: $Au\text{-}(CO_3H) + Al\text{-}OH = Au\text{-}(CO_3)\text{-}Al + H_2O$ (Zou *et al*., 2007:787). Al_2O_3-supported Ru catalysts have shown greater efficiency for CO oxidation compared to other popular catalysts such as Pt/Al_2O_3 and some Ru-based catalysts (Xu & Zhang, 2006:65; Kim & Park, 2010:42).

Catalytic activity for CO PROX is also influenced by catalyst pre-treatment methods. Zhu *et al*. (2007:90) observed that calcinations in O_2-He increased the activity of Au/SiO_2 pre-reduced in H_2-Ar. Costello *et al*. (2004:12529) mentioned that with Au/TiO_2 catalysts, treatment in H_2 at 200°C was more effective than calcination in O_2 at 400°C. On a $Au/\gamma\text{-}Al_2O_3$ catalyst, activities were found to improve with time-on-stream when calcinations temperatures were

below 300°C (Costello *et al.*, 2004:12529). Xu *et al.* (2007:42) reported that their untreated and unsupported Au nanoparticles exhibited excellent performance for the oxidation of CO. Most pre-treatment methods of Ru-based catalysts include a reduction step after calcination of the catalyst has been done (Han *et al.*, 2004:124; Xu & Zhang, 2006:67; Kim & Park, 2010:42; Rosso *et al*., 2004:476). However, the reduction conditions must be selected in order to avoid adverse changes in the catalyst properties which will lead to a decrease in its activity. For instance, on a Al_2O_3-supported Ru catalyst, complete CO elimination was observed between 120 and 160°C (Chin *et al*., 2005:131). The authors also reported that catalysts which were first calcined in 5 vol.% O_2/N_2, prior being reduced in 5 vol.% H_2/N_2, showed severe sintering, probably due to the formation of Ru oxide particles which rapidly sintered upon the reduction step. This is attributed to their weak attachment to the metal support.

Ru and Au catalysts are promising catalysts for PROX of CO contained in H_2-rich gas streams. Their associated performances, as well as for other catalysts published in the literature, are summarised in Table 2.4.

Table 2.4. A summary of literature on the PROX of CO on Ru- and Au-based catalysts

Reference	Catalyst used	Reactor technology	Feed composition (vol.%)	Temperature	Space velocity	Performance
Calla and Davis (2005:5404–5407)	1.16 wt.% Au/Al_2O_3	Fixed bed quartz	1% CO, 2% O_2, 40% H_2 and He	90°C	45–3 000 $L.g_{cat}^{-1}.h^{-1}$	CO conversion: 56%. Selectivity: 50 to 60%.
Chen *et al*. (2004:102–106)	$Rh/\gamma Al_2O_3$ $Rh\text{-}K/\gamma Al_2O_3$	Microchannel and monolith	40% H_2, 1% CO, 20% CO_2, 1% O_2 and N_2	200–450°C	Microchannel reactor: 100 000 to 500 000 h^{-1} Monolith reactor: 20 000 h^{-1}	$Rh\text{-}K/\gamma Al_2O_3$ microchannel reactor: CO conversion: 99.5% at 80–220°C and 100 000 h^{-1}; 96.8% at 200–250°C and 500 000 h^{-1}.
Costello *et al*. (2004:12532)	1wt.% $Au/\gamma\text{-}Al_2O_3$	Flow-through microreactor	1% CO, 0.5% O_2, 40.5% H_2 and He	100°C	300 $L.g_{cat}^{-1}.h^{-1}$	Initial CO conversion: 69%
Galletti *et al*. (2008:3046–3048)	0.5–1 wt.% Rh supported on γAl_2O_3, CeO_2, TiO_2 and zeolite	Microchannel	1% CO, 2% O_2, 5% H_2O, 18% CO_2, 37% H_2 and He	50–250°C	60 $L.g_{cat}^{-1}.h^{-1}$	On Ru/Al_2O_3-zeolite: CO <10 ppm at 120–180°C. Maximum selectivity for all catalysts: 25%.

Table 2.4. A summary of literature on the PROX of CO on Ru- and Au-based catalysts (continued)

Reference	Catalyst used	Reactor technology	Feed composition (vol.%)	Temperature	Space velocity	Performance
Grisel & Nieuwenhus (2001:49–53)	5 wt.% Au on Al_2O_3, Au/MnO/Al_2O_3, Au/MgO/Al_2O_3, and Au/MnO/MgO/Al_2O_3	Flow-through microreactor	2.29% H_2, 1.14% CO, 0.57% O_2 and He	25–400°C	2 500 h^{-1}	For Au/MgO/Al_2O_3, and Au/MnO/MgO/Al_2O_3 catalysts: CO conversion: >75% below 100°C. Selectivity: 90% below 100°C.
Kim and Park (2010:43,49)	0.7 wt.% Ru/α-Al_2O_3	Fixed bed	1% CO, 20 % CO_2, 1% O_2, 50% H_2, 10% H_2O and He	77–180°C	3 $L.g_{cat}^{-1}.h^{-1}$	CO product concentration: <10 ppm from 110–140°C. Selectivity: 50%.
Laguna *et al*. (2012:106–109)	CuO_x/CeO_2	Microchannel	1% CO, 2% O_2, 10% CO_2, 10% H_2O, 70% H_2 and N_2	120–260°C	60 $L.g_{cat}^{-1}.h^{-1}$	CO product concentrations <100 ppm at 180–220°C. CO selectivity: 25%.
Laguna *et al*. (2014:177–184)	15 wt.% CuO_x/CeO_2 12 wt.% CuO-0.9 wt.% Au/CeO_2	Fixed bed	0.3–2% CO, 0.5–3% O_2, 50% H_2, 0–10% CO_2, 0–10% H_2O and N_2	50–250°C	60 $L.g_{cat}^{-1}.h^{-1}$	On CuO_x-Au/CeO_2, CO conversions > 98% from 100 to 200°C. Selectivity: 30–100% (depending on temperature & composition).

Table 2.4. A summary of literature on the PROX of CO on Ru- and Au-based catalysts (continued)

Reference	Catalyst used	Reactor technology	Feed composition (vol.%)	Temperature	Space velocity	Performance
Li *et al.* (2013:1–7)	Nanoporous Au	Fixed bed quartz	1% CO, 1% O_2, 50% H_2, 10% CO_2, 10% H_2O in N_2	5–100°C	240 $L.g_{cat}^{-1}.h^{-1}$	In the absence of CO_2: CO product concentration: <1ppm. CO selectivity: 50–100%.
Marino *et al.* (2004:60–65)	2 wt.% Pt or 2 wt.% Ir or 1 wt.% Pd, all supported on $Ce_xZr_{(1-x)}O_2$, 3 wt.% Pt supported on Al_2O_3, SiO_2, MgO, La_2O_3, CeO_2	Fixed bed	70% H_2, 2% CO, 1% O_2 and N_2	50–300°C	60 $L.g_{cat}^{-1}.h^{-1}$	CO product concentration: 700 ppm for $Pt/Ce_{0.15}Zr_{0.85}O_2$ at 225–250°C. CO selectivity: 20%.
Miao *et al.* (2016:24604–24605)	1 wt.% Au/Al_2O_3 1 wt.% $Au-Cu/Al_2O_3$ 1 wt.% $Au-Cu/K-Al_2O_3$	Fixed bed quartz	1% CO, 1% O_2, 40% H_2, 20% CO_2, 10% H_2O in N_2	30–160°C	80 $L.g_{cat}^{-1}.h^{-1}$	CO conversion: 100% for $Au-Cu/K-Al_2O_3$ at 60–110°C. CO selectivity: 60%.
Rosso *et al.* (2004:476–478)	0.5 wt.% and 1 wt.% Ru/Al_2O_3	Fixed bed	37% H_2, 18% CO_2, 0.5% CO, 5% H_2O, 0.5% O_2 and He	70–300°C	67 000 h^{-1}	CO product concentration: <10 ppm for 0.5 wt.% Ru/Al_2O_3 at 120–180°C. CO selectivity: 50%.

Table 2.4. A summary of literature on the PROX of CO on Ru- and Au-based catalysts (continued)

Reference	Catalyst used	Reactor technology	Feed composition (vol.%)	Temperature	Space velocity	Performance
Snytnikov *et al*. (2010:924–928)	5 wt.% Cu/CeO_{2-x}	Microchannel	1.5% CO, 2.25% O_2, 57% H_2, 10% H_2O, 20% CO_2 and He	150–250°C	80–240 $L.g_{cat}^{-1}.h^{-1}$	For the reactor assembly, CO product concentration: <10 ppm between 230 and 240°C. Selectivity: ca. 30%
Srinivas *et al*. (2014:286–292)	2 wt.% Pt/Al_2O_3	Microchannel, packed bed	60% H_2, 1% CO, 1% O_2 in Ar	150–250°C	120 $L.g_{cat}^{-1}.h^{-1}$	On both reactors, CO conversion 85% at 210°C. Selectivity: ca. 40%.
Xu and Zhang (2006:65–67)	0.5 wt.% Ru/Al_2O_3	Fixed bed	0.5–1% CO, 0.3–0.51% O_2, 70% H_2, 29.1% CO_2	70–150°C	4.25 $L.g_{cat}^{-1}.h^{-1}$	CO product concentration: tens of ppm (oxidation and methanation). Selectivity: 40%.
Xu *et al*. (2007:42)	Unsupported Au	Fixed bed	1% CO, 10% O_2, 89% N_2	-30, 0 & 30°C	80 $L.g_{cat}^{-1}.h^{-1}$	CO conversion: 99.5% at 30°C.
Zou *et al*. (2010:307–308)	1.15 wt.% Au/Al_2O_3	Fixed bed	1% CO, 10% O_2 and N_2	-28 and 30°C	15 000 h^{-1}	100% CO conversion at 30°C (>160 h on stream)

2.4.2.4. Reaction kinetics

Studying CO oxidation on Ru/γ-Al_2O_3, Han *et al*. (2011:394) expressed the rate of CO oxidation as:

$$-r_{CO} = k_{CO}.{P_{CO}}^{a}.{P_{O_2}}^{b} \quad (2.20)$$

This study suggested that the reaction model follows a Langmiur-Hishelwood mechanism, in which a dense CO adlayer would limit O_2 adsorption on the catalyst.

Baughman *et al*. (2012:402–403) expressed the rate laws of CO PROX over several noble metals catalysts, which were considered as the best choice due to their good electrochemical performances. On Al_2O_3-supported Ru, the following rate expressions were derived for CO oxidation (Eq. 2.21), H_2 oxidation (Eq. 2.22) and the WGS (Eq. 2.23) reaction:

$$-r_{CO} = k_C \times \exp\left(-\frac{E_C}{R\times T}\right) \times {C_{CO}}^{a} \times {C_{H_2}}^{b} \quad (2.21)$$

$$-r_{H_2} = k_H \times \exp\left(-\frac{E_H}{R\times T}\right) \times {C_{O_2}}^{c} \quad (2.22)$$

$$-r_{WGS} = k_D \times \exp\left(-\frac{E_D}{R\times T}\right) \times \left(C_{CO}.C_{H_2O} - \frac{C_{CO_2}.C_{H_2}}{K_{eq}}\right) \quad (2.23)$$

where $K_{eq} = \exp\left(\frac{4\,577.8}{T} - 4.33\right)$ (equilibrium constant) (2.24)

Ojeda *et al*. (2012:96) studied the mechanism of CO oxidation over Au clusters, supported on Al_2O_3, TiO_2 and Fe_2O_3. Steady state was assumed for all the adsorbed species, and subsequently expressed the rate equation as:

$$-r_{CO} = \frac{\alpha.(P_{CO}.P_{O_2}.P_{H_2O})^2}{\left(1+K_1.P_{CO}+K_2P_{O_2}+K_3.P_{H_2O}\right)^2} \quad (2.25)$$

Uriz *et al*. (2013:284) studied PROX of CO over Au/CuO_x-CeO_2, and expressed the rates of CO oxidation (Eq. 2.26), H_2 oxidation (Eq. 2.27) and the RWGS (Eq. 2.28) reaction as follows:

$$-r_{CO} = \frac{k_{CO}.P_{CO}.{P_{O_2}}^{1/2}}{\left(1+K_{CO_2}.P_{CO_2}+K_{O_2}{P_{O_2}}^{1/2}\right)^2} \quad (2.26)$$

$$-r_{H_2} = k_{H_2}.P_{H_2}.{P_{O_2}}^{1/2} \quad (2.27)$$

$$-r_{RWGS} = k_{RWGS}\left(P_{CO_2}.P_{H_2} - K_{WGS}.P_{CO}.P_{H_2O}\right) \quad (2.28)$$

These expressions were also used by Arzamendi *et al.* (2011:590–591), who compared CO removal via PROX on Au/CeFe and CeCu catalysts and suggested that simple rate laws sometimes failed to describe the effect of O_2 and CO_2 concentrations.

2.5. Reactor technology options for CO removal by chemical reaction

CO SELMET and CO PROX have been studied in numerous reactors at industrial and R&D scale. The fixed bed reactor is the most popular, probably due to the simplicity of the packed catalytic bed and its widespread use in the industry. Castaldi (2010:345) mentioned the monolith reactor and other short contact time reactors are suitable for CO oxidation. Microchannel reactors are a more recent technology, but show promising efficiency via improved transport phenomena, and have been used for both CO methanation and oxidation in laboratory investigations.

2.5.1. Fixed bed reactors

The fixed bed reactor consists of a reactor shell in which a catalyst is placed in a structured manner. Both surface catalysed and porous catalysts can be used in the case of the fixed bed reactor. High CO removal efficiencies have been reported for processes carried out in packed/fixed bed reactors (Galletti *et al*., 2010:590–596; Miao *et al.*, 2016:24603–24609). In some cases, heat and mass transfer limitations can occur, resulting in uneven temperature distributions, hotspot formation, increased reactor pressure drop and channelling at high throughput. It was noted that these problems could be overcome by using structured packing, rather than random packing in the reactor (Laguna *et al.*, 2012:105; Holladay *et al.*, 2004:4770. Roy *et al.*, 2004:2919).

Fig. 2.5. Schematic of a packed bed reactor

2.5.2. Monolithic reactors

Monolithic reactors are characterised by a single reactor substrate that supports several parallel channels, which could be at the micro- or meso-scale. There is often reference to a "honeycomb" structure when describing monolithic reactors. Many processes have been performed in monolithic reactors; they include adsorption, distillation, and CO and NO_x removal in autocatalytic converters (Roy *et al.*, 2004:2919). Monolithic reactors are commonly made of ceramics or metals such as copper, aluminium or stainless steel (Danaci, 2017:45). They have several advantages, including their good mechanical and thermal properties, high specific surface area, high interface mass transfer as well as simple scalability (Tomasic & Jovic, 2006:113). Chen *et al.* (2004:104) used a monolithic reactor for the PROX of CO in a H_2-rich gas initially consisting of 5000 ppm CO. Excellent CO conversions (>99.8%) and selectivities (>80%) were obtained in a temperature range of 170–240°C at a space velocity of 20 000h^{-1} on Rh-K/Al_2O_3 catalyst.

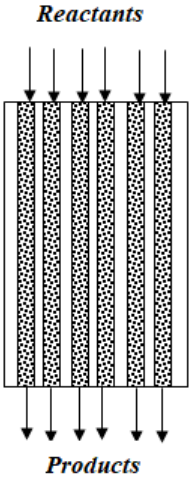

Fig. 2.6. Schematic of a monolithic reactor (Castaldi, 2010:346).

2.5.3. Microchannel reactors

Microchannel reactors consist of a structure containing a large number of small channels in the micro-scale dimension (i.e. ~10–1000 µm), which have been machined or chemically etched on reactor substrate's surface (Castaldi, 2010:349; O'Connell, *et al.*, 2012:12). Each microchannel reactor may contain hundreds or even thousands of parallel microchannels, and must be configured in order to minimise flow maldistributions between the channels (Rouge *et al*, 2001:1419). They have a large specific surface area which varies between 10 000 and 50 000 m^2/m^3 (Castaldi,

2010:349). Catalyst deposition in microchannel reactors can be in a packed form, or washcoated to the surface of the microchannel walls. Microchannel reactors are robust and mostly made of medium to high thermal performance materials such as stainless steels, copper, or silicon carbide ceramic, or in other instances low conductivity ceramic such as alumina (Yao *et al.*, 2015: 520).

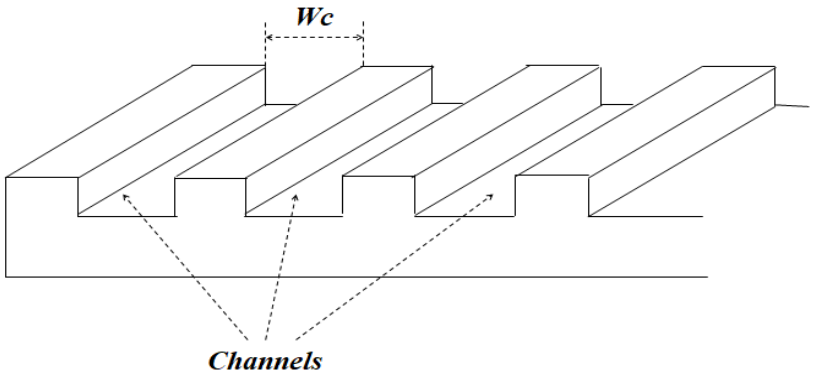

Fig. 2.7. Schematic of the plate of a microchannel reactor

Compared to large-scale reactors, microchannel reactors have a much larger surface-to-volume ratio, improved heat and mass transfer, which increases their size comparative performance, and makes them suitable for temperature control of highly exothermic and endothermic reactions (Gokhale *et al.*, 2005:25–26). The small width of microchannels shortens the diffusion paths of reacting species, thus increasing mass transfer in the reactor (Adeosun & Lawal, 2005:108). Therefore, less catalyst is needed to coat the microchannel walls to achieve performances similar to that of conventional reactors. They also present the advantage of being compact, a feature which makes them suitable for portable applications (Ndlovu *et al.*, 2018:487).

Castaldi *et al.* (2010:349) stated that microchannel reactor size can be significantly lower than that of systems using catalyst pellets. Their ability to integrate heat and mass transfer reduces the number of auxiliary process components required for efficient and safe operation (Gokhale *et al.*, 2005:24). In addition, microchannel reactors improve conversion and selectivity towards desired products through precise reaction control, even when short residence times are imposed on the reactor (Gokhale *et al.*, 2005:24).

2.5.3.1. Fabrication techniques

Different methods can be used during the fabrication of microchannel plates. The first is the LIGA (Lithographie, Galvanoformung, Abformung), a German-developed method which is designed to

integrate deep lithography, electroplating and molding in the fabrication process (Jensen, 2001:294; Holladay *et al*., 2004:4769; Yao *et al*., 2015:520).

The second is the etching process which can be wet or dry. The wet etching process uses a liquid etching solution which removes unwanted material from the plate. The dry etching process uses plasma instead of a liquid solution (Holladay *et al*., 2004:4769).

Micromachining is the third technique; it involves milling techniques with low machining tolerances. Micromachining also consist of radiation by a laser beam or sparks in a dielectric fluid to remove material and print the channel feature on the plate (Holladay *et al*., 2004:4769–4770). For large scale production, punching and embossing are inexpensive methods that can be used for the creation of holes or microstructures on the substrate (O'Connell *et al*., 2012:12).

Fourthly, soft lithography is a low cost and fast procedure which makes use of an elastomer with a pattern on its surface, which will be transferred to a substrate (Jensen, 2001:295; Holladay *et al*., 2004:4770). When patterns have been printed on the sheets, lamination is then used for stacking several sheets together in a single device (Dritz *et al*., 2011:4; Holladay *et al*., 2004:4770).

2.5.3.2. Catalyst deposition methods

Catalysts can be deposited by washcoating, aerosol spray, and chemical or physical thin film deposition techniques (Jensen, 2001:295; Holladay *et al*., 2004:4770). Washcoating results in thin layers and high catalyst surface area. Aerosol spray allow for more precision in the catalyst deposition method. Chemical and physical vapour deposition techniques yield thinner catalyst layers and higher surface areas than the other mentioned techniques (Holladay *et al*., 2004:4770).

2.5.3.3. Disadvantages of microchannel reactors

Several advantages of microchannel reactor technology have been discussed. Their enhanced heat and mass transfer capabilities, coupled with their small geometric features, enable them to perform single and multiphase reactions efficiently and safely (Jensen, 2001:293).

Nevertheless, microchannel reactors also have drawbacks. Castaldi *et al*. (2010:350) suggested that microchannel reactors are unsuitable for precipitation reactions. The microchannels are easily clogged with particulate matter and their performance is reduced with fouling. Besides, the substrates of which microchannels are made may not always be compatible with the processed

chemicals. Microfabrication techniques must be precisely executed, otherwise the flow patterns of microchannel reactors will be compromised. In addition, careful selection of the reactor material is necessary to ensure durability. Holladay *et al*. (2004:4768) mentioned that microreactors operating at high throughput could be susceptible to increased pressure drop across the reactor. Lastly, Chiuta *et al*., (2015:11392) pointed out the difficulty in measuring process parameters during operation of the microchannel reactor.

2.5.3.4. Application of microchannel reactors for CO removal from hydrogen-rich gas streams

Enhanced heat transfer capabilities of microchannel reactors enable them to perform both highly endothermic and exothermic reactions. A variety of processes have been carried out in microchannel reactors, including: Fischer-Tropsch synthesis (Lerou *et al.*, 2010:381), CH_4 steam reforming (Arzamendi *et al.*, 2009:168–173), H_2 production from ammonia decomposition (Chiuta *et al.*, 2015:2921–2926), formic acid decomposition (Ndlovu *et al.*, 2018:485–497), dehydration of isopropanol (Rouge *et al*., 2001:1419–1427), gas-solid-liquid hydrogenation reactions, polymerization reactions (Gokhale *et al*., 2005:23), methanation of carbon oxides (Engelbrecht *et al.*, 2017a:847–857; Liu *et al.* 2012:599–605). The small dimensions of microchannels act as an inherent safety mechanism that enable flame prevention. Safer operations of processes involving highly explosive mixtures such as ethylene oxide synthesis (Bac & Avci, 2019:2) and H_2 oxidation to H_2 peroxide (Lerou *et al.*, 2010:383) are therefore possible.

SELMET and PROX of CO have mostly been investigated in packed-bed reactors, at least at industrial scale, while there is a limited amount of literature on the two processes studied within microchannel reactors. Currently there have not been many studies on kW-scale microchannel reactors used for CO abatement from H_2-rich streams. Kolb *et al.* (2008:485) developed a fuel processor incorporating a CO PROX step for a 5 kW fuel cell. Snytnikov *et al.* (2010:926) studied CO PROX in 26 parallel microchannel reactors (coated with a 5 wt.% Cu/CeO_{2-x} catalyst) designed for a 100 W PEMFC. The array of microchannel reactors was able to reduce CO content in a realistic reformate gas, from 1.5 vol.% to 10 ppm at temperatures between 230 and 240°C. The selectivity to CO_2 was about 35%.

Lee *et al*. (2014:423–424) studied the SELMET and PROX of CO (in series) in microchannel reactors using Pt/A-type zeolite and Ru/TiO_2 catalysts for the two processes, respectively. Separate

preliminary tests on each of the two reactors showed that 1 vol.% CO could be reduced to less than 10 ppm in the PROX reactor at close to 80°C, while a temperature range of 214–277°C was suitable for selective CO methanation. These experiments were carried out at a space velocity of 30 000 h^{-1}. In a system combining the two reactors in series, with the PROX reactor upstream of the methanation reactor, the overall CO product concentration of the system was maintained below 10 ppm at a O_2/CO ratio of 1, at temperatures ranging from 141 to 248°C.

Men *et al*. (2007:87) studied the methanation of carbon oxides on Ni/CaO/Al_2O_3, stating that the microchannel reactor provided opportunities to study different reaction pathways in a wide range of operating parameters. Görke *et al*. (2005:136) recorded methanation conversions as high as 95% and selectivities of 82 and 99% on Ru/SiO_2 and Ru/Al_2O_3 catalysts, respectively. The authors reported that the microchannel reactor enabled precise control of reaction temperatures; thus maximizing CO conversion, and supressing the conversion of CO_2 towards CH_4 (Görke *et al*., 2005:138).

Galletti *et al*. (2008:3047) investigated CO PROX in a microchannel reactor coated with a Rh/(50 wt.% γ-Al_2O_3+ 50 wt.% zeolite) catalyst. For an O_2/CO ratio of 1.5, CO concentrations were reduced from 1% to 10 ppm at temperatures of 140–220°C. Chen *et al*. (2004:105) indicated that improved CO oxidation performance in a microchannel reactor was attained over a Rh-K/Al_2O_3 catalyst, compared to that of a monolithic reactor. High space velocities (100 000–500 000 h^{-1}) were tested in both reactors. The CO conversion could be maintained as high as 93% using the microchannel reactor at the 500 000 h^{-1} space velocity condition, whereas the CO conversion decreased to less than 80% at 400 000 h^{-1} in the monolithic reactor. These results confirmed that the microchannel reactor supported very good overall reaction kinetics. Srinivas *et al*. (2004:291–293) compared the performance of a silicon microchannel reactor to that of a packed bed reactor for CO oxidation, and showed that their performances were similar (85% CO conversion at 210°C) at the same space velocity (120 $L.g_{cat}^{-1}.h^{-1}$). On the other hand, benefits of microchannel reactors over packed-bed reactors include the integration of structural and functional features, more design considerations to limit pressure drop, efficient heat management and ease of scaling out reactor size.

Scaling-out microchannel reactors consists of increasing the number of parallel microchannels or connecting parallel channel clusters, with minimal changes in fluid dynamic effects (Tonkovich *et*

al., 2005:635). Of course, heat management and flow distribution needs to be accounted for, as the reactor scale becomes larger. As soon as microchannels are made significantly longer, for instance, some redesign is necessary (e.g. size of distribution manifolds and hydraulic diameter of microchannels need to be recalculated to account for pressure drop effects) (Tonkovich *et al*., 2005:637). Microchannel reactors in parallel make it possible to replace reactor sections without having to shut down entire processes (Atkinson & McDaniel, 2010:97).

2.6. Computational Fluid Dynamics (CFD) Modelling

Understanding the kinetics of the CO SELMET and CO PROX reactions, as well as the heat and mass transfer phenomena within the unknown space of microchannels can be especially useful to predict the performance of the microchannel reactor during the abatement of CO from H_2-rich streams. It is not practical to accurately measure process parameters within a microchannel reactor during operation; and even if traditional methods of measurement were used, they would interfere with the local flow field inside the reactor. CFD modelling enables to simulate the reactions, the flow characteristics as well as the heat and mass transfer inside the reactor (Chiuta *et al*., 2014:11392).

An accurate CFD model would describe experimental data over a wide range of operating parameters, i.e. temperature and space velocity. In the past in our research group, Chiuta *et al*., (2014:11392–11395) described the development of a CFD model based on a microchannel reactor for the ammonia decomposition process using COMSOL Multiphysics® software. A 3D geometry was developed which represents the exact dimensions of the reactor substrate and catalyst washcoat, subject to certain symmetric assumptions to limit the solution time. In general, a CFD model of a chemical process requires input of transport phenomena, thermodynamics and the kinetic aspects of the reactions involved, expressed as mathematical governing equations and boundary conditions (Laguna *et al*., 2012:106). Engelbrecht *et al*. (2017a:850–857) studied CO_2 methanation in the same reactor geometry, and used the CFD to model and accurately validate the experimental reactor.

Thus far, CFD modelling has not been used often for SELMET and PROX of CO in H_2-containing gas streams. Uriz *et al*. (2013:283–291) studied PROX of CO over a Au/CuO_x-CeO_2 catalyst using ANSYS® CFX software. A microchannel reactor was used for the experiment work as well. The

model revealed that the microchannel reactor could efficiently reduce the CO level from 1 vol.% to tens of ppm under specific conditions of temperature and at specific ratios of O_2/CO.

Arzamendi *et al*. (2011:588–595) also used ANSYS® CFX software to carry out 3D simulations of the CO PROX over Au/Ce-Fe and Ce-Cu catalysts in a microreactor. The two model geometries consisted of (i) square parallel microchannels, and (ii) parallel microliths, which were compared and found to perform similarly for CO PROX.

Several reasonable assumptions can be made to simplify a CFD model. For instance, Laguna *et al*. (2012:107) modelled the CO PROX process over a CuO_x/CeO_2 catalyst in a microchannel reactor; assumptions included: steady state and isothermal conditions, and uniform catalyst deposition in the microchannel reactor. Their modelling observations were very similar to the experimental measurements. They indicated that the region for maximum CO conversion falls in a temperature range of 180–220°C, and predicted a decrease of CO selectivity at higher reaction temperatures (Laguna *et al.*, 2012:108).

In conclusion, microchannel reactors can be categorised as process equipment that provide characteristics which are often referred to as "process intensifying". These include very fast heat and mass transfer (in some cases the absence of any limitations), kinetics close to that which can be describes as intrinsic (due to minimal diffusional effects), and micro-scale dimensions. Conventional reactors can be described with well-known design equations; microchannel reactors however not so easily due to the above mentioned characteristics. CFD modelling is therefore a promising tool to describe these unknowns within the dynamic reaction space of a microchannel reactor during CO SELMET and CO PROX.

CHAPTER 3. EXPERIMENTAL PROCEDURE

In this chapter, the experimental setup, as well as the method followed throughout the investigation will be described. Section 3.1 will briefly describe the characteristics of the microchannel reactors used in this project. The Ni, Ru and Au catalysts used during the microchannel washcoating will be introduced in Section 3.2. The design of experiments will be summarised in Section 3.3, while Section 3.4 will stipulate the methods used during the thermodynamic equilibrium calculations using ASPEN Plus software. For all experiments, the volumetric flow rate and space velocity were expressed in normal conditions of temperature and pressure (293.15 K and 1 atm) as $Nml.min^{-1}$ or $NL.g_{cat}.h^{-1}$.

3.1. Microchannel reactors

The three microchannel reactors that were used in this project are identical in their geometry and in the material used to manufacture them. They only differ in the catalyst coated on the wall surface of their channels. They were designed and constructed by Fraunhofer-IMM (Mainz, Germany). Each reactor, manufactured of stainless steel 314, consisted of one microchannel plate, and one cover plate. The first plate (Fig. 3.1a) was 2 mm thick and contained 80 microchannels and two fluid distribution manifolds engraved on its surface, using a wet chemical etching technique (O'Connell *et al*., 2012:12). The microchannel were 250 µm wide, 150 µm high and 5 cm long. They were separated by 250 µm-wide fins.

The second (Fig. 3.1b), which was laser-welded on the first, contained no channels, but two mirror manifolds for the inlet and outlet, which corresponded to those on the microchannel plate. The inlet and outlet manifolds, shown in Figs. 3.1a and 3.1b, allowed for uniform fluid distribution due to their triangular shapes, and minimised the formation of dead volumes within the microchannel reactor.

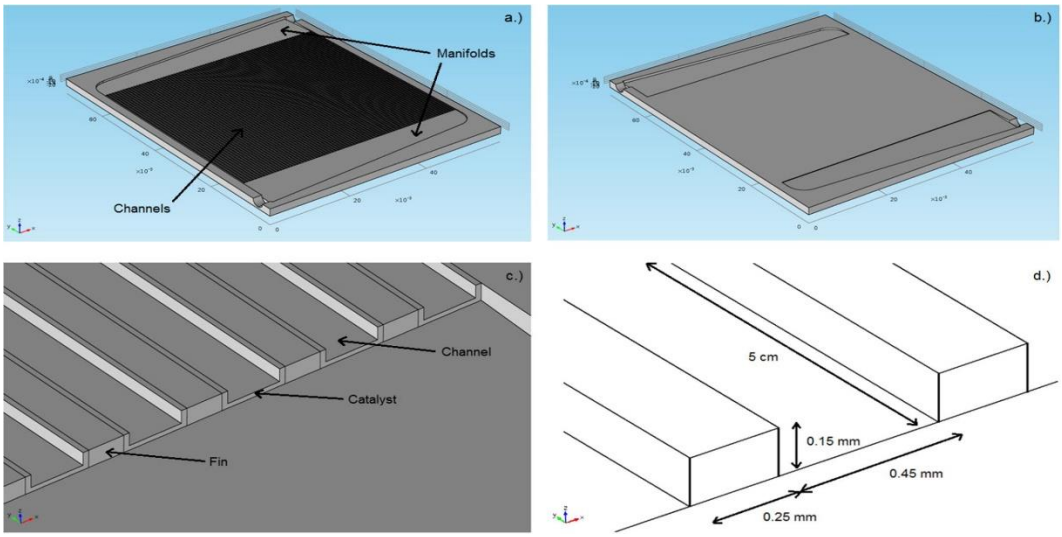

Fig. 3.1. (a) Microchannel reactor plate with 80 microchannels engraved on it. (b) Cover plate containing no microchannels, but two fluid distribution manifolds, and laser welded to the microchannel plate. (c) Representation of the structure of five adjacent microchannels. (d) Dimensions of a microchannel which is not coated with catalyst (Engelbrecht et al., 2017a:849)

Two 1/8 inch stainless steel pipes were welded at the inlet and outlet of the microchannel reactor. In addition, two heating cartridges were inserted into a heating block, which supported the reactor. For reaction temperature measurements, two small boreholes within the heating block (2 mm diameter), and near the wall of the reactor, were fabricated for thermocouples to be inserted at a later stage.

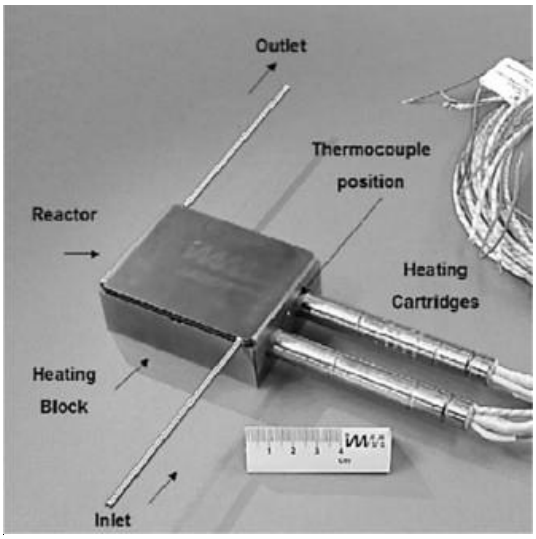

Fig. 3.2. An image of the microchannel reactor, inlet and outlet piping, heating block and cartridges heaters (Chiuta et al., 2015:2922)

3.2. Catalysts

O'Connell *et al*. (2012:12) described the catalyst washcoating, drying and calcination methods, which were used to apply to catalysts to the three microchannel reactors used in this project. Each reactor contained a total of 92 mg of the catalyst, with a thickness of 40 μm applied to the respective microchannels. The catalyst coatings were subjected to a series of impact tests, and demonstrated good adhesion and uniformity, before the reactor was laser welded with the cover plate. The three catalysts are described below.

3.2.1. Ni-based catalyst

Firstly, a Ni-Pt bimetallic catalyst (ActiSorb® O6), supplied by Clariant, was used. XRD tests showed that it consisted of 4.7 wt.% Ni and 0.1 wt.% Pt on γ-Al_2O_3. The Ni-coated microchannel reactor was formerly used for a project to decompose ammonia to produce H_2, intended for fuel cell power applications (Chiuta *et al.*, 2014a:7228).

3.2.2. Ru-based catalyst

A commercial Ru-based catalyst (10010™) was obtained from Acta S.p.A (Crespina, Italy). The catalyst consisted of a 8.5 wt.% Ru-Cs active metal, supported on Al_2O_3. A BET surface area analysis revealed that the catalyst supported a surface area of 113 $m^2.g^{-1}$ and pore volume of 0.30 $cm^3.g^{-1}$. It has previously been used for ammonia-to-hydrogen (Chiuta *et al*., 2015:2923) and CO_2 methanation applications (Engelbrecht *et al*., 2017a:849).

3.2.3. Au-based catalyst

Lastly, a commercial 1.15 wt.% Au/Al_2O_3 catalyst (79-0160™) from Mintek (South Africa) was used to washcoat the third microchannel reactor. The results of BET analysis showed that the surface area of the washcoated catalyst was 130 m^2/g. This reactor was previously used for the decomposition of formic acid towards H_2 production (Ndlovu *et al*., 2018:487).

3.3. Experiment design

Prior to the experiments, the reactors were heated in a flow of N_2 (50 $NmL.min^{-1}$ or 32.6 $NL.g_{cat}^{-1}.h^{-1}$), then reduced in H_2 flow (same flow rate) at a temperature which depended on the specific

catalyst in the reactors (300°C was used for Au, 700°C for Ni and 400°C for Ru). After reduction, a flow of N_2 (50 NmL.min^{-1}) was used to cool the reactor to the desired reaction temperature.

The experimental operating conditions were estimated during a preliminary investigation in which the effects of parameters (i.e. temperature, space velocity and feed composition) on the reactor performance were tested.

Throughout all the investigations, a one-factor-at-a-time procedure was followed. Each experiment was conducted under isothermal conditions and at constant space velocity within 2.5 h of steady operation, and product gas samples were taken every 15 min. Each final experimental data point is presented as an average of the 10 samples taken during that particular experiment. After the primary experiments, data repeatability was investigated with a set of 4 experiments at conditions for which some of the best reactor performances were obtained.

3.3.1. Methanation reaction

The methanation reaction is affected by several key parameters. Temperature is one of the most important factors because of the exothermic nature of the CO and CO_2 methanation reactions. The space velocity is also critical, as sufficient residence time is required for reaction to take place. These parameters were varied within ranges that were inspired from literature findings. The parametric ranges for temperature and flow rate are summarised in Table 3.1.

Table 3.1. Reaction parameters varied during the SELMET of CO

Parameter	Range
Temperature	280–400°C, in increments of 20°C.
Flow rate	50 and 100 NmL.min^{-1} (space velocity: 32.6 and 65.2 NL.g_{cat}^{-1}.h^{-1})

3.3.2. Oxidation reaction

As in the case of CO methanation, temperature and flow rate are important factors to consider for the exothermic CO oxidation reaction. The composition of the feed gas, especially the O_2/CO ratio, is also important in order to obtain maximum CO conversion and high selectivity. These parameters were varied within ranges that were inspired from literature findings. They are summarised in Table 3.2.

Table 3.2. Reaction parameters varied during the PROX of CO

Parameter	Range
Temperature	80–200°C, in steps of 20°C.
Flow rate	50–200 NmL.min^{-1} (space velocity: 32.6–130.4 NL.g_{cat}^{-1}.h^{-1}), in steps of 50 NmL.min^{-1}.
O_2/CO ratio	0.7, 1.4 and 2.8

3.3.3. Apparatus

Figure 3.3 is a schematic representation (PFD) of the experimental setup used for both CO SELMET and CO PROX processes. In Fig. 3.3, a specialised gas bottle with a mixture of CO/H_2 was used for both CO methanation and oxidation. The pure H_2 stream was used during the reduction of the catalysts. In addition, an O_2/N_2 specialised gas mixture was used during CO oxidation, while only the N_2 stream was used as an inert gas during methanation (absence of O_2). The third gas feed, pure CO_2, was also used in both CO SELMET and PROX processes.

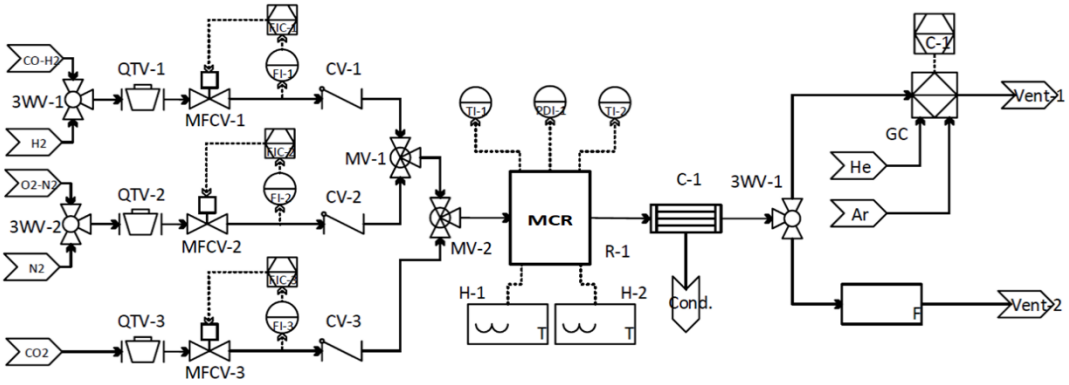

Fig. 3.3. PFD diagram of the experimental setup used in the project

Main components		**Valves**	
FIC-1,2,3	: Flow controller	3WV-1,2	: Three-way valve
Fl-1,2,3	: Flow indicator	QTV-1,2,3	: Quarter-turn valve
Tl-1,2	: Thermocouple	MFCV-1,2,3	: Mass-flow control valve
MCR (R1)	: Microchannel reactor	CV-1,2,3	: Non-return (check) valve
H-1,2	: Heating cartridges	MV-1,2	: Mixing valve
C-1	: Condenser		
GC	: Gas chromatograph		
F	: Flow meter		

A model gas stream, simulating a dry reformate gas from a WGS reactor, was mixed using the feed streams described above, and fed to the microchannel reactor. Three flow controllers (Brooks SLA5850) were used in order to obtain the desired composition of the feed gas. For SELMET experiments, the feed contained: 68.53 vol.% H_2, 1.47 vol.% CO, 10 vol.% CO_2 and 20 vol.% N_2. On the other hand, for the PROX experiments, some N_2 was replaced with O_2 in order to initiate the oxidation of CO. The feed consisted of: 68.6 vol.% H_2, 1.4 vol.% CO, 10 vol.% CO_2 and 1.0–4.1 vol.% O_2 and balance N_2.

The mixture gas was fed to a microchannel reactor containing one of the three catalysts (Ni, Ru and Au). Two 300W Watlow FIREROD® heating cartridges were used to control the reaction temperature at isothermal conditions. Two K-type thermocouples were placed in the boreholes described earlier to verify the reaction temperature.

The outlet gas was dried using silica beads. The dry product gas was analysed using an online gas chromatograph (SRI 8610 GC), fitted with a HayeSep D column and two molecular sieve (MS-13X) columns. The GC also contained a helium ion detector (HID) and two thermal conductivity detectors (TCD), which were capable of detecting CO levels below 50 ppm. One of the MS columns was used to separate the lighter gas products (H_2, N_2, O_2, CH_4, and CO) with argon as carrier gas, and analysed using a TCD. On the other hand, CO_2 was trapped using helium as carrier gas in the HayeSep D column. A stop-flow solenoid was used to elude and analyse the CO_2 at a later stage than the lighter gases. To verify mass balances, the product flow rate was measured with a bubble flow meter at atmospheric conditions (around 25°C and 86 kPa), and converted back to normal flow conditions.

3.4. Thermodynamic equilibrium

CO abatement from a H_2-rich gas stream by SELMET or PROX involves a complex set of reactions that occur simultaneously, at different rates, depending on the reaction conditions. Equilibrium calculations assist in determining the possible product composition, and serve as a reference which can be used to evaluate the performance of the reactor. The equilibrium calculations were perform using Aspen Plus V8.6. A Gibbs reactor, with the Peng-Robinson fluid property package was selected for the calculations. All the reactants (H_2, O_2, CO and CO_2), with

N_2, CH_4, and H_2O were considered as possible products in the Gibbs free energy minimization technique. In the case of methanation, no O_2 was considered as a reactant or a product.

The methanation (Fig. 3.4) and oxidation (Fig. 3.5) reactions are highly exothermic, thus equilibrium favoured at moderate temperatures (<400°C). In both cases, CO and CO_2 equilibrium conversions were above 99.3% in the temperature range studied (80–400°C). The conversion of CO_2 in both cases are predominantly driven by its methanation reaction. Furthermore, it appears that the conversion of H_2 is slightly higher in the oxidation case (69.33% at 400°C), as all excess O_2 which does not convert CO in the feed gas combusts H_2. In the methanation case, the H_2 conversion is slightly lower (64.05% at 400°C). In general, it seems the reaction systems have a high potential to convert CO, CO_2 and H_2, and irrespective of temperature (at least below 400°C). It is therefore up to active and selective catalysts to convert CO from the H_2-rich gas stream, for both processes investigated. The effect of the reversible WGS reaction is not apparent from equilibrium calculations, and will be investigated during the experiments.

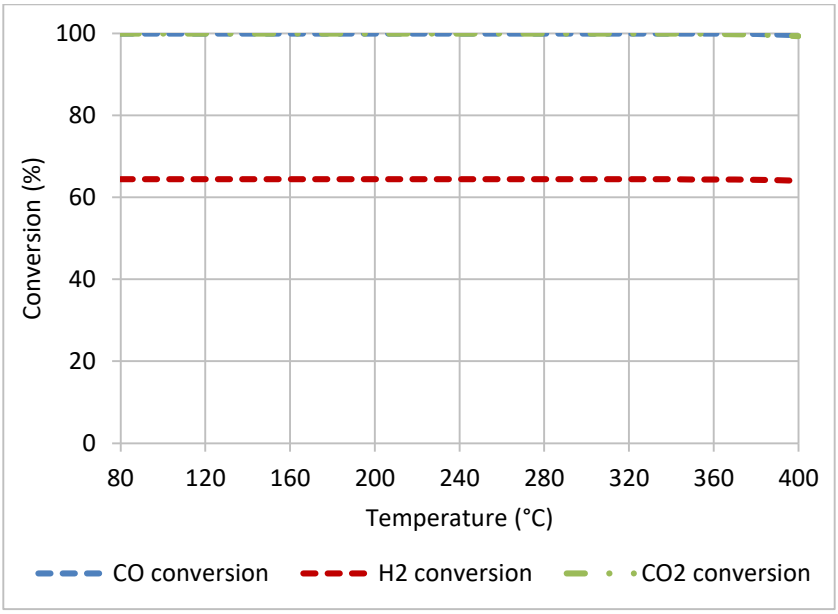

Fig. 3.4. CO, CO_2 and H_2 equilibrium conversions calculated for the CO SELMET case, in a temperature range of 80–400°C. The inlet gas composition was applied as specified in Section 3.3.3.

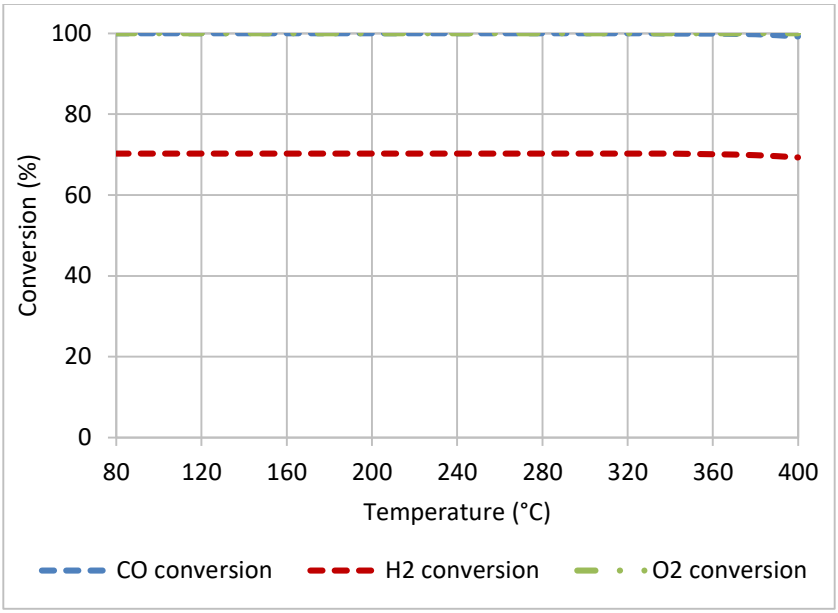

Fig. 3.5. CO, O_2 and H_2 equilibrium conversions calculated for the CO PROX case, in a temperature range of 80–400°C. The inlet gas composition was applied as specified in Section 3.3.3.

Two factors that hinder near-equilibrium conversion is the activity of the catalyst (kinetic turn-over rate at a certain temperature), and mass transport limitations. The two reaction parameters identified earlier – reaction temperature and residence time – are therefore crucial to vary in order to evaluate the two catalytic processes, and ultimately obtain high CO conversions as indicated by equilibrium. Obviously, the potential for H_2 and CO_2 consumption is also high due to the methanation reaction involving CO_2 (Fig. 3.4), and to a lesser extent the oxidation of H_2 with excess O_2 (Fig. 3.5). The selective catalysts within the microchannel reactors will therefore be required to deliver high CO conversions (close to equilibrium), while limiting any unnecessary conversion of H_2 (far from equilibrium).

CHAPTER 4. EXPERIMENTAL RESULTS AND DISCUSSION

In this chapter, the experimental performance evaluation of the microchannel reactors used during the course of this project are discussed. Three microchannel reactors, respectively coated with commercial Au, Ni and Ru-based catalysts were evaluated for CO SELMET and PROX. Of the three catalytic reactors, the Ru-coated reactor performed the best via the PROX of CO. The preliminary investigations of the oxidation of CO in the Au-coated reactor (Section 4.2.1), methanation of CO in the Ni-based reactor (Section 4.2.2) and methanation of CO in the Ru-coated reactor (Section 4.2.3) will be briefly described. Finally, the most satisfactory experimental results, which is the PROX of CO on Ru, is discussed in detail in Section 4.3, while a summary of the recommended operating conditions is given in Section 4.4.

4.1. Performance criteria

During both CO SELMET and PROX, the aim was to reduce the CO concentration in the product gas to levels below 100 ppm, while keeping H_2 consumption to a minimum.

4.1.1. Preferential oxidation

For the PROX of CO, the performance criterion of the microchannel reactor was based on the CO conversion (Eq. 4.1) and the selectivity (Eq. 4.2) towards CO oxidation. During oxidation, H_2 is also prone to be oxidised, which is why the selectivity parameter is important. These criteria are expressed as follows (Marino *et al.*, 2004:61):

$$CO\ conversion\ (\%): \quad X_{CO} = \frac{F_{CO_{in}} - F_{CO_{out}}}{F_{CO_{in}}} \times 100 \tag{4.1}$$

$$CO\ selectivity\ (\%): \quad S_{CO} = \frac{F_{CO_{in}} - F_{CO_{out}}}{2 \times \left(F_{O_{2in}} - F_{O_{2out}}\right)} \times 100 \tag{4.2}$$

Where F_i is the normalised volumetric flow rate of species i.

These expressions are valid under the assumption that all CO was converted via the oxidation reaction, and that no CO methanation took place at the relevant temperature and flow conditions investigated for oxidation. During the discussions of the PROX results (for both Au and Ru catalysts), references will be made to the absence of any CH_4 formed at all the experimental conditions investigated.

4.1.2. Selective methanation

During the methanation CO, the secondary methanation of CO_2 can also take place, as both gas species are reduced with H_2 to produce CH_4. The CO conversion (Eq. 4.3) and the selectivity (Eq. 4.4) towards CO methanation are expressed as follows (Men *et al.*, 2007:83):

$$CO\ conversion\ (\%): \quad X_{CO} = \frac{F_{CO_{in}} - F_{CO_{out}}}{F_{CO_{in}}} \times 100 \qquad (4.3)$$

$$CO\ selectivity\ (\%): \quad S_{CO} = \frac{F_{CO_{in}} - F_{CO_{out}}}{F_{CH_{4_{out}}}} \times 100 \qquad (4.4)$$

Where F_i is the normalised volumetric flow rate of species *i*.

4.2. Preliminary investigations of CO preferential oxidation on Au, CO selective methanation on Ni, and CO selective methanation on Ru

4.2.1. CO preferential oxidation in the Au/Al_2O_3-washcoated microchannel reactor

CO PROX experiments were carried out in a microchannel reactor washcoated with the 1.15 wt.% Au/Al_2O_3 commercial catalyst. The feed mixture to the reactor consisted of 68.6 vol.% H_2, 1.4 vol.% CO, 10 vol.% CO_2, 2 vol.% O_2 and 18 vol.% N_2. In order to maximise the residence time, low feed flow rates of 50 and 100 $NmL.min^{-1}$ (corresponding to space velocities of 32.6 and 65.2 $NL.g_{cat}^{-1}.h^{-1}$) were used for these oxidation experiments. No CO conversion was observed at temperatures between 80 and 200^{o}C. From the literature, these temperatures are within the suitable range for CO PROX on Au-based catalysts.

In the absence of CO_2 in the feed gas, and the balance made up of additional N_2, CO conversions reached only 8–10% between 150 and 200°C, which suggested that some inhibition effect by CO_2 on the catalyst surface took place, as suggested by Uriz *et al*. (2013:287). This alone cannot fully explain the low rate of CO conversion. Other possibilities could include the aging of the catalyst or the sintering of the Au particles which could have occurred as the reactor was previously used for formic acid decomposition at relatively high temperatures (up to 350°C) (Ndlovu *et al*., 2018:485–497). Lastly, other mechanisms of catalyst deactivation, such as the possibility of carbonate species formation on catalytically active sites, could be the reason which the loss in

activity is attributed to. It was difficult to establish the true cause of the poor reactor performance, and ultimately it was decided to study the other catalytic microchannel reactors instead.

4.2.2. CO selective methanation in the Ni-Pt/Al_2O_3-washcoated microchannel reactor

CO SELMET experiments were carried out in the microchannel reactor washcoated with the 4.7 wt.% Ni-Pt/Al_2O_3 catalyst. The feed mixture consisted of 68.6 vol.% H_2, 1.4 vol.% CO, 10 vol.% CO_2 and 20 vol.% N_2. The feed flow rate was kept relatively low at 50 and 100 NmL.min^{-1} (space velocities of 32.6 and 65.2 NL.g_{cat}^{-1}.h^{-1}) in order to maximise the residence time. The reactor temperature was varied between 150 and 600°C, a range which covers typical temperatures for CO methanation on Ni-based catalyst reported in the literature.

Experimental results for CO conversion via methanation are illustrated in Fig. 4.1 for the two space velocities investigated. Both the reaction temperature and the space velocity influenced the CO conversion, which however, remained lower than 40% for the range of operating conditions investigated. At the lowest space velocity (32.6 NL.g_{cat}^{-1}.h^{-1}) and 400°C, the maximum CO conversion was attained of 39.0%. The CO conversion reached only 20.0% at 350°C when the space velocity was doubled. One of the probable reasons for the unsatisfactory reactor performance is the low Ni loading of the catalyst. Typical Ni loadings for efficient CO SELMET catalysts range between 10 and 40 wt.%. Gao *et al*. (2016:5489) reported that, at a constant reaction temperature, the CO conversion improves with increasing Ni loading of the catalyst.

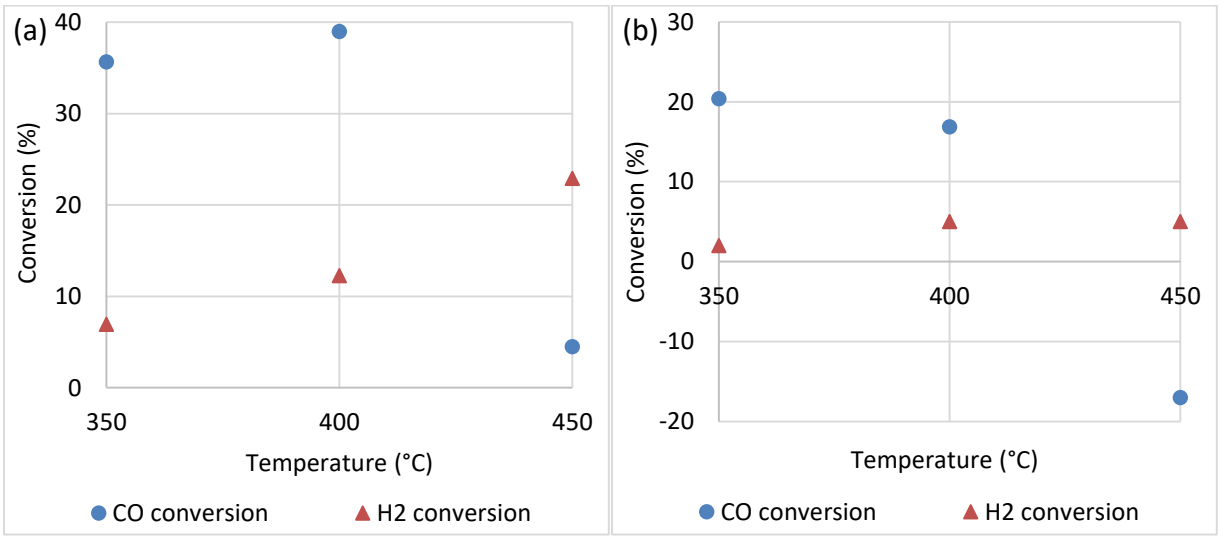

Fig. 4.1. CO and H_2 conversions in the 4.7 wt.% Ni-Pt/Al_2O_3-coated microchannel reactor at space velocities of (a) 32.6 and (b) 65.2 NL.g_{cat}^{-1}.h^{-1}.

Due to the low CO conversions obtained at 350 and 400°C, the reaction temperature was increased in anticipation that faster kinetics would improve the reactor performance. On the contrary, at 450°C, the CO conversions decreased to 4.5 and -17.0% at the 32.6 and 65.2 $NL.g_{cat}^{-1}.h^{-1}$ space velocities, respectively. An explanation for this phenomenon is the endothermic RWGS reaction which converts CO_2 into CO at higher temperatures (Chin *et al*., 2014:134). The negative conversion (-17%) obtained at the high space velocity indicated that more CO was formed at 450°C, compared to the rate at which CO was consumed via methanation.

In some studies, the performance of Ni catalysts is improved by the addition of promoters such as Ru, V_2O_3, MgO or CaO (Gao *et al.*, 2016:5490; Li *et al.*, 2014:43; Men *et al*., 2001:83). In this investigation, it was difficult to establish the effect of the 0.1 wt.% Pt as promoter to the Ni catalyst used. Ultimately, CO SELMET on Ni appeared to yield sub-standard results. Consequently, the CO methanation reaction was studied in the third catalytic reactor containing the Ru-based catalyst.

4.2.3. CO selective methanation in the Ru-Cs/Al_2O_3-washcoated microchannel reactor

CO SELMET experiments were performed in a microchannel reactor coated with a 8.5 wt.% Ru-Cs/Al_2O_3 catalyst. The feed mixture consisted in 68.53 vol.% H_2, 1.47 vol.% CO, 10 vol.% CO_2 and 20 vol.% N_2. Feed flow rates of 50 and 100 $NmL.min^{-1}$ (space velocities of 32.6 and 65.2 $NL.g_{cat}^{-1}.h^{-1}$) were used in experiments which were conducted at reactor temperatures of 280–400°C.

In general, when flow rates were increased to the microchannel reactor, slightly higher temperatures were required to convert the same amount of CO to CH_4. To illustrate this, at a temperature of 280°C and a space velocity of 32.6 $NL.g_{cat}^{-1}.h^{-1}$, 0.5 vol.% CH_4 was detected in the outlet gas of the microchannel reactor. At higher space velocity (65.2 $NL.g_{cat}^{-1}.h^{-1}$), the same performance was achieved at 300°C. It was observed that the conversion of CO increased with higher reaction temperatures. At 32.6 $NL.g_{cat}^{-1}.h^{-1}$, average CO conversions increased from less than 10% at 300°C to reaching near-equilibrium values (>99%) at 380°C and higher. This suggests that kinetic limitations are a possible cause of low conversions below 380°C. However, the competing RWGS reaction could also be a factor that kept CO conversions below equilibrium in this temperature range.

Unfortunately, as the CO conversion increased with higher reaction temperature, so did that of CO_2. The selectivity towards CO methanation was below 20% for all the reaction temperatures and space velocities studied. At 32.6 $NL.g_{cat}^{-1}.h^{-1}$, H_2 consumption rose from ca. 9% to more than 60% between 300°C and 400°C. This high consumption rate is due the large H/C stoichiometric ratios of the methanation reactions–especially that of the CO_2 reaction pathway, considering CO_2's high initial feed concentration (10 vol.%). Excessive H_2 consumption rate is undesirable as the ultimate fuel that is intended for fuel cells is depleted in the CO clean-up stage.

An apparent loss of catalytic performance with time-on-stream was observed with the Ru-based catalyst for CO methanation. Figure 4.2 illustrates the decrease in performance within 2 h of operation at a space velocity of 65.2 $NL.g_{cat}^{-1}.h^{-1}$ and at temperatures between 360 and 400°C. In this temperature range, the decrease in CO conversion was more severe at 360°C, as CO conversions became negative (more CO formation by RWGS). The gradual loss in activity was possibly the result of carbon deposition on the surface of the catalyst. Catalyst reduction steps using a pure flow of H_2 (50 $NmL.min^{-1}$) were done at 400°C between experiments to regain the activity of the Ru catalyst. The detection of CH_4 during the reduction processes confirmed the hypothesis of carbon deposition.

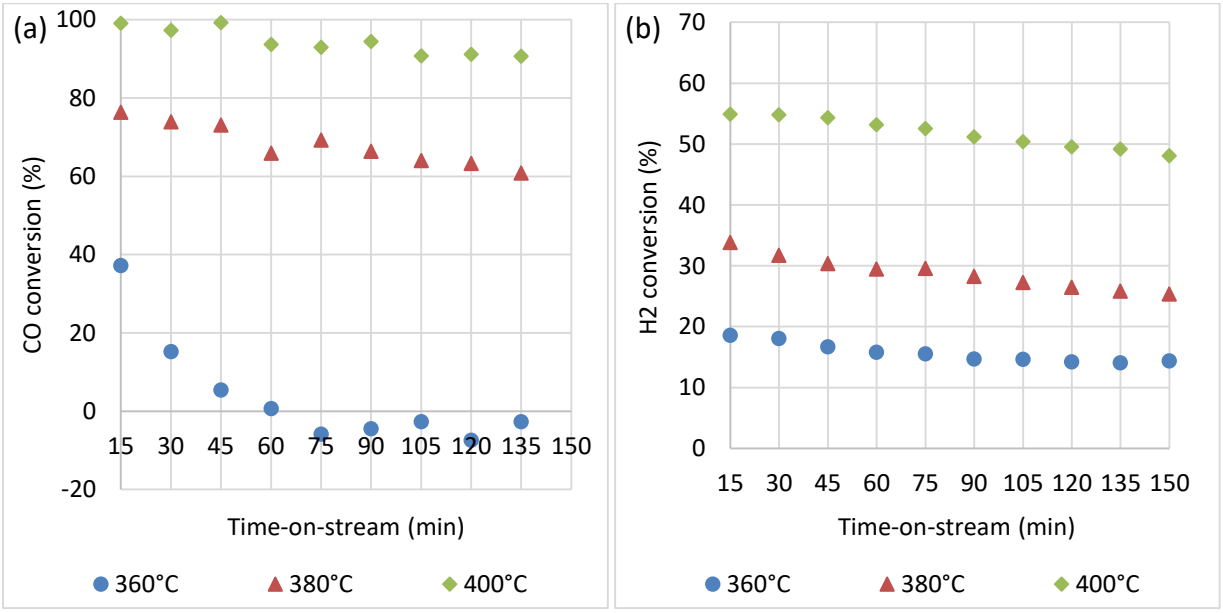

Fig. 4.2. Decrease in (a) CO conversion and (b) H_2 conversion, plotted against the reaction time-on-stream at a space velocity of 65.2 $NL.g_{cat}^{-1}.h^{-1}$.

4.3. CO preferential oxidation in the Ru-Cs/Al_2O_3-washcoated microchannel reactor

The microchannel reactor coated with the 8.5 wt.% Ru-Cs/Al_2O_3 catalyst was used for the PROX of CO. The feed gas mixture consisted in 68.6 vol.% H_2, 1.4 vol.% CO, 10 vol.% CO_2, 2 vol.% O_2 and 18 vol.% N_2. Feed flow rates of 50 to 200 NmL.min^{-1} (space velocities of 32.6 to 130.4 NL.g_{cat}^{-1}.h^{-1}) were used to evaluate the effects of residence time within the reactor. The reaction temperature was varied in a range of 80–200°C, since CO PROX does not require temperatures as high as those required for the methanation of CO. In addition, low temperature oxidation avoids the presence of the methanation reactions, which would consume significant amounts of H_2, and ultimately lower the energy content of the product gas stream.

4.3.1. Effects of reaction temperature and gas hourly space velocity on the performance of the microchannel reactor

Six temperatures were chosen in the range of 100–200°C (in intervals of 20°C) at flow rates of 50–200 NmL.min^{-1} (in intervals of 50 NmL.min^{-1}) which corresponded to space velocities of 32.6–130.4 NL.g_{cat}^{-1}.h^{-1}. These reaction parameters were chosen in a broad range to fully evaluate the microchannel reactor's performance based on these parameters. For the space velocity of 32.6 NL.g_{cat}^{-1}.h^{-1}, an additional experimental data point was added at 80°C. The general trend of CO conversion as a function of reaction temperature (Fig. 4.3) is similar to several literature observations for PROX processes (Rosso *et al.*, 2004:478; Chen *et al.*, 2013:276; Kim & Park, 2010:48), even though the exact conversion values differ with reaction conditions including temperature, space velocity and feed composition.

The CO conversions were observed to be strongly dependent on the reaction temperature. At a space velocity of 32.6 NL.g_{cat}^{-1}.h^{-1} and a temperature of 80°C, a CO conversion of 38.5% was observed. This data point was added to illustrate kinetic limitations for this single flow rate which did not show obvious kinetic limitations at 100°C. At the three higher space velocities, CO conversions did not exceed 65% at 100°C. At these lowest temperatures investigated, sub-standard CO conversions can be attributed to kinetic limitations. In the intermediate temperature range studied (120–160°C), CO conversions (>98%) were close to the equilibrium values calculated for all the space velocities investigated. At higher temperatures (180 and 200°C), a decrease in CO

conversion was observed for the four space velocities, which is attributed to the occurrence of the RWGS reaction. The relatively high amounts of H_2 and CO_2 in the feed gas, and the higher temperature range (180 and 200°C), caused the RWGS reaction to shift towards the formation of some CO and H_2O. This decrease in CO conversion at higher temperatures is not observed when the CO oxidation is carried out in the absence of H_2 (Grisel & Nieuwenhuys, 2001:51).

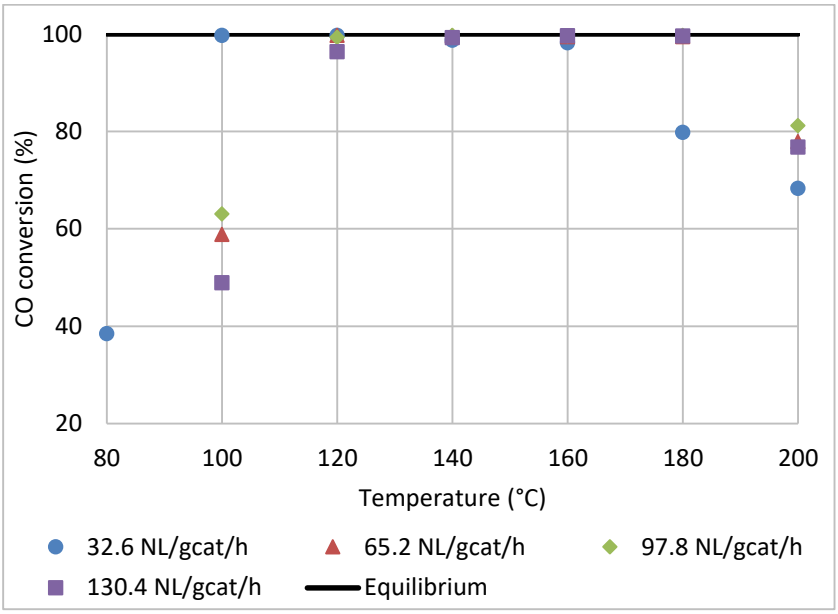

Fig. 4.3. Effects of reaction temperature and space velocity on the CO conversion by PROX on Ru-Cs/Al_2O_3. Feed composition: 68.6 vol.% H_2, 1.4 vol.% CO, 10 vol.% CO_2, 2 vol.% O_2 and 18 vol.% N_2. (This set of data is also presented in table form in Fig. F.1, Appendix F)

Figure 4.3 also illustrates the effect of the residence time on the CO conversion at different temperatures. At 100°C, 99.7% CO conversion was observed at 32.6 $NL.g_{cat}^{-1}.h^{-1}$, whereas at higher space velocities (65.2–130.4 $NL.g_{cat}^{-1}.h^{-1}$) the CO conversion was comprised, and measured in a range of 48–64%. This suggests that high residence times (low space velocity) are needed in order to maximise the contact time between the reactants in the gas mixture and the catalytically active sites. It was the nearly complete CO conversion observed at 100°C and 32.6 $NL.g_{cat}^{-1}.h^{-1}$ that required an experiment at lower temperature (80°C) to determine if kinetic limitations also exist for this space velocity. The reactor performance at higher space velocity (65.2–130.4 $NL.g_{cat}^{-1}.h^{-1}$) was unsatisfactory at 100°C, and therefore not evaluated at 80°C, as it is understood that

much lower CO conversions would be obtained compared to the 38.5% CO conversion at 32.6 $NL.g_{cat}^{-1}.h^{-1}$.

It is interesting to note the decrease in CO conversion by increasing the reaction temperature from 160 to 180°C at the 32.6 $NL.g_{cat}^{-1}.h^{-1}$ space velocity. The CO conversion decreased from 98.2% to 79.8% with the increase in this reaction temperature mentioned. The high residence time for this flow condition has allowed the undesirable RWGS reaction to considerably counteract the CO oxidation reaction. For the higher space velocities (65.2–130.4 $NL.g_{cat}^{-1}.h^{-1}$), the decrease in gas contact time with the catalyst was not sufficient for the slower RWGS reaction to have a significant effect on the more rapid CO oxidation reaction. This effect of the RWGS reaction was more pronounced at the 200°C reaction temperature, at which the CO conversion was measured for all four flow rates in a range of 68.3–81.1%. At that temperature, the increasing effect of the endothermic RWGS reaction resulted in a noticeable increase in CO product concentrations which lied between 2698.2–6690 ppm (>>100ppm). Consequently, 200°C acted as the high temperature boundary for this experimental investigation. In order to illustrate the simultaneous effects of the space velocity and the temperature on the CO conversion, 3D plots in were added in Appendix E (Fig. E.1).

PEMFC using more durable Pt-Ru anodes can tolerate maximum CO impurity in the H_2 fuel of 100 ppm (Mohaideen *et al.*, 2014:8). The microchannel reactor was able to achieve CO product concentrations lower than 100 ppm at all the space velocities investigated. The lowest CO concentrations (<50 ppm) were observed at individual reaction temperatures of 100, 120, 140 and 160°C for the four space velocities of 32.6, 65.2, 97.8 and 130.4 $NL.g_{cat}^{-1}.h^{-1}$, respectively (Fig. 4.4). This again suggested that higher reaction temperature was necessary to achieve similar conversions when the space velocity was increased. Suitable temperature ranges for acceptable performance varied for the different space velocities. CO product concentrations lower than 100 ppm were obtained for a 60°C temperature range from 120 to 180°C for the space velocities of 65.2 and 97.8 $NL.g_{cat}^{-1}.h^{-1}$. At the lowest and highest space velocity conditions, the temperature ranges were respectively only 20 and 40°C large.

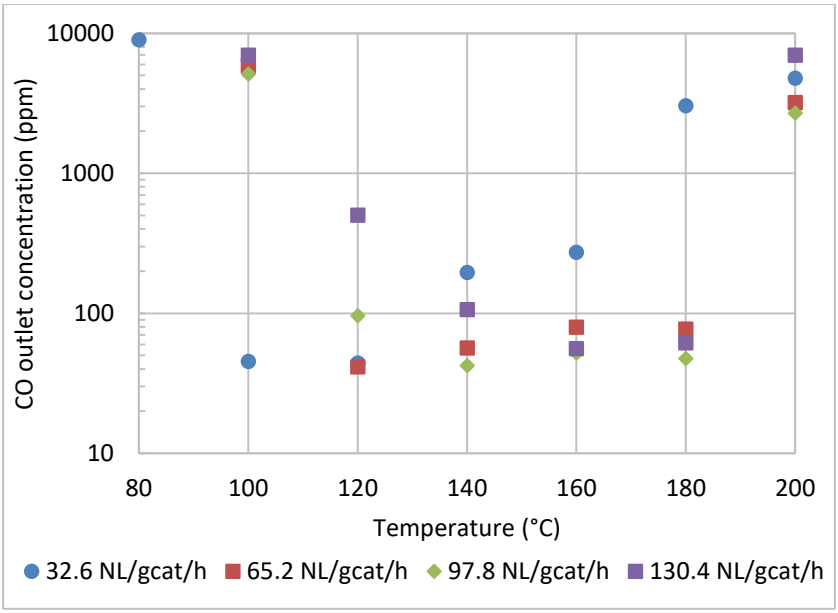

Fig. 4.4. Effects of reaction temperature and space velocity on the CO product concentration by PROX on Ru-Cs/Al_2O_3. Feed composition: 68.6 vol.% H_2, 1.4 vol.% CO, 10 vol.% CO_2, 2 vol.% O_2 and 18 vol.% N_2. (This set of data is also presented in table form in Fig. F.2, Appendix F)

The microchannel reactor performance assessment deduced from Figs. 4.3 and 4.4 suggest that space velocities of 65.2 and 97.8 $NL.g_{cat}^{-1}.h^{-1}$ and reaction temperatures between 120 and 180°C are suitable. However, the conversion of H_2 must be taken into account, and subsequently minimised. The relatively high amount of H_2 (68.6 vol.%) in the feed gas renders its oxidation inevitable. Figure 4.5 shows that for all the reaction temperatures and flow conditions studied, the maximum H_2 consumption did not exceed 7% (Fig. 4.5a). This meant that the selectivities towards CO oxidation were between 20 and 50%. It was observed that the H_2 conversion decreased with an increase in space velocity. This once again implies that shorter residence time could limit H_2 consumption, and preserve the energy content of the product gas. Due to faster kinetics, H_2 oxidation increased with reaction temperature. In the literature, CO selectivities varied between 20 and 80%, depending on the catalyst and reaction conditions (Arzamendi *et al.*, 2011:590; Rosso *et al.*, 2004:478; Han *et al.*, 2004:125; Kim *et al.*, 2010:49), but can be as high as 100% if low reaction temperature is used (i.e. 20°C), as in the case of several Au-catalysed PROX processes (Li *et al.*, 2013:2).

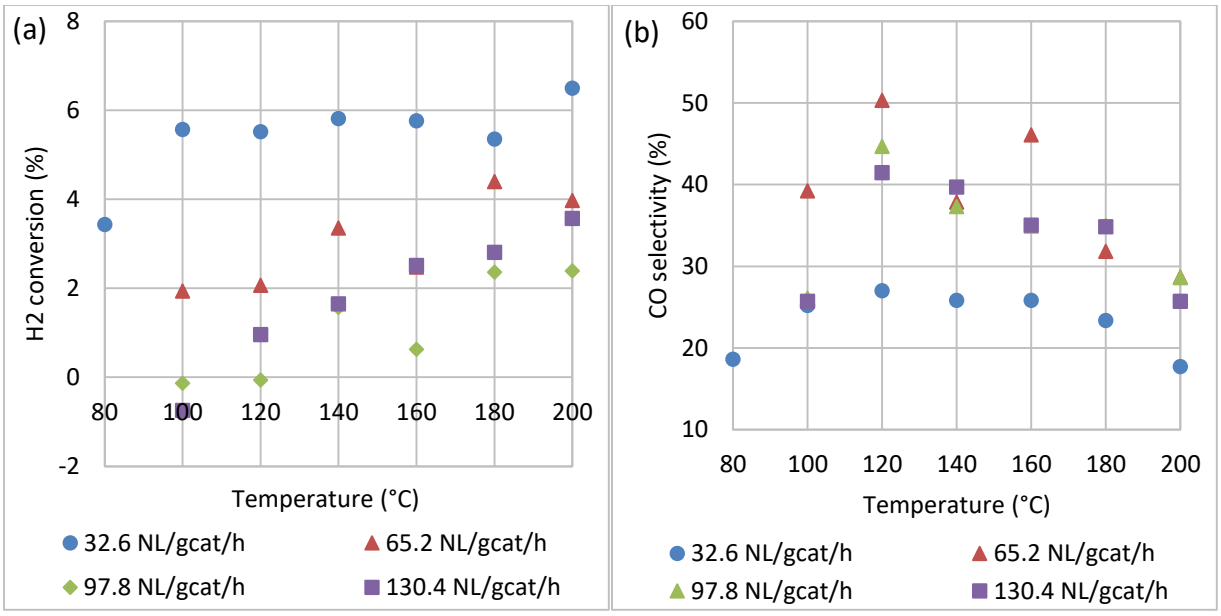

Fig. 4.5. Effects of reaction temperature and space velocity on the (a) H_2 conversion and (b) selectivity towards CO oxidation. Feed composition: 68.6 vol.% H_2, 1.4 vol.% CO, 10 vol.% CO_2, 2 vol.% O_2 and 18 vol.% N_2. (These sets of data are also presented in table form in Figs. F.3 and F.4, Appendix F)

At all the space velocities, the CO selectivity was low (20–40%) in the low temperature region (80 and 100°C). This low selectivity can be attributed to slow kinetics for the CO oxidation reaction, while the occurrence of H_2 oxidation was already observed. As the reaction temperature increased to 120°C, CO conversions were near maximum and resulted in higher CO selectivities (as high as 50.3% for 65.2 $NL.g_{cat}^{-1}.h^{-1}$), as the rate of H_2 oxidation was still relatively slow. From temperatures of 140°C and upwards, the CO selectivities for the four space velocities decreased, firstly due to increased H_2 oxidation, and secondly as a result of CO formation by the RWGS reaction at temperatures above 180°C.

Varying the space velocity affected the extent of H_2 consumption in similar ways as previously described for the CO oxidation reaction at low temperatures. Low space velocity increased both H_2 and CO oxidation, as gas-catalyst contact time was extended. The highest H_2 conversions (3.4–6.5%) and lowest selectivities (<28%) were observed for the low space velocity of 32.6 $NL.g_{cat}^{-1}.h^{-1}$. The Ru-Cs/Al_2O_3 catalyst is well known for exhibiting high activity for the methanation reaction too. However, in the low temperature range studied, no CH_4 was detected in the product

gas. The CO and CO_2 methanation reactions generally have higher activation energies than the oxidation reactions on this particular Ru-Cs/Al_2O_3 catalyst, and would therefore require higher reaction temperatures (>200°C) to be initiated.

4.3.2. Effect of the O_2/CO ratio on the performance of the microchannel reactor

The experimental results reported on the effects of reaction temperature and space velocity (Section 4.3.1) were performed at an O_2/CO molar ratio of 1.4, compared to the stoichiometric amount required for complete CO conversion (O_2/CO ratio = 0.5). In practice, since the H_2 oxidation reaction is unavoidable in CO PROX processes, O_2/CO ratios greater than stoichiometric are required for complete CO abatement (Han *et al*., 2002:395). Snytnikov *et al*. (2003:152) suggested that CO inlet concentrations between 0.6 and 1 vol.% require O_2/CO ratios between 1 and 1.5 in order to reduce the CO concentration to less than 10 ppm. Han *et al*. (2004: 125) used a ratio of 1.3 to convert more than 99% of the inlet CO (0.2 vol.% of the feed) in a temperature range of 100–120°C.

The best operating conditions identified in Section 4.3.1 (space velocities: 65.2 and 97.8 $NL.g_{cat}^{-1}.h^{-1}$; reaction temperatures: 120–180°C) were selected in order to study the effect of the O_2/CO ratio. In this section, the feed mixture contained O_2 and CO at O_2/CO ratios of 0.7 and 2.8, in addition to the 1.4 molar ratio used during the base case experiments. Table 4.1 summarises the feed gas compositions at different O_2/CO ratios.

Table 4.1. Feed gas compositions for CO PROX, corresponding to different O_2/CO ratios investigated

O_2/CO ratio	Feed composition
0.7	68.6 vol.% H_2, 1.4 vol.% CO, 10 vol.% CO_2, 1.0 vol.% O_2 and 19 vol.% N_2.
1.4	68.6 vol.% H_2, 1.4 vol.% CO, 10 vol.% CO_2, 2.0 vol.% O_2 and 18 vol.% N_2.
2.8	68.6 vol.% H_2, 1.4 vol.% CO, 10 vol.% CO_2, 4.1 vol.% O_2 and 15.9 vol.% N_2.

Figure 4.6 shows the performance of CO PROX at O_2/CO molar ratios of 0.7 and 1.4, at the two selected space velocities (65.2 and 97.8 $NL.g_{cat}^{-1}.h^{-1}$). In practice, a low O_2/CO ratio which provides good CO oxidation performance will reduce the air requirements of the reactor for

complete CO conversion. The different temperature ranges chosen were the ones at which the CO product concentrations were previously found to be the lowest at each of the flow rates. The CO conversion at the O_2/CO ratio of 0.7 was at least 40% lower than the conversions obtained at O_2/CO ratio of 1.4. CO conversions showed a slight decrease from 140°C which is probably due to the competing H_2 oxidation as shown by the small decrease in selectivity observed at the same temperatures. Selectivities obtained at the O_2/CO ratio of 0.7 showed that only 30 to 40% of the O_2 fed is actually used in the conversion of CO.

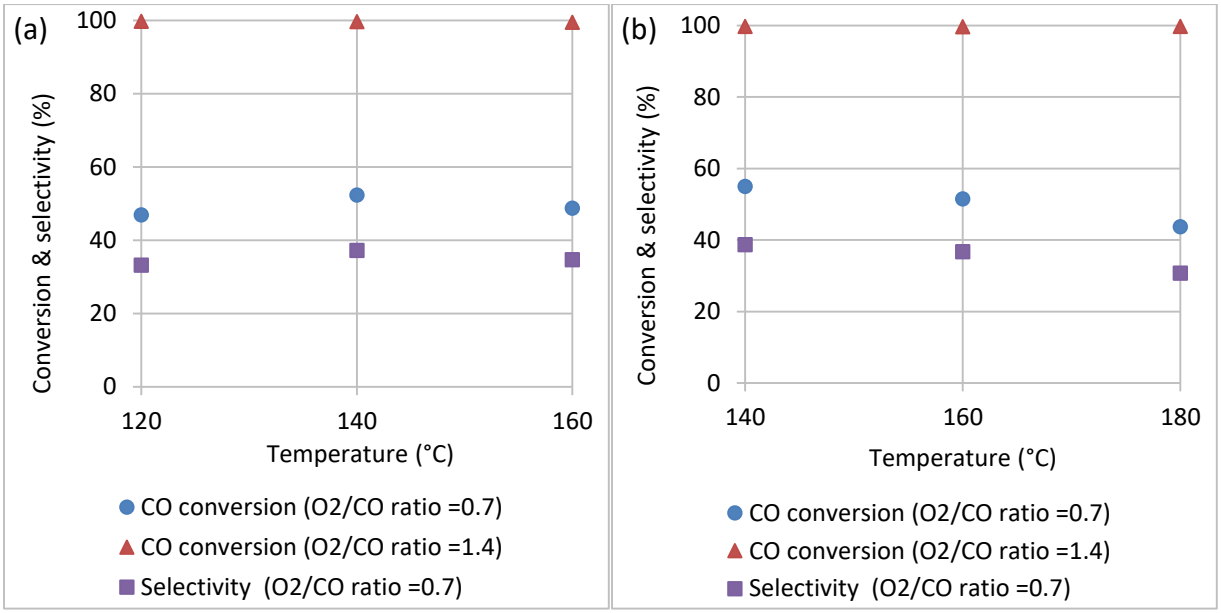

Fig. 4.6. Effect of the O_2/CO ratio on the CO conversion at space velocities: (a) 65.2 NL.g_{cat}^{-1}.h^{-1} and (b) 97.8 NL.g_{cat}^{-1}.h^{-1}.

These results show that, at the O_2/CO ratio of 0.7, there is not sufficient O_2 for complete CO conversion in an H_2-rich gas mixture. The reactor performances at O_2/CO ratios of 2.8 and 1.4 were compared at a space velocity of 65.2 NL.g_{cat}^{-1}.h^{-1}. Average selectivities recorded at the O_2/CO ratio of 2.8 were found to be 15–22% (compared to 30–40% at the O_2/CO ratio of 1.4). O_2 converted the both CO and larger amounts of H_2 in the feed gas. In addition, lower CO conversions decreasing with time-on-stream were observed at the O_2/CO ratio of 2.8 (Fig. 4.7). The excess O_2 at this O_2/CO ratio probably contributed to the deactivation of the Ru catalyst. This suggests the oxidation of metallic Ru to possibly RuO and RuO_2. When the loss in activity of the catalyst due to oxidation occurred in the extreme case illustrated in Fig. 4.7, initial catalytic performance could be recovered with a H_2 flow rate of 50 NmL.min^{-1} at a reduction temperature of 400°C for an hour.

Han *et al*. (2002:395) explained that at high O_2/CO ratios (strong oxidizing conditions), CO conversion decreased due to the lower CO coverage on the surface of the Ru-based catalyst, and that the oxidation of Ru to RuO_2 occurred. The layer of RuO_2 was inactive for the CO oxidation reaction.

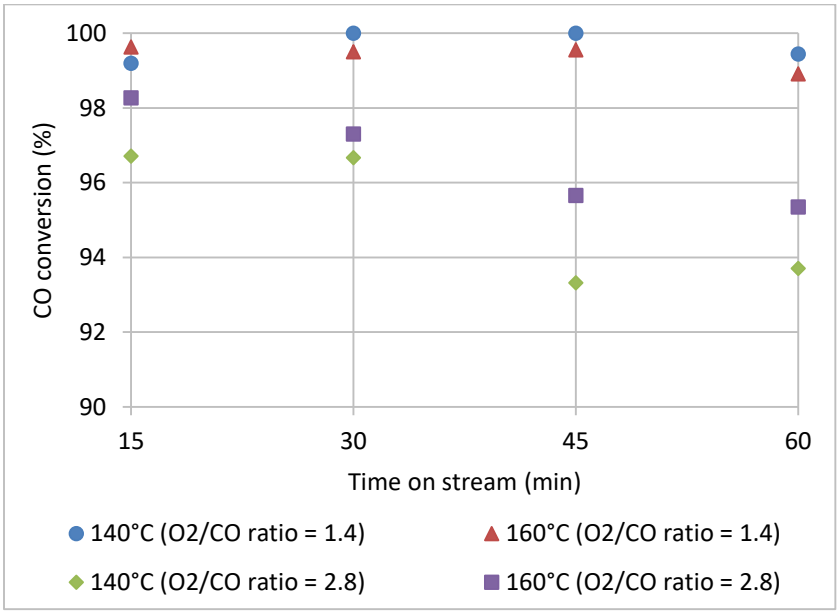

Fig. 4.7. Comparison between CO conversions at O_2/CO ratios of 1.4 and 2.8. Space velocity of 65.2 NL.g_{cat}^{-1}.h^{-1} and reaction temperatures of 140 and 160°C.

4.3.3. Reproducibility of results

In order to ensure accuracy of the experimental results, some of the data points were repeated at identical operating conditions. The four experiments chosen (Table 4.2) were those which yielded high reactor performance in terms of CO conversion.

Table 4.2. Experimental conditions for the reproducibility of results.

Experiment No	Space velocity (NL.g_{cat}^{-1}.h^{-1})	Reaction temperature (°C)	O_2/CO ratio
1	32.6	100	1.4
2	32.6	120	1.4
3	65.2	120	1.4
4	97.8	140	1.4

Up to the point where experimental data was repeated, the microchannel reactor with Ru-based catalyst endured about 150 hours of experiments, conducted in daily start/stop cycles. Ensuring reproducibility after these experiments will be an indication of the catalyst longevity. A major catalyst degradation pathway is catalyst sintering (particle agglomeration) after extended time-on-stream and elevated temperature experiments, which will be investigated with the reproducibility experiments. Before the repeated experiments were performed, the catalyst was reduced using a pure H_2 flow rate of 50 Nml/min (32.6 $NL.g_{cat}^{-1}.h^{-1}$) at 400°C for an hour to avoid the possibility of Ru oxides on the catalyst surface, due to the number of earlier experiments performed. During the experimental repeats (Fig. 4.8), the reactor still exhibited high performance, with the outlet CO concentrations being below 60 ppm for the four cases investigated (Table 4.2).

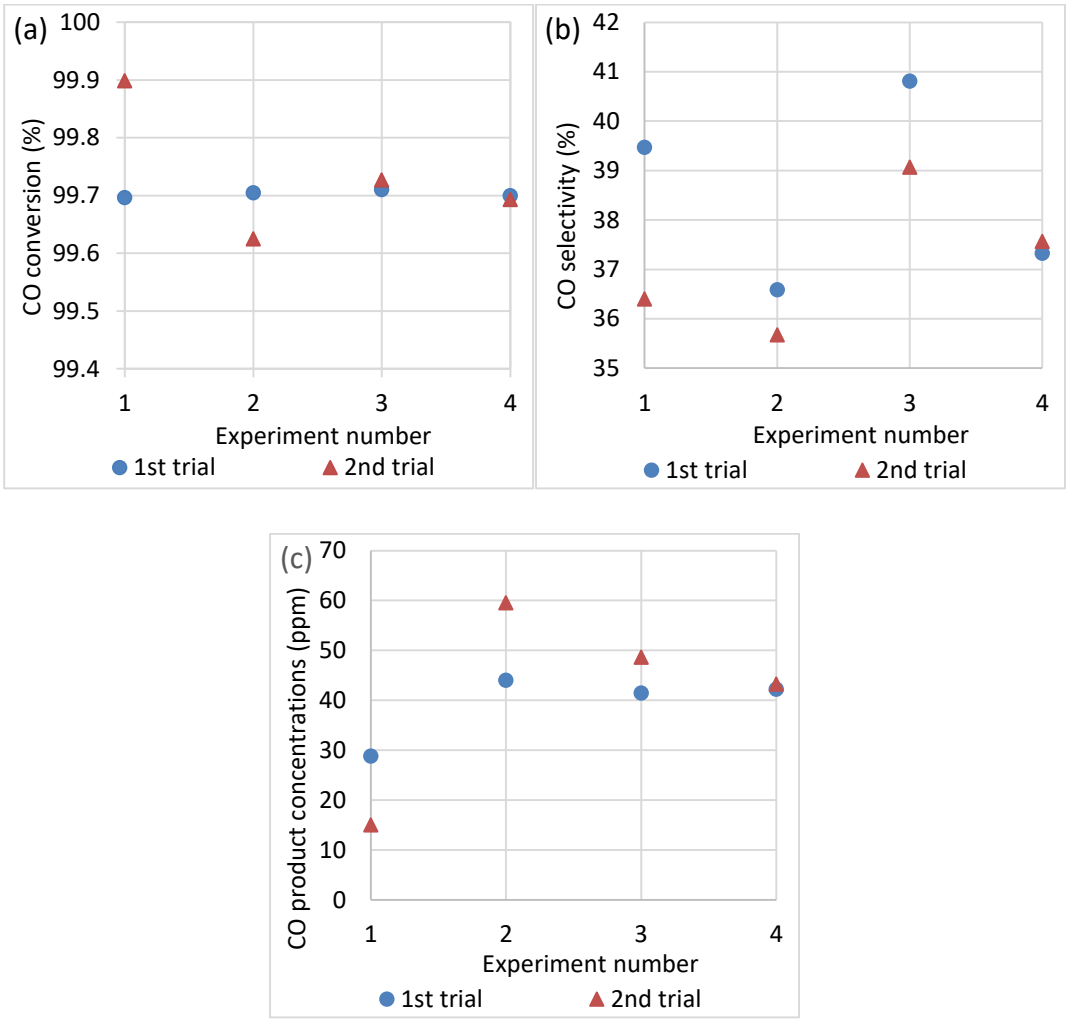

Fig. 4.8. Results from the reproducibility tests: (a) CO conversions; (b) CO product concentrations and (c) CO selectivities.

Figure 4.8a shows that the repeated data for CO conversion was closely related to the original values for each of the four repeated experiment conditions. The largest difference in CO conversion (ca. 0.2%, experiment 1) corresponded to product concentrations of 15 to 29 ppm CO (Fig. 4.8c) and a difference in selectivities of about 3%. At these low concentrations, the differences could partially be influenced by uncertainties in the measurement of very low concentrations using the gas chromatograph. Although some variations were obtained in the repeated values for CO conversion, selectivity and product concentration, consider the amount of CO that entered the reactor; the microchannel reactor was able to reduce CO levels from 14 000 ppm to a range of 15–60 ppm. The scale differences in these values and the small outlet variations are indicative of the catalyst having kept its activity (Ru particle dispersion) during the course of the CO PROX experiments. The deactivation of Ru-Cs/Al_2O_3 can occur for different reasons, including thermal sintering and oxidation. The result of the reproducibility test showed that the catalyst was able to maintain satisfactory performance (CO product concentrations < 100 ppm) after more than 150 hours of operation, provided suitable H_2 reduction is used after experiments containing high O_2/CO ratios, in order to avoid irreversible alteration of the metallic state of the Ru catalyst.

4.4. Recommended operating conditions of the microchannel reactor

The experimental performance evaluation of the Ru-based microchannel reactor for CO PROX show that this process is a viable option for CO abatement to concentration levels below 100 ppm, starting with a H_2-rich feed gas containing 1.4 vol.% CO. The microchannel reactor was coated with a 8.5 wt.% Ru-Cs/Al_2O_3 catalyst and was evaluated in a temperature range of 80–200°C. Figure 4.4 shows that low CO product concentrations (<100 ppm) were obtained at all space velocities investigated (32.6–130.4 $NL.g_{cat}^{-1}.h^{-1}$) at different temperatures ranging from 100 to 180°C. These temperatures are typically lower than that of WGS reactors, which means that any feed pre-heating is not necessary before CO can be removed. In addition, these temperatures are close to the operating temperature of PEMFC, which will facilitate the integration of the PROX reactor to the fuel processing unit.

Of the three O_2/CO ratios studied, satisfactory CO conversion (>99.6%) was only achieved at the ratio of 1.4. The ratio of 0.7 provided too little O_2 for significant CO abatement (to levels below 50 ppm), as the competing H_2 oxidation reaction also consumed small amounts of O_2. Meanwhile,

at a high O_2/CO ratio of 2.8, the excess O_2 contributed to the oxidation of the catalytically active Ru metal, and decreased CO oxidation activity was observed with time-on-stream.

At flow rates of 100 and 150 NmL.min^{-1} (65.2 and 97.8 NL.g_{cat}^{-1}.h^{-1}), CO product concentrations lower than 100 ppm were achieved in a large temperature range of 120–180°C. The flow rate of 150 NmL.min^{-1} (97.8 NL.g_{cat}^{-1}.h^{-1}) presents the advantage of higher throughput for the same reactor size. To maximise CO abatement, it is recommended that CO conversion by PROX is carried out at space velocities between 65.2 and 97.8 NL.g_{cat}^{-1}.h^{-1}. The operating temperature is recommended between 120 and 140°C at an O_2/CO ratio of 1.4. CO product concentrations as low as 41–42 ppm could be achieved at these conditions. For increased space velocities, higher reaction temperatures will be required for achieving the same level of CO conversions. This can be seen in Fig. 4.4 where a CO product concentration of 55.9 ppm was achieved at 160°C for the 130.4 NL.g_{cat}^{-1}.h^{-1} space velocity.

Typically, small-scale fuel processors can operate near-isothermally, so in this case it would be easy to control the temperature in the temperature range of 120–140°C. In addition, the lower temperature range of 120–140°C will ensure catalyst longevity and durability, as the oxidation of the Ru catalyst is insignificant, while the effects of the H_2 oxidation is also kept minimal. In this way, it is possible to selectively convert nearly all CO contained in a H_2-rich stream from a WGS reactor effectively to provide H_2 for fuel cell applications.

CHAPTER 5. CFD MODEL DEVELOPMENT, RESULTS AND DISCUSSION

This chapter is devoted to the development and experimental validation of a 3D CFD model of the Ru-Cs/Al_2O_3-coated microchannel reactor for the CO PROX process. CO removal using the preferential oxidation process was found to be the most effective and with much higher selectivity, compared to CO selective methanation. This chapter presents the kinetic parameters used in the simulation as well as a model validation using the experimental results obtained in the previous chapter. The CFD model geometry, assumptions, equations and boundary conditions are summarised in Section 5.1. Section 5.2 provides a description of the approach followed to validate the model to the experimental data. Section 5.3 provides the results of model validation to the experimental data, and the goodness of fit estimation. Sections 5.4 gives more clarity and discusses the transport distributions and kinetic properties within the dynamic space of the modelled microchannel, including: velocity, reaction rate, species concentration and pressure drop effects.

5.1. CFD model description

During the experimental evaluation of the microchannel reactors, the CO preferential oxidation process was found to be best suited for the removal of CO from a H_2-rich gas stream. In this chapter, the process was simulated using a CFD modelling technique to better understand the transport phenomena taking place within the microchannel reactor, and to estimate the reactor performance using a model-based technique with suitable reaction kinetics. Understanding the kinetics of the process, as well as the transport phenomena within the unknown space of microchannels can be especially useful to predict the performance of the microchannel reactor during the removal of CO from H_2-rich gas streams. A CFD model was developed in COMSOL Multiphysics® V4.4 software. In this work, only steady-state modelling was attempted in order to validate experimental data from the microchannel reactor. Below are important aspects of the model geometry, assumptions made, and governing equations used within certain boundary conditions of the model.

5.1.1. Process description and catalyst

The CO oxidation process which was simulated in a microchannel reactor involved a volumetric feed gas mixture of 68.6% H_2, 1.4% CO, 10% CO_2, 2% O_2 and N_2 as balance. The gas was introduced into the microchannel reactor at four different flow rates (32.6 to 130.4 $NL.g_{cat}^{-1}.h^{-1}$) and 6 reaction temperatures (100 to 200°C). The geometry of the microchannel reactor consisted of two computational domains: a free-fluid region and a porous catalyst layer. Upon entering the microchannel, the gas was assumed to first access the free-fluid region before transferring to the porous catalyst through rapid diffusion.

The catalyst section consisted of a 40 µm-thick Ru-Cs/Al_2O_3 layer coated on the microchannel walls, and was considered both a sink for the reactants and a source of products. The physical characteristics of the catalyst were estimated from the properties of Ru-Cs/Al_2O_3. They included the density, thermal conductivity and heat capacity. The total catalyst mass was 92 mg, and its porosity was assumed to be 0.40. Chemical reaction rate expressions, which will be listed in the following sections, were used to describe the activity and selectivity of CO oxidation, H_2 oxidation and reversible WGS.

5.1.2. Model geometry

The CFD model geometry of the microchannel reactor was originally designed by Chiuta *et al.* (2014:11393). It represents a single wall-coated microchannel, truncated along its central longitudinal plane as a plane of symmetry. The geometry length, width and height were 50 mm, 225 µm and 150 µm, respectively. A uniform catalyst thickness of 40 µm was incorporated, and also illustrated in Fig. 5.1 as a computational domain. The delimitation of the free-fluid and the porous catalyst sections is shown in Fig. 5.1a.

Furthermore, the model geometry was discretized using a relatively fine mesh, consisting of a total of 75 900 prismatic elements (Fig. 5.1b). The mesh was manually generated in such a way as to assign the finest elements towards the interface between the free-fluid and the catalyst sections, as well as at the catalyst outer wall. This was done in order to improve the accuracy of boundary condition computations. Generally, the catalyst layer contained finer elements to accurately calculate the fast reaction rates within the catalyst (gas species consumption/formation), while the free-fluid region contained slightly coarser mesh elements as it only supports slower convective

and diffusive mass transfer (to minimise computational time). Finally, a distribution function was used to slice the microchannel at its inlet into fine slices, perpendicular to the flow direction. This was done to improve calculation accuracy at the inlet of the microchannel, while towards the outlet of the microchannel, coarser mesh slices were used.

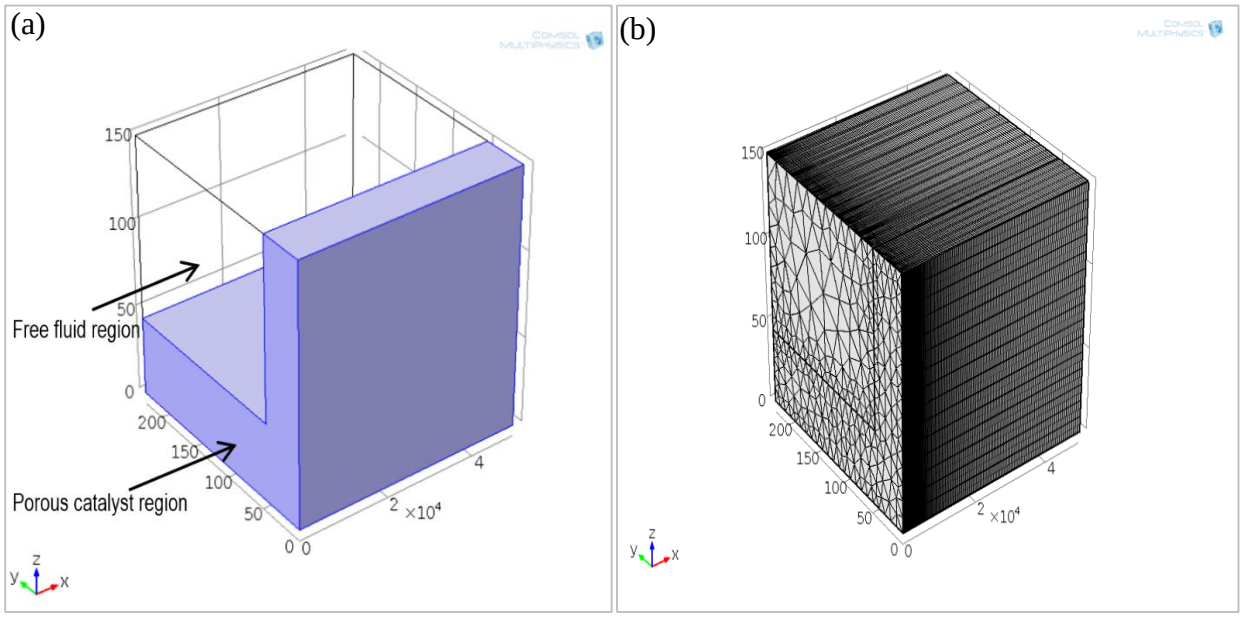

Fig. 5.1. (a) Computational domains of the simulated microchannel, and (b) discretised model geometry consisting of 75 900 prismatic elements.

5.1.3. Model assumptions

Since the 80 microchannels in the reactor are identical, it was assumed that equal partitioning of the gas flow occurs, therefore only a single microchannel is considered for modelling. Chemical reactions were only assumed to take place within the catalyst layer, and any homogeneous reactions, such as combustion, were assumed not to part take in the formation of product species.

The gas was assumed ideal, and its flow compressible (Ma < 0.3) and laminar (Re << 2 100). Temperature-dependent properties such as the gaseous heat capacities, thermal conductivities, and viscosities were estimated using correlations found in the Korean Thermophysical Property Data Bank, and calculated on an averaged molar basis for gas mixtures (CHERIC, 2020).

5.1.4. Governing equations of the CFD simulation

The CFD model used partial differential equations to describe species continuity, momentum and energy conservation within the computational domains. Mass transfer was assumed to take place both by convection and diffusion. Navier-Stokes equations described momentum conservation in the free-fluid region, while in the catalyst domain, the Brinkman-Forchheimer extended Darcy model was used. For describing diffusion, the Maxwell-Stefan diffusion model was used, which incorporated binary gas mixing coefficients. These coefficients were estimated using the Fuller-Schettler-Giddings equation (Fuller *et al*., 1966:21), and were subsequently modified for the catalyst domain using the Bruggeman correlation (Fuller *et al.*, 2009:336) to take into account the effect of the catalyst porosity.

Table 5.1. Summary of CFD model governing equations

Governing equation	**Formula**
Ideal gas law	$\rho = \frac{P}{RT} M$
Fuller-Schettler-Giddings equation	$D_{ij} = \frac{10^{-3} T^{1.75} \left(\frac{1}{M_i} + \frac{1}{M_j}\right)^{1/2}}{P_{atm}\left[\left(\sum v_i\right)^{1/3} + \left(\sum v_j\right)^{1/3}\right]^2}$
	Free-fluid region
Continuity equation	$\nabla \cdot (\rho u) = 0$
Navier-Stokes momentum equation	$u \cdot \nabla(\rho u) = -\nabla P + \nabla \cdot (\mu \nabla u)$
Species continuity equation	$u \cdot \nabla(\rho \omega_i) = \nabla \cdot (\rho D_{ij} \nabla \omega_i)$
	Porous catalyst phase
Continuity equation	$\nabla \cdot (\varepsilon \rho u) = 0$
Brinkman-Forchheimer extended Darcy equation	$u \cdot \nabla(\varepsilon \rho u) = -\nabla P + \nabla \cdot \left(\mu_{eff} \nabla u\right) - \frac{\mu}{\kappa} u - \frac{\varepsilon \rho C_F}{\sqrt{\kappa}} \lvert u \rvert u$
Species continuity equation	$u \cdot \nabla(\varepsilon \rho \omega_i) = \nabla \cdot \left(\varepsilon \rho D_{ij_{eff}} \nabla \omega_i\right) + (1 - \varepsilon) \sum a_i M_i \rho_s R_r$
Bruggeman correlation	$D_{ij_{eff}} = D_{ij} \left(\frac{T}{T_0}\right)^{1.5} \varepsilon^{1.5}$

The reaction kinetics used in the CFD model were reported by Baughman *et al*. (2012:402–403), who used a parameter estimation method to optimize the kinetic parameters in different reaction models used in fitting calculated CO conversions and selectivities to different CO PROX experimental results found in the literature (Baughman *et al*, 2012:406).

CO oxidation ($CO + ½\ O_2 = CO_2$):

$$-r_{CO} = k_C \times \exp\left(-\frac{E_C}{RT}\right) \times {C_{CO}}^{a} \times {C_{O_2}}^{b} \quad (2.21)$$

H_2 oxidation ($H_2 + ½\ O_2 = H_2O$):

$$-r_{H_2} = k_H \times \exp\left(-\frac{E_H}{RT}\right) \times {C_{O_2}}^{c} \quad (2.22)$$

Reversible WGS reaction ($CO + H_2O = CO_2 + H_2$):

$$-r_{WGS} = k_D \times \exp\left(-\frac{E_D}{RT}\right) \times \left(C_{CO}.C_{H_2O} - \frac{C_{CO_2}.C_{H_2}}{K_{eq}}\right) \quad (2.23)$$

$$K_{eq} = \exp\left(\frac{4577.8}{T} - 4.33\right) \text{ (equilibrium constant)} \quad (2.24)$$

For a Ru-based catalyst, Baughman *et al*. (2012:402–403) reported the following values:

$k_c = 1.33\ 10^6\ s^{-1}.\ (mol.m^{-3})^{-0.08}$; $k_H = 3.34\ 10^7\ s^{-1}.(mol.m^{-3})^{0.08}$; $E_H = 49.10\ kJ.mol^{-1}$;

$E_C = 35.56\ kJ.mol^{-1}$; a = 0.01; b = 1.07; c = 0.92.

The reversible WGS reaction parameters, k_D and E_D, were not reported for this catalyst. Given the importance of the WGS reaction during for a process containing CO, CO_2, H_2 and H_2O, the parameters were taken from a different study. Garbis *et al*. (2019:8) investigated CO SELMET on a Ru/Al_2O_3 catalyst, and estimated the pre-exponential constant of the WGS reaction to be $5.18\ 10^4\ m^6.s^{-1}.kg^{-1}.mol^{-1}$, corresponding to $6.45\ 10^8\ m^3.s^{-1}.mol^{-1}$ (considering Ru density = $12450\ kg.m^{-3}$). The reported activation energy was $97\ kJ.mol^{-1}$.

5.1.5. Boundary conditions

The boundary expressions imposed on the reactor model are summarised in Table 5.2. The composition of the model gas mixture was imposed at the inlet of the free-fluid region, and the

average velocity at the inlet was calculated using the volumetric flow rate through a single microchannel and its cross-sectional area. At the plane of symmetry, the normal gradient in species concentration, pressure, temperature and velocity was set to zero. A no-slip boundary condition was imposed at the walls of the channel. Continuity was assumed at the interface between the porous catalyst and the free-fluid region, and no flux was imposed in the normal direction to the reactor wall for all the gas components. Atmospheric pressure was assumed at the free-fluid outlet. At the outlet of the microchannel, the pressure was assumed to be atmospheric, with a continuity condition across the exit boundary of the free-fluid region.

Table 5.2. Summary of CFD model boundary conditions

Condition	Formula
No slip condition at the wall	$u_{wall} = 0$
Average inlet gas velocity	$u = -u_{in}.n$
Outlet pressure	$P_{out} = P_{atm}$
Symmetry plane	$n.N_i = 0$ $u.n = 0$ $K - (K.n)n = 0; K = [\mu(\nabla u + (\nabla u)^T)]n$ $-n(-k\nabla T) = 0$
Inlet mass fraction	$\omega_{in} = \omega_0$

5.1.6. Solution method

The simulation package, COMSOL Multiphysics® V4.4, was used on a computer with 16 GB DDR3 RAM, and 2.9 GHz (8 core-Intel) processor. Simulated CO conversions were calculated using a parametric sweep for the set of combinations including 6 temperatures and 4 flow rates (24 data points). The direct solver, PARDISO, was used to solve the set of differential equations defined earlier, while the relative tolerance of the solution was set to 0.01.

A subsequent parametric estimation (Table 5.3) was conducted in order to approximate the values of the kinetic rate parameters of CO oxidation and WGS, which resulted in close correlation of the model-predicted and experimental CO conversions. The Nelder-Mead optimization algorithm was used to minimize the sum of squared differences between the experimental and model-predicted

CO conversions. The relative tolerance was set as 0.01, and the maximum number of iterations was set to 1 000.

5.2. Model validation approach

This section explains the procedure followed during the estimation of the kinetic parameters. This method is similar to the one used by Ramanathan and Charma (2011:9961–9974), in which the authors did kinetic parameter estimation aimed at predicting the cold start-up emissions of an automibile exhaust, using a three-way catalyst model. Section 5.2.1 briefly describes the reasoning behind the identification of the reactions which were most relevant for the CO PROX process, and their effect at different temperature ranges (3 regimes) on the CO conversions. Section 5.2.2 explains the problem encountered while using kinetic parameters as published in Baughman *et al*. (2012:403) & Garbis *et al*. (2019:8) and motivates the need for the estimation of kinetic the most important rate parameters for the calculation of the CO conversions. The following sections (5.2.3 & 5.2.4) describe the procedure taken in the estimation of the selected kinetic parameters. Ideally, an optimization algorithm would be run, using the published parameters as initial values. However, due to the complex and non-linear nature of the model, and the possibility of multiple optima, it was necessary to start with a manual parameter estimation (Section 5.2.3). The objective of this step was to obtain a set of parameter values close enough to an optimum combination which would result in satisfactory conversions. These manually-estimated parameters were used as initial values in the Nelder-Mead regression (Section 5.2.4) in COMSOL Multiphysics® V4.4.

5.2.1. Relevant chemical reactions and the identification of three temperature-dependant reaction regimes for CO PROX

The equilibrium calculations performed using Aspen V8.6 showed that CO PROX is a process which allows secondary reactions to occur, in addition to the primary CO oxidation reaction; the secondary reactions include: reversible WGS, H_2 oxidation, CO and CO_2 methanation. Temperature is a parameter that determines the extent at which each of the reactions occur, through their kinetic rates for a specific catalyst. In this work, CO PROX was investigated in a temperature range of 80–200°C; temperatures at which the two methanation reactions have negligible effects on the conversion of CO using the Ru-Cs/Al_2O_3 catalyst. The absence of these two reactions was demonstrated during the experimental evaluation of the reactor. Therefore, for simplification, these

two methanation reactions were not included in the CFD model computations. Three reactions (CO and H_2 oxidation reactions and reversible WGS) will be used in all the simulation calculations. Since the objective of this work is abatement of the CO content of H_2-rich gas streams, the focus was set on CO conversion rather than on that of H_2.

Consider the set of experimental data points for CO conversion (Fig. 4.3), which has been overlaid with three shaded regions to indicate temperature regions at which the kinetics of the CO oxidation and WGS reactions play different roles on the overall CO conversion. The experimental CO conversions reported in Chapter 4 showed that at temperatures of 80–100°C (regime 1, Fig. 5.2), slower kinetic rates essentially limited the CO oxidation reaction, and conversions below 65% were obtained for the space velocities of 65.2–130.4 $NL.g_{cat}^{-1}.h^{-1}$. In a temperature range of 120–160°C (regime 2, Fig. 5.2; Fig. G.1, Appendix G) near-equilibrium CO conversions were obtained for all the flow rates investigated, due to sufficiently fast CO oxidation kinetics. At temperatures of 180°C and higher (regime 3, Fig. 5.2) some breakthrough was observed, as the CO conversion started decreasing following the effect of the RWGS to produce CO from large amounts of CO_2 and H_2. . Understanding the effect of each of the relevant reactions on the CO conversion in these temperature regimes assisted in the analysis during kinetic parameter estimation.

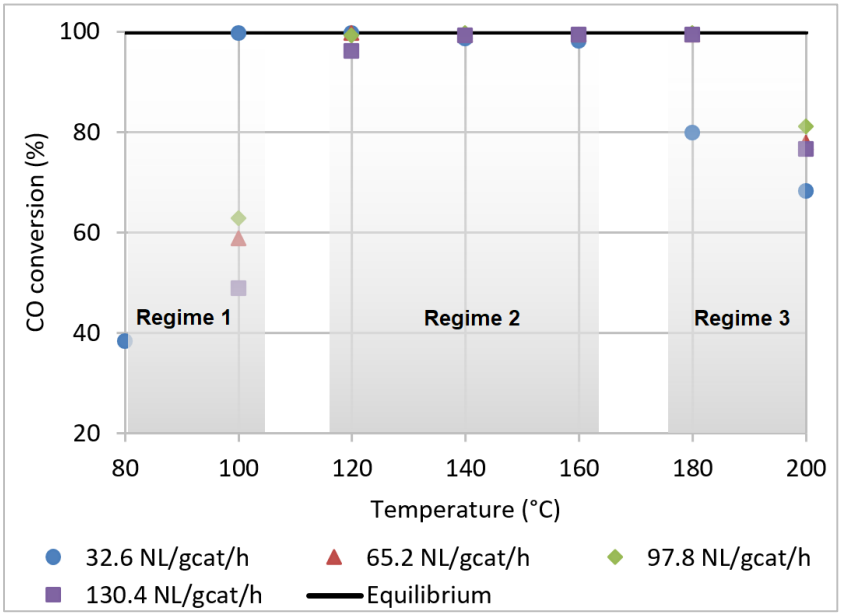

Fig. 5.2. Identification of three hypothetical temperature regimes that affect CO conversion in the experimental microchannel reactor (data representative of Section 4.3.1).

5.2.2. Published kinetic rate parameters

The reaction rate parameters reported by Baughman *et al.* (2012:403) and Garbis *et al*. (2019:8) did not accurately predict the CO conversion in the microchannel reactor in the current project. Using the set of originally published reaction rate parameters, several problems were noticed. First, the CO oxidation reaction was expressed as nearly a zero order (a = 0.01) reaction dependence on the concentration of CO. This resulted in a CO oxidation rate expression which was more dependent on the O_2 concentration than that of CO. This translated in O_2 acting as the limiting reactant in the model, whereas experimentally, CO was the actual limiting reactant. Secondly, the constants E_C and k_C (CO oxidation) resulted in less accurate predictions of low temperature CO conversion at high space velocities (regime 1 in Fig. 5.2).

The WGS parameters (E_D and k_D) found in the literature resulted in very insignificant RWGS effect. Experimental CO conversions were found to decrease above 160°C due to the influence of the RWGS reaction (regime 3 in Fig. 5.2). The RWGS rate was several orders of magnitude lower than the rate CO oxidation. This resulted in CO conversions remaining high in the model (Fig. A.1, Appendix A), while they were observed to decrease at temperatures above 160°C, experimentally.

Parameter estimation was therefore necessary for a better model fit to the experimental data, for both the reactions of CO oxidation and reversible WGS. The parameters that were considered for parameter estimation were: the CO oxidation rate order relative to CO concentration (a), the pre-exponential constants of the CO oxidation and WGS reactions (k_C and k_D), and the activation energies of the CO oxidation and WGS reactions (E_C and E_D). The rate of H_2 oxidation generally had little effect on the CO conversion (Fig. C.1, Appendix C) due to a relatively high O_2/CO ratio, 1.4. As a result, the parameters k_H, E_H and c were not considered for new parameter estimation.

5.2.3. Manual kinetic parameter estimation

Parameter estimation in non-linear models involving multiple reactions, and the regression of several parameters is a relatively complex process in which several solutions can be obtained due to the possibility of obtaining multiple optima, depending on the initial values of the parameters to be optimized (Froment *et al.*, 2011:118; Ramanathan & Charma, 2011:9961). The selection of

initial parameter values close to the optimum solution is therefore a critical step during parameter regression.

In order to better understand the effects of each of the selected parameters on the model-predicted CO conversion, a manual sensitivity analysis was performed, considering one kinetic parameter at a time. Each parameter had a different effect on the CO conversion. Parameters *a*, k_C and E_C had a noticeable impact on the CO conversion below 120°C (regime 1 in Fig. 5.2), where the experimental data was observed to be kinetically limited, and to deviate from near-equilibrium since the reaction temperature was too low. The CO oxidation rate order relative to CO concentration, *a*, was made first order, as CO was a limiting reactant and determined to rate at which the CO oxidation reaction took place in the dynamic region (length) of the microchannel. In addition, E_C, the activation energy of CO oxidation, was observed to impact the sensitivity (gradient) of CO conversion with respect to changes in reaction temperature in the low temperature region. The pre-exponential constant, k_C, was subsequently used to compensate the kinetic rate (CO turn-over rate) when changes in E_C was made.

The kinetic parameters of the reversible WGS; the activation energy, E_D, and the pre-exponential constant, k_D, significantly affected the decrease in CO conversion observed in the high temperature regime (regime 3 in Fig. 5.2) for all the space velocities investigated. As in the case of estimating the parameters for CO oxidation, the activation energy for the WGS, E_D, influenced the gradient at which the CO conversion decreases with increasing temperature, while the pre-exponential constant, k_D, was used to adjust the magnitude of the decreasing CO conversion effect. In general, the manual estimation of the rate parameters was guided by the difference between experimental and modelled CO conversions (Fig. B.1, Appendix B). Table 5.3 summarizes the effects of each of the kinetic parameters estimated in this work.

Table 5.3. Rationale for the manual estimation of kinetic parameters

Parameter	Rationale
a	- At $a = 0.01$, the CO oxidation rate could remain high, while CO concentration was very low, resulting in computational errors due to subsequent negatively calculated CO concentrations. - A higher *a* value increased the dependency of CO oxidation on the concentration of CO (CO limiting reactant). - The *a* parameter was increased to 1, close to that of the reaction order relative to O_2 concentration ($b = 1.07$).
$\mathbf{E_C}$	- E_C was modified based on the gradient of CO conversions in the low temperature range of 100–120°C. - Lower values of E_C resulted in inaccurate conversion predictions for higher space velocities at a certain temperature.
$\mathbf{k_C}$	- The k_C parameter was adjusted as a function of the change in E_C. - A change in the k_C parameter was proportional to the change in magnitude of the rate expression. - A low k_C value naturally resulted in low CO conversions for all reaction temperatures.
$\mathbf{E_D}$	- The E_D parameter was chosen to accurately describe the decreasing gradient of CO conversions in the higher temperature regime (160–200°C, regime 3 in Fig. 5.2).
$\mathbf{k_D}$	- Although the gradient of CO conversion was stronger with lower E_D values, the RWGS effect was also low at high temperature. As a result, the k_D value had to be increased, since an increase in k_D was proportional to the magnitude of the RWGS rate.

5.2.4. Nelder-Mead kinetic parameter regression

In order to find an optimal solution, further kinetic parameter optimisation was performed on four of the five manually-estimated parameters, namely: E_C, E_D, k_C, k_D. A Nelder-Mead optimisation algorithm was used, which was incorporated into the COMSOL Multiphysics® V4.4 software. To achieve parameter values as close as possible to an optimum model fit, was a pre-requisite for this non-linear optimization problem. Once the small effects of the parameters could not be estimated with higher accuracy by hand, Nelder-Mead regression was used to solve this kinetic parameter estimation problem towards an optimal solution. The kinetic parameters which were determined though the manual estimation method were used as initial values in the regression calculations.

The Nelder-Mead algorithm, which is a direct-search optimisation method, was preferred to other gradient based methods, and was used to minimize the sum of squared residuals between the model-predicted and experimental CO conversions (Eq. 5.1).

$$\min_{\theta} \sum_{g,h} [X_{gh} - \widehat{X_{gh}}(\theta)\ ]^2, \qquad (5.1)$$

where $\widehat{X_{gh}} = f(T_g, F_h|\theta)$ is the CO conversion calculated in the model using a set of estimated values of the 4 parameters θ = [E_C, E_D, k_C, k_D], while X_{gh} is the CO conversion obtained experimentally, for *g* temperatures and *h* flow rates (i.e. g = 1, 2, 3, 4, 5, 6; h = 1, 2, 3, 4).

5.3. Model results and discussion

This section reports the results obtained using the method described in 5.2. First, a comparison between published, manually-estimated and regressed parameters is tabulated in Section 5.3.1. Section 5.3.2 discusses the validation of the model with experimental data. The simulated CO conversions results follow the same trend as the one obtained experimentally in the three temperature regimes shown in Fig. 5.2. Lastly, Section 5.3.3 is a brief statement on the limitation encountered in the estimation of the goodness of fit. The sum of squared residuals between experimental and calculated CO conversions was taken as final criteria for the goodness of fit estimation.

5.3.1. Parameter estimation results

The results of the parameter estimation displayed in table 5.4 show more variation between the published and the manually-optimized parameters. Using the manually-estimated parameters instead of the published values, the model fit to the experimental data resulted in a 73.8% decrease in the sum of squared residuals.

Smaller changes were observed between the values of the manually-estimated and the regressed values. This confirms the importance of the selection of suitable initial values for the regression calculations. The Nelder-Mead regression has only refined the manually optimized values in order to obtain near-optimum parameters. As a result of the Nelder-Mead regression, a 14.6% decrease in the value of the sum of squared residuals was achieved.

Appendices A and B show compare the experimental conversions with those obtained using the published parameters and the manually-estimated parameters respectively.

Table 5.4. Results of the parameter estimation of the selected kinetic rate constants of CO oxidation and WGS reactions

Kinetic parameter	Published values	Manually-estimated values	Regressed values
a	0.01	1	No regression on *a*
$\mathbf{E_C}$ [kJ.mol^{-1}]	35.56	72.0	72.15
$\mathbf{k_C}$ [s^{-1}.(mol.m^{-3})$^{-1.07}$]	1.33 10^6	2.8 10^{11}	3.42 10^{11}
$\mathbf{E_D}$ [kJ.mol^{-1}]	97.0	74.0	74.74
$\mathbf{k_D}$ [s^{-1}.(mol.m^{-3})$^{-1}$]	6.45 10^8	2.4 10^9	2.89 10^9

5.3.2. Model validation

In this section, the CFD model of the microchannel reactor developed for CO oxidation is compared and validated on the experimental performance of the reactor described in Chapter 4. The model is compared to the experimental data, with CO conversion being the primary performance metric, for the range of reaction temperatures (100–200°C) and space velocities (32.6–130.4 NL.g_{cat}^{-1}.h^{-1}) investigated. The experimental and CFD modelling results presented in Fig. 5.3 show that the calculated CO conversions fit the experimental results with acceptable accuracy, considering the wide range of temperatures and space velocities studied. The trend in the CO conversions with increasing reaction temperature was similar to the trend observed experimentally. Kinetic limitations were the main reason for the relatively low CO conversions at temperatures below 120°C. The apparent activation energy of 72.15 kJ.mol^{-1} was higher than the one reported by Baughman *et al.* (2012:406) for the Ru/Al_2O_3 catalyst (35.56 kJ.mol^{-1}). This explains the rapid increase in CO conversion in temperature regime 1; comparing CO conversion at 120°C to that at 100°C (Fig. 5.3b–d).

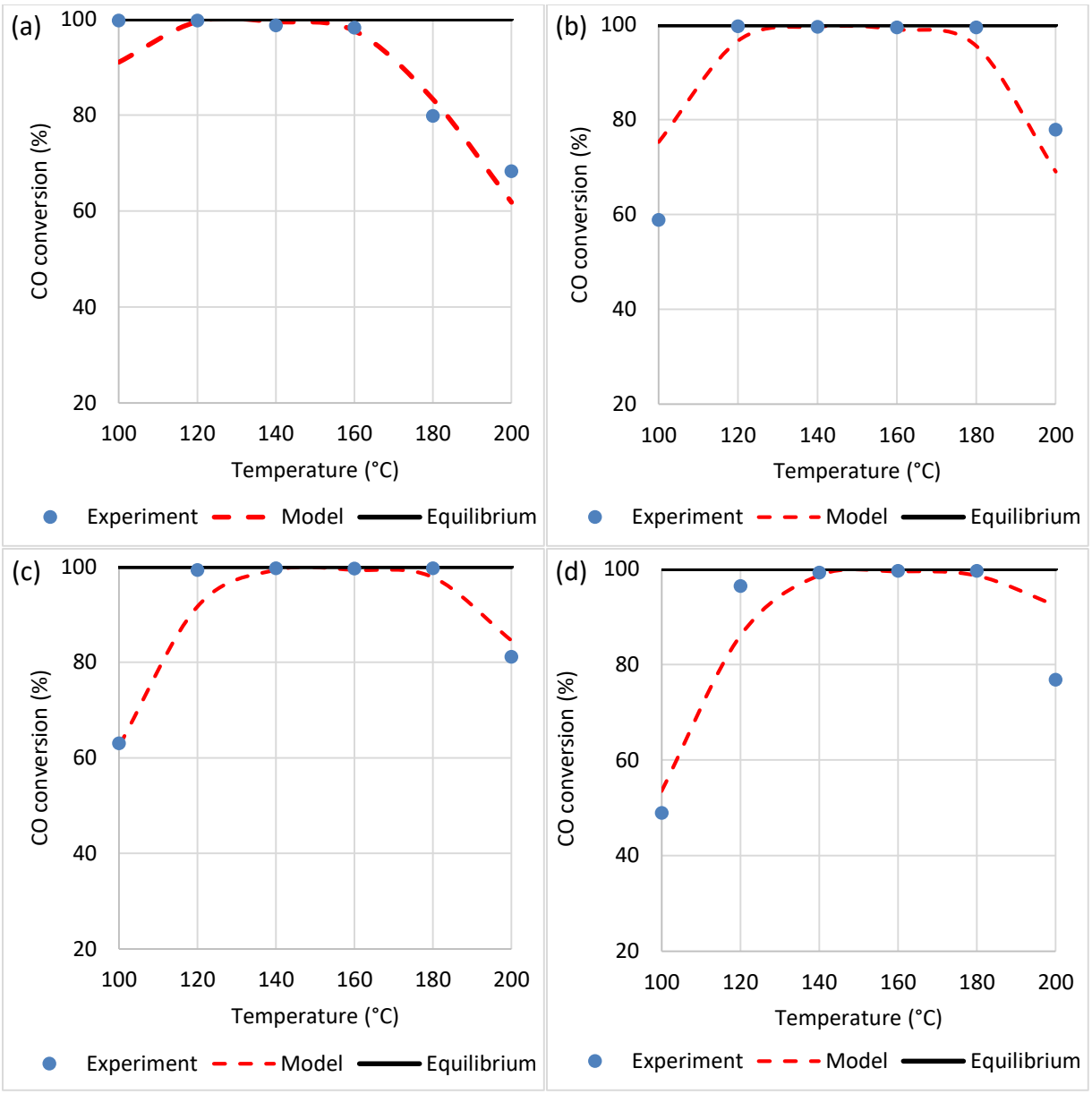

Fig. 5.3. Model validation to experimental data based on the CO conversion performance metric at space velocities of (a) 32.6, (b) 65.2, (c) 97.8 & (d) 130.4 NL.g_{cat}^{-1}.h^{-1}. Reaction temperatures range between 100 and 200°C.

The model (Fig. 5.3) also predicted high CO conversions (>90%) at temperatures between 120 and 180°C, with the exception at 120°C for the highest space velocity of 130.4 NL.g_{cat}^{-1}.h^{-1} (86.0% conversion) and at 180°C and for the lowest space velocity of 32.6 NL.g_{cat}^{-1}.h^{-1} (83.3% conversion). At these two conditions, the model deviation from high CO conversion was not unexpected, as the experimental data showed values for the CO conversion of 96.4% and 79.8%, respectively. The modelling results in this temperature range fitted most of the ones obtained

experimentally, and shows that the model could be used for the selection of suitable operating conditions of the microchannel reactor. From the model, temperatures between 140 and 180°C and space velocities between 65.2 and 97.8 $NL.g_{cat}^{-1}.h^{-1}$ could be selected as satisfactory operating conditions.

In the high-temperature regime (Fig. 5.3: 180–200°C), the model suitably predicted the effect of the RWGS reaction to produce small amounts of CO and effectively lower the CO conversion. This effect was observed for all the four space velocities investigated, especially at 200°C. Typically, the activation energy of the reversible WGS (74.74 $kJ.mol^{-1}$) has to be higher than that of the CO oxidation reaction (72.15 $kJ.mol^{-1}$), for the model to account for the stronger effect of the RWGS reaction in this high temperature range. It may be noticed that the model under-predicted (by 15.6% in the CO conversion) the strong effect of the RWGS reaction at 200°C for the highest space velocity (130.4 $NL.g_{cat}^{-1}.h^{-1}$). This was the largest discrepancy between the model-predicted CO conversion and the experimental data. It has to be taken into account that the Nelder-Mead optimisation problem considered the errors between the model-predicted values and the experimental data for all the space velocities and across the range of temperatures (100–200°C), to arrive at the minimum sum of squares solution. Considering the "rigid" set of experimental values for CO conversion across a temperature range of 100°C and a four-fold increase in the space velocities investigated, it was concluded that the microchannel model for CO PROX fits with acceptable accuracy the experimentally-evaluated reactor.

Figure 5.4a illustrates model-predicted CO conversions obtained across the evaluated temperature range and for a space velocity of 65.2 $NL.g_{cat}^{-1}.h^{-1}$, but in two scenarios for which the kinetics of the reversible WGS reaction was neglected. The first scenario considers only the CO oxidation reaction (solid line), and the second scenario both the CO and H_2 oxidation reactions (dotted line). Here, the effect of the H_2 oxidation reaction was found to be negligible on the CO oxidation reaction. This confirms that the O_2 being consumed during CO oxidation was not the limiting reactant, as it was being fed in excess to the reactor. In Fig. 5.4b, the effect of the formation of CO by the RWGS reaction is clearly illustrated, and the model-predicted CO conversions noticeably turns negative in the higher temperature range (160–200°C). The reversible WGS reaction was therefore crucial to include in the CFD model validation problem, as it resulted in the decreasing CO conversion trend observed in the higher temperature range (180–200°C) in Fig. 5.3. This

analysis was important to determine in what temperature range the two CO reactions (oxidation and RWGS) play roles, and assisted during the manual estimation of kinetic parameters, Nelder-Mead regression, and as a basis during this analysis of the interdependent three-reaction system.

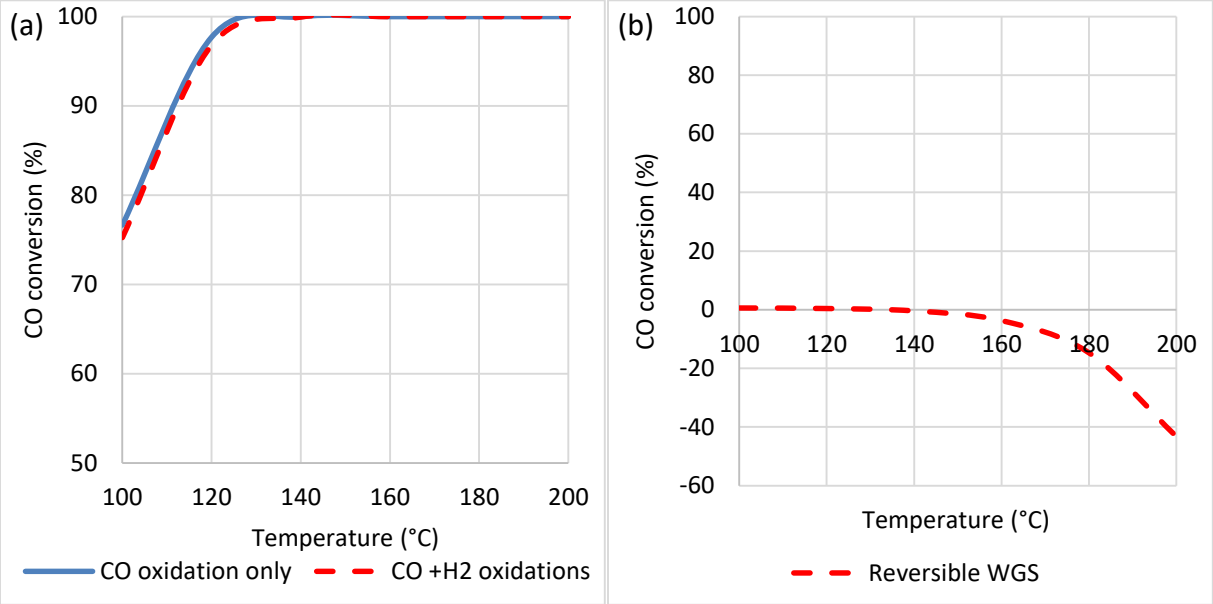

Fig. 5.4. CO conversions due to (a) CO and H_2 oxidation reactions, and (b) RWGS. The space velocity corresponds to 65.2 $NL.g_{cat}^{-1}.h^{-1}$.

5.3.3. Measure of the goodness of fit

Due to the non-linear nature of this chemical reaction engineering model, the coefficient of determination (R^2) was not appropriate for the estimation of the goodness of fit (Spiess & Neumeyer, 2010:1). An F-test could be used to estimate how adequately the model described the relationship between the CO conversion performance at different reaction temperatures and space velocities. However, according to Froment *et al.* (2011:114), when some uncertainty persists regarding the pure error sum of squares, the F-test can be calculated using the ratio of the regression residual sum of squares and the residual sum of squares. The results from applying the F-test are provided in Appendix D.

For the purpose of this work, the model output using the three different sets of kinetic parameters (published kinetics, manual estimation, and Nelder-Mead regressed parameters) were compared based on the sum of squared residuals (Table 5.5). The sum of squared residuals calculated from

the model using the Nelder-Mead regression method was found to be 77.6% lower than the sum of squared residuals calculated using the published kinetic parameters.

Table 5.5. Sum of squared residuals calculated for the CFD model using different sets of kinetic refinements to validate the model for CO PROX against the experimental data.

Set of kinetic parameters	**Sum of squared residuals**
Published parameters (Baughman *et al.*, 2010:403; Garbis *et al*., 2019:8)	4248.3
Manually-estimated parameters	1112.3
Regressed parameters (Nelder-Mead optimisation)	949.5

5.4. Transport phenomena

5.4.1. Velocity profiles

The cross-section of the simulated velocity profile (Fig. 5.5) shows a laminar, fully-developed flow at all space velocities in the free-fluid region of the channel (channel height = 45–150 μm). In the porous catalyst layer, the motion of species was expected to be mainly due to diffusion from and to the porous catalyst layer. The maximum calculated free-fluid velocities reached roughly 0.45 $m.s^{-1}$ at 32.6 $NL.g_{cat}^{-1}.h^{-1}$ and 1.9 $m.s^{-1}$ at 130.4 $NL.g_{cat}^{-1}.h^{-1}$, corresponding to residence times between 0.026 and 0.11 s. This gives an idea of the effectiveness of the microchannel reactor compared to that of conventional reactors and the rapid nature of the diffusion in the porous catalyst layer.

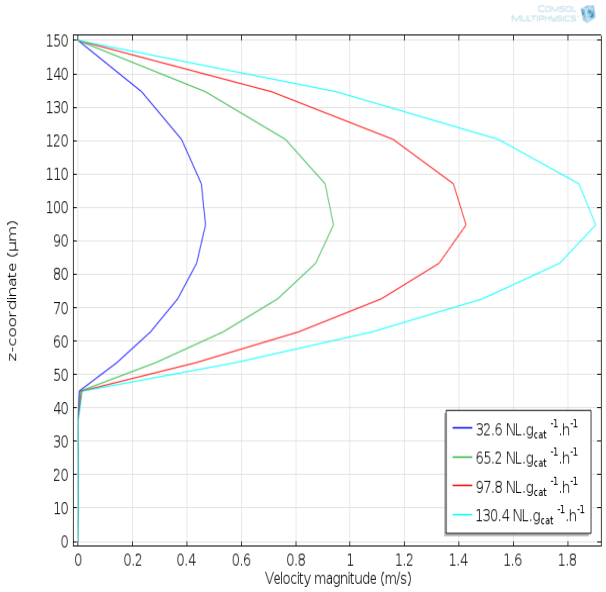

Fig. 5.5. Velocity profile along the height of the channel (z-axis) at 100°C, 4 flow rates.

In Fig. 5.6, two cross-sectional velocity profiles are illustrated for the space velocity of 65.2 $NL.g_{cat}^{-1}.h^{-1}$ and a temperature of 100°C. The velocity profiles correspond to (a) a profile along the length of the microchannel at y = 125 µm, and (b) a profile in the cross-section at x = 25 mm. It is shown (Fig. 5.6a) that the velocity in the microchannel did not vary significantly along the x-axis. This is probably due to the fact that the total number of moles in the reacting gas mixture did not vary significantly, as the initial CO content in the gas was low (1.4 vol.%), and H_2 oxidation was minimal (<6.5% conversion). The cross-sectional plot of velocity (Fig. 5.6b) is confirmation of the fully-developed flow plots observed in Fig. 5.5. Generally, velocity played an important role in the performance of the catalyst. A careful selection of the flow rate was required to enhance the conversion of CO while limiting the effects of side reactions.

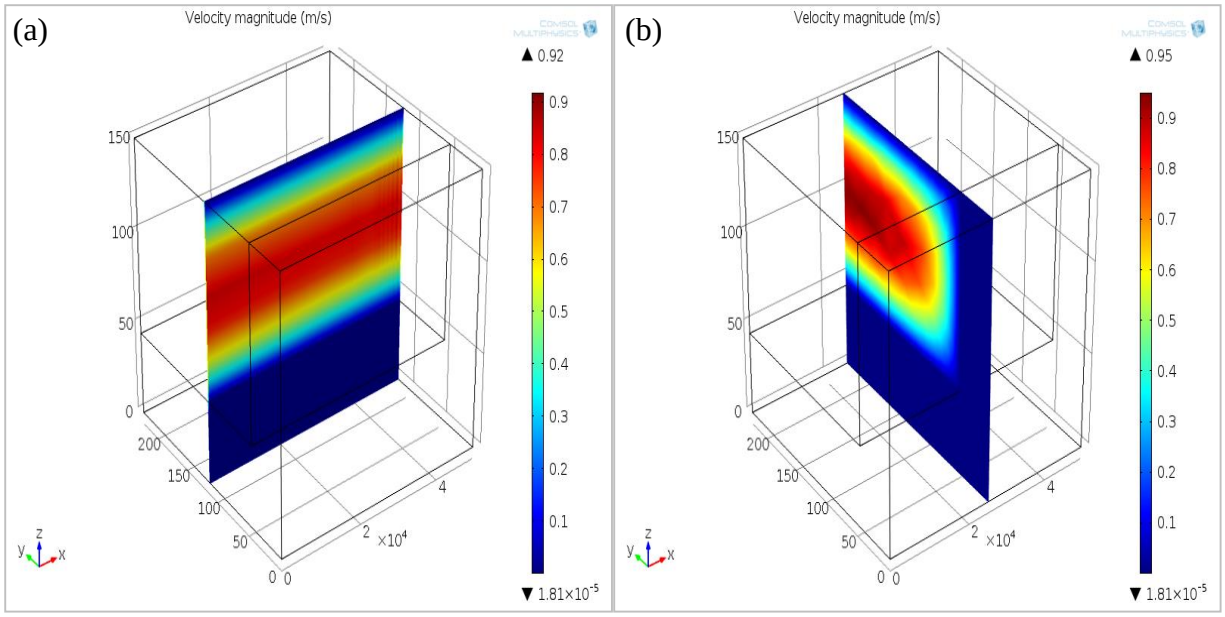

Fig. 5.6. Axial velocity profile in (a) the mid-zx and (b) mid-yz planes for a space velocity of 65.2 $NL.g_{cat}^{-1}.h^{-1}$ and a temperature of 100°C.

5.4.2. Reaction rates

Figure 5.7 shows the magnitude of the rate of the three reactions plotted against the normalized reactor length. Generally, the initial reaction rate magnitudes increased with temperature due to the Arrhenius effect. In Fig. 5.7a, the sharp decrease in the rate of CO oxidation at higher temperatures (>160°C) can be attributed to the rapid depletion of CO and O_2 in the gas mixture. The same tendency is observed more in Fig. 5.7b which shows that the H_2 oxidation rate decreases slowly between temperatures of 100 and 140°C and much faster at higher temperatures. In this case, however, the decrease is due to the depletion of O_2 only since H_2 oxidation rate depends on the O_2 molar concentration and not on that of H_2 (Eq. 2.22). In Fig. 5.7c, the negative magnitude of the WGS reaction rate indicates that the RWGS occurred at nearly all temperatures, but much more noticeably at high temperatures (i.e. 180–200°C). The RWGS reaction rate became less significant at the reactor outlet for the 200°C condition, and can be explained by the increase in water content due to both H_2 oxidation and RWGS.

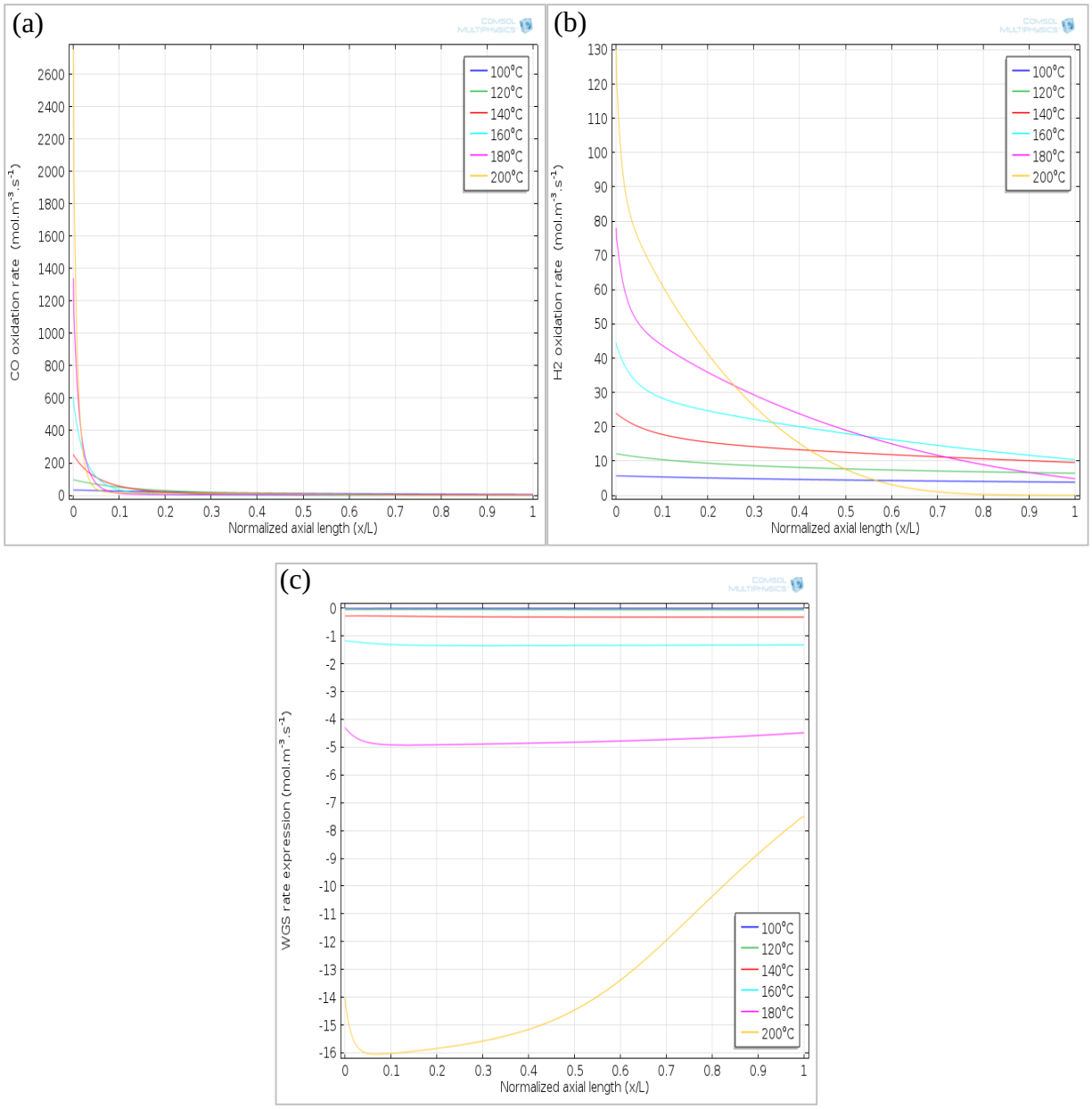

Fig. 5.7. (a) CO oxidation, (b) H_2 oxidation and (c) WGS rate profiles at different temperatures, along the length of the microchannel (Space velocity: 65.2 $NL.g_{cat}^{-1}.h^{-1}$)

From these reaction rate profiles, optimum reaction temperature range can be selected. A trade-off between maximisation of the magnitude of the CO oxidation rate and minimisation of both the rates of H_2 oxidation and RWGS could be used as a guide for the selection of the operation temperature. For instance, at 65.2 $NL.g_{cat}^{-1}.h^{-1}$, the CO conversion could be near-equilibrium between 120 and 160°C, while the H_2 oxidation rate is not yet at a maximum and the effect of the RWGS is relatively low.

5.4.3. Concentration profiles

In Figs. 5.8–5.12, axial plots show the depletion of reactants and evolution of product species within microchannel length at all six reaction temperatures, for a space velocity of 65.2 $NL.g_{cat}^{-1}.h^{-1}$. In addition, 3D profiles give an idea of the spatial concentration distribution at 200°C and the same space velocity. In Fig. 5.8a, it is noticed that for temperatures between 100 and 120°C, slower CO oxidation kinetics possibly prevent near-complete conversions within the reactor length due to limited residence time of the reactants. The CO concentration decreases throughout the reactor length since the effect of the RWGS reaction is insignificant in that temperature range. For higher reaction temperatures and at the microchannel inlet, the CO depletion rate is initially faster at temperatures higher than 160°C. In the first tenth of the microchannel length, the magnitude of the CO reaction rate was shown to increase with temperature (Fig 5.7a). As the gas pass through the downstream volume of the microchannel, the resulting outcomes vary with temperature.

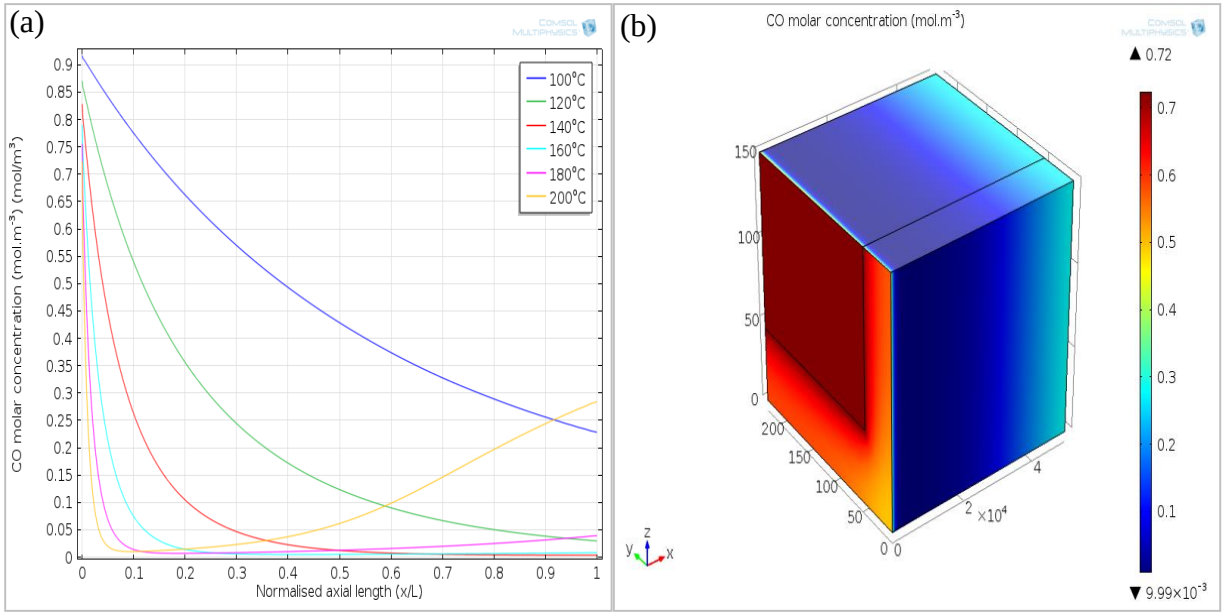

Fig. 5.8 (a) 2D plots of CO concentration profiles at 65.2 $NL.g_{cat}^{-1}.h^{-1}$ and 100–200°C; (b) 3D CO concentration distribution in the microchannel at 65.2 $NL.g_{cat}^{-1}.h^{-1}$ and 200°C

At temperatures between 140 and 160°C, maximum CO conversions were obtained within the microchannel length, and evident in the near-zero concentration of CO at the microchannel outlet. In this temperature range, theoretically CO could be converted with microchannel lengths shorter than 5 cm. At 140°C about 60% of the channel length is required in order to obtain minimum CO

outlet concentrations, whereas less than 40% of the microchannel length is needed at 160°C. The RWGS effect is still insignificant in this temperature range.

At the highest temperature studied (180–200°C), the rapid CO oxidation reaction results in near-complete CO conversions within the first tenth of the microchannel. However, the RWGS kinetics is fast enough to counteract the benefit of CO oxidation and increased the CO concentration lower down the microchannel towards the outlet. A CO molar concentration of 0.28 $mol.m^{-3}$ was obtained at the microchannel outlet for the 200°C temperature, resulting in only 69% CO conversion. Therefore, the model results suggest that the effect of the slower RWGS reaction could be limited by reducing the length of the microchannel since the CO oxidation rate is faster than that of RWGS.

From Fig. 5.8b, the same conclusion can be drawn. In this 3D plot, it is important to note the 3D concentration distribution at the inlet of the reactor. The concentration of CO is the highest in the free-fluid region and decreases along the z-axis as the gas is rapidly diffused through the porous catalyst region. In the remaining part of the reactor, the CO concentrations vary with the length of the microchannel (x-axis), but appear to be uniform along the z-axis. This is another indication of the fast rate of diffusion within the microchannel, a characteristic that arguably shows the effectiveness of the microchannel reactor.

The CO_2 concentrations along the microchannel length (Fig. 5.9a) were shown to increase at temperatures below 180°C. At 100°C, the CO_2 concentration increased more steadily than at temperatures between 120 and 180°C. At 100°C, most of the O_2 was consumed by CO oxidation, as the rate of H_2 oxidation at that temperature was still relatively low (Fig. 5.7b), with the H_2 concentration almost constant throughout the microchannel (Fig 5.10a). The plateaus observed for the CO_2 concentration between 120 and 180°C was due to the slower CO oxidation (Fig. 5.7a) of the smaller amount of CO present in the gas mixture. At 200°C, the effect of the RWGS reaction is noticeable, mostly in the second half of the microchannel, as the CO_2 concentration ultimately decreased by roughly 4% from its plateau. Fig. 5.9b shows that fast diffusion is also a key factor in the concentration distribution of CO_2 in the microchannel. Again, at 200°C, the decrease in the CO_2 concentration at the outlet of the microchannel was noticed.

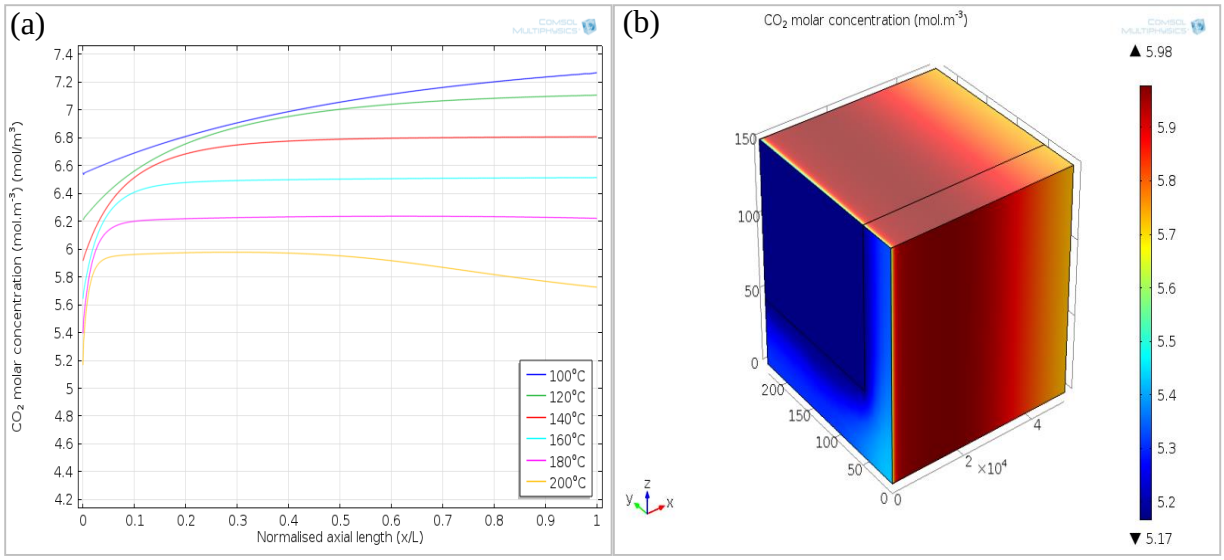

Fig. 5.9 (a) 2D plots of CO_2 concentration profiles at 65.2 NL.g_{cat}^{-1}.$h^{-1}$and 100–200°C; (b) 3D CO_2 concentration distribution in the microchannel at 65.2 NL.g_{cat}^{-1}.h^{-1} and 200°C

Figure 5.10 shows that the H_2 concentration does not decrease as significantly as that of CO as a function of the microchannel length. The advantage of minimising H_2 loss is that the energy content of the fuel is kept high. Higher temperatures increase H_2 loss by oxidation and RWGS. It is therefore important to carefully select ranges of operational temperatures in such a way as to minimise the H_2 consumption while keeping the CO conversion sufficiently high.

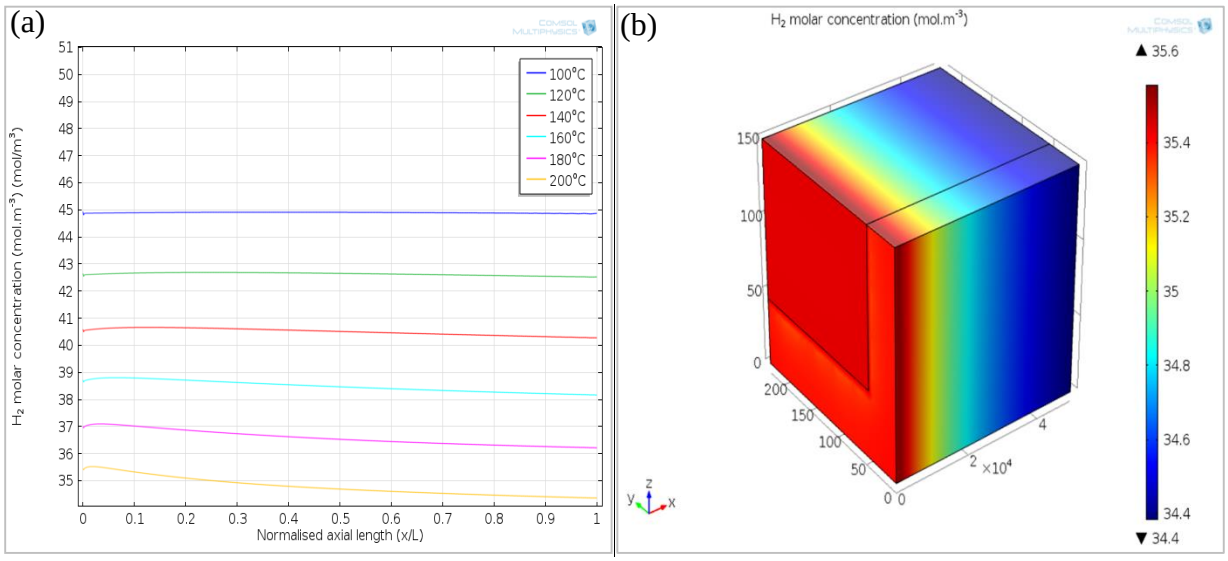

Fig. 5.10 (a) 2D plots of H_2 concentration profiles at 65.2 NL.g_{cat}^{-1}.$h^{-1}$and 100–200°C; (b) 3D H_2 concentration distribution in the microchannel at 65.2 NL.g_{cat}^{-1}.h^{-1} and 200°C

On Fig. 5.11, the O_2 content is shown to decrease more rapidly with higher reaction temperature, as the effect of H_2 oxidation (more noticeable at high temperatures) adds to that of the CO oxidation reaction. At 200°C, O_2 has almost completely reacted at 70% of the reactor length. This causes the RWGS effect to be more significant at this temperature, as more CO_2 is converted back to CO (Figs. 5.8a & 5.9a), while O_2 is absent to assist with CO oxidation.

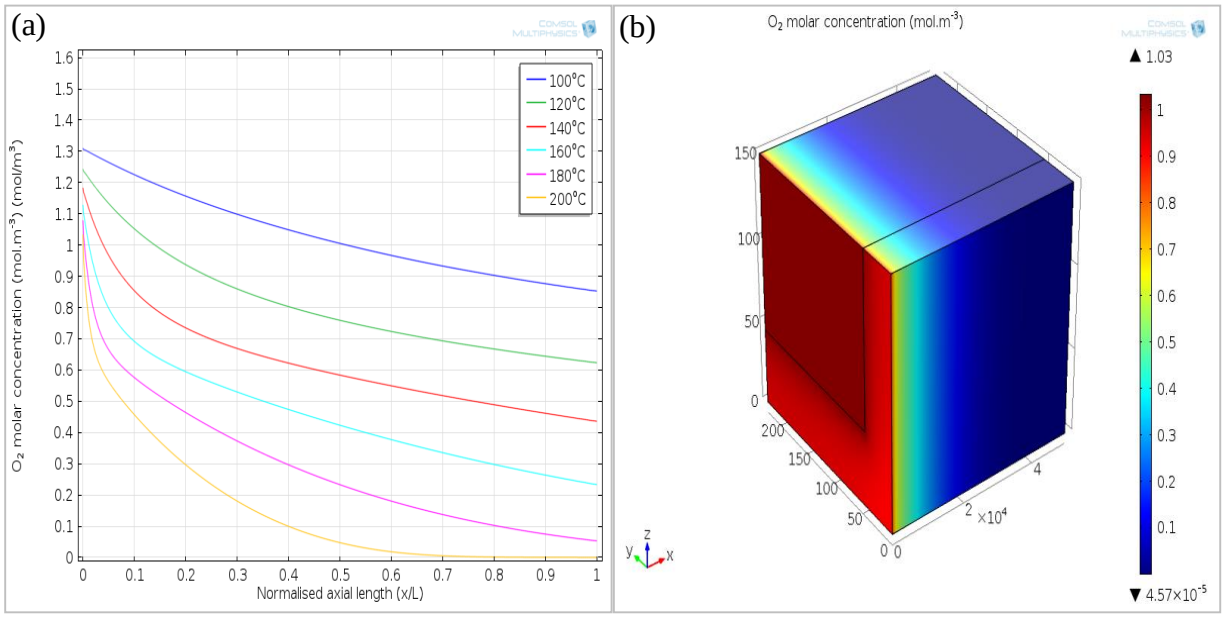

Fig. 5.11 (a) 2-D plots of O_2 concentration profiles at 65.2 NL.g_{cat}^{-1}.h^{-1} and 100–200°C; (b) 3D O_2 concentration distribution in the microchannel at 65.2 NL.g_{cat}^{-1}.h^{-1} and 200°C

The increase in H_2O content at temperatures between 100 and 140°C (Fig. 5.12a) is most probably due to the H_2 oxidation reaction only. At 180°C, since O_2 is not completely depleted in the reactor, H_2O production could be assumed to be the result of a combination of H_2 oxidation and RWGS. The O_2 depletion helps explain the slight decrease in the slope of the H_2O concentration profile in the second half of the microchannel length at 200°C. These concentration profiles can therefore be used, not only as a guide for suitable operation temperatures but also for the selection of the microchannel length.

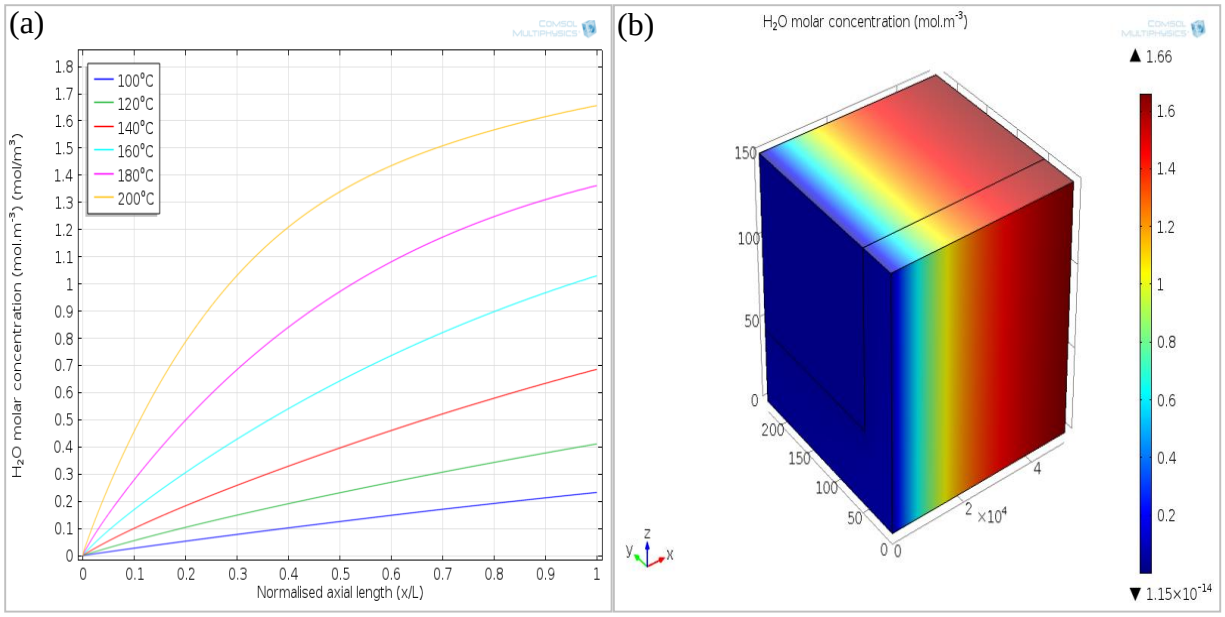

Fig. 5.12 (a) 2D plots of H_2O concentration profiles at 65.2 NL.g_{cat}^{-1}.$h^{-1}$and 100–200°C; (b) 3D H_2O concentration distribution in the microchannel at 65.2 NL.g_{cat}^{-1}.h^{-1} and 200°C

5.4.4. Pressure drop

One of the main advantages of microchannel reactors is its low pressure drop, when suitable flow rates are applied for the hydraulic diameter and length of the microchannel. Figure 5.13 shows that the pressure was almost constant throughout the channel length. The pressure drop in the microchannel was less than 0.02 atm. For processes such as pure CO_2 methanation, the pressure drop was noticed to be a bit higher at 0.054 atm (Engelbrecht, 2017b:42). A contributing factor during CO PROX is that only little amounts of CO (1.4%) and O_2 (2%) are available for reaction, and results in a small variation in the total number of moles of the reacting gas flowing in the microchannel. The small pressure drop also suggests that wall-coated microchannels support low pressure drop, rather than packed/total porous microchannel systems. Of course, the effects of external diffusion needs to be considered in wall-coated systems to make sure that mass transport between the free-fluid and the catalyst does not hinder the reaction system.

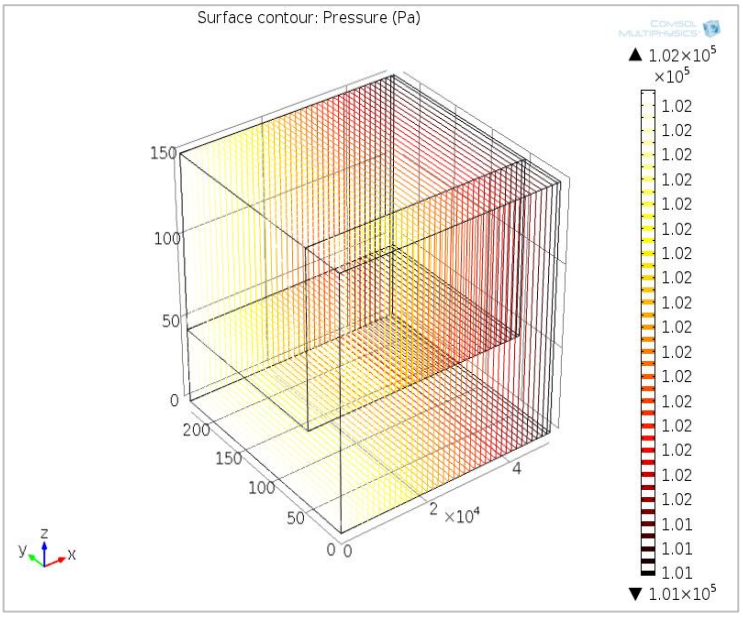

Fig. 5.13. Pressure distribution in the microchannel at 65.2 NL.g_{cat}^{-1}.h^{-1} and 200°C

CHAPTER 6. CONCLUSIONS AND RECOMMENDATIONS

This chapter summarises the major conclusions made based on the results obtained in the previous sections as well as the technical recommendations and suggestions for future research work. Section 6.1 summarises the main inferences drawn from the literature survey and the experimental results starting from the screening of the catalysts used, the experimental performance of the Ru-based catalyst and the conclusions from the CFD model. Section 6.2 completes the chapter by proposing a few conditions for successful operation during CO PROX in the microchannel reactor, and gives recommendations for future work which can contribute to a further understanding of CO PROX, both experimentally and theoretically.

6.1. Conclusions

Hydrogen is considered as a versatile energy carrier, and which could assist in mitigating CO_2 emissions in future energy systems. Cost-effective methods of H_2 production (and originating from fossil-fuel sources), such as steam reforming of natural gas and coal gasification, still constitute the largest source of H_2 produced globally. The H_2 yielded from these processes is maximised through a WGS step. However, thermodynamic limitations of the WGS reaction cause the H_2-rich gas mixture to contain between 0.5 and 2% CO, which is a compound known to decrease the durability of proton-exchange membrane fuel cells by poisoning their Pt electrodes, even at CO concentrations below 100 ppm.

The following conclusions were drawn from this work:

i. In the literature, extensive work has been performed on the topic of CO selective methanation (SELMET) and preferential oxidation (PROX). The effectiveness of the processes largely depended on the choice of the catalyst, the feed gas composition, the temperature range, the space velocity and the type of the reactor used. Microchannel reactors are a promising technology for SELMET and PROX, due to their enhanced heat and mass transfer capabilities. CFD modelling of microchannel reactors for SELMET or PROX was scarce in the literature.
ii. Of the catalysts screened in this work, the 8.5 wt.% Ru-Cs/Al_2O_3 catalyst performed better than 1.15 wt.% Au/Al_2O_3 and 4.7 wt.% Ni-Pt/Al_2O_3. The Ru-based catalyst proved to be

able to reduce the amount of CO in the H_2-rich gas from 1.4% to less than 100 ppm, by SELMET at temperatures above 380°C and PROX at temperatures between 100 and 200°C. Probable catalyst deactivation and low catalyst loading could be the causes of the poor performance observed for the Au-based and Ni-based catalysts, respectively.

iii. Of the two processes, CO PROX was selected to be the most suitable, because of the lower temperature operation (100–200°C) and higher selectivity towards CO oxidation (>99.7% CO conversion with <6.5% H_2 consumption). The relatively low reaction temperatures are close to those at which PEMFC operate (~80°C), thus decreasing the excessive need for cooling the H_2 gas. Depending on the flow rate, CO concentrations below 100 ppm were obtained in the 120–180°C temperature range, with the minimum CO concentration (42 ppm) obtained at between 120 and 140°C, at space velocities of 65.2 and 97.8 $NL.g_{cat}^{-1}.h^{-1}$, and for an O_2/CO ratio of 1.4.

iv. A CFD tool was used to describe the microchannel reactor for CO PROX, and validate the model accuracy to experimental data. Kinetic rate expressions from the literature were used to describe the oxidation reactions of CO and H_2, while it was also necessary to include a rate expression for the reversible WGS reaction. It was concluded that when the published kinetic parameters were used, the CFD model did not fit with acceptable accuracy to the experimental data. It was therefore necessary to ultimately do Nelder-Mead regression on the activation energy and pre-exponential constants for the two most important reactions for CO PROX (CO oxidation and RWGS), to accurately describe the experimental CO conversions across the range of operating parameters. It was concluded that the kinetics of CO oxidation dominated at temperatures of 100–160°C, while the RWGS reaction contributed significantly towards lower CO conversions in the 180–200°C range.

v. The CFD model was also used to characterise the CO PROX reaction and transport phenomena within the microchannels, that could not be practically described during the experimental assessment of the microchannel reactor. Velocity profiles showed that fully developed laminar flow occurred in the free-fluid region of the microchannel. Reaction rates and concentration profiles gave valuable insights into the dynamics of the three PROX reactions along the length of the microchannel. It was observed, that at different temperatures in the 100–200°C temperature range, the reaction rates and concentration profiles of the gas species present (H_2, CO, CO_2, O_2 and H_2O) varied significantly, which

contributed to the different regions of CO conversion (CO kinetic limited, equilibrium, and RWGS effect), respectively for the low, medium and high temperature regions of this particular CO PROX investigation. Lastly, the CFD results showed that microchannel length (or changes in space velocity) was a crucial factor that could be used to maximise the CO conversion, while minimising H_2 consumption and the negative effects of the RWGS reaction.

6.2. Recommendations

The following recommendations are made with regard to future work beyond the scope of this project, which will contribute to the evaluation of the CO PROX process in microchannel reactors, and other subjects of improvement emanating from this work:

i. Characterisation of the catalyst

   Determining the particle size, dispersion and oxidation state of the active metal could improve the understanding of the metallic characteristics that promote decrease the catalyst activity under demanding reactor operating conditions. Besides, temperature-programmed reduction methods should be performed on the Ru-Cs/Al_2O_3 catalyst in order to optimise the reduction temperature.

ii. Development of 8.5 wt.% Ru-Cs/Al_2O_3-specific reaction kinetics.

   Reaction kinetics play an important role in the accuracy of the model predictions. It is recommended that a kinetic study is done in order to describe the reaction kinetics for CO and H_2 oxidation, and WGS on the 8.5 wt.% Ru-Cs/Al_2O_3 catalyst as accurately as possible. This study could entail doing microkinetic modelling.

iii. Selection of other kinetic regression algorithms.

   It is recommended that other direct regression methods are investigated for models that are non-linear in their parameters, when kinetics from the literature are used.

iv. Calculation of the goodness of fit for non-linear models.

   The coefficient of determination (R^2) is known to be unsuitable for the estimation of the goodness of fit of non-linear models. Other suitable advanced statistical methods (e.g. bootstrap method) should be selected or derived, in order to better understand the accuracy of the CFD model compared to the experimental data for CO PROX.

REFERENCES

Abdel-Mageed, A.M., Widmann, D., Olesen, S.E., Chorkendorff, I. & Behm, R.J. 2018. Selective CO methanation on highly active Ru/TiO_2 catalyst: Identifying the Physical Origin of the Observed Activation/Deactivation and Loss in Selectivity. *ACS Catalysis*, 8:5399-5414.

Abu Bakar, W., Ali, R. & Toemen, S. 2012. Catalytic methanation reaction over supported nickel-ruthenium oxide base for purification of simulated natural gas. *Scientia Iranica*, 19:525-534.

Adeosun, J. & Lawal, A. 2005. Mass transfer enhancement in microchannel reactors by reorientation of fluid interfaces and stretching. *Sensors and Actuators B.* Volume 110:101-111.

Akinyele, D., Olabode, E. & Amole, A. 2020. Review of Fuel Cell Technologies and Applications for Sustainable Microgrid Systems. *Inventions,* 5(42):1-35.

Arzamendi, G.; Diéguez, P.M.; Montes, M.; Odriozola, J.A.; Sousa-Aguiar, L.M.; Gandia, L.M. 2009. Methane steam reforming in a microchannel reactor for GTL intensification: A computational fluid dynamics simulation study. *Chemical Engineering Journal,* 154:168-173.

Arzamendi, G., Uriz, I., Dieguez, P.M., Laguna, O.H., Hernandez, W.Y.; Alvarez, ... Gandia, L.M. 2011 . Selective CO removal over Au/CeFe and CeCu catalysts in microreactors studied through kinetic analysis and CFD simulations. *Chemical Engineering Journal*, 167:588-596.

Atkinson, D. & McDaniel, J. 2010. *Microchannel reactors in fuel production: A demonstration plant aims to confirm the potential for microchannel and other technologies in the distributed production of biofuels*. https://www.yumpu.com/en/document/read/32166118/microchannel-reactors-in-fuel-production-oxford-catalysts-group Date of access: 06 Nov. 2020.

Bac, S. & Avci, A. 2019. Ethylene Oxide Synthesis in a Wall-Coated Microchannel Reactor with Integrated cooling. *Chemical Engineering Journal*, 377:1-10.

Baughman, A., Huang, X. & Martin, L. 2012. Evaluating kinetic models for preferential CO oxidation catalysts using optimization based parameter estimation. *Journal of Power Sources,* 210:402-408.

Belgian Academy Council of Applied Science (BACAS). 2006. *Hydrogen as an energy carrier*. https://www.kvab.be/sites/default/rest/blobs/1125/tw_BACAS_hydrogen_as_an_energy_carrier.pdf Date of access: 06 Nov. 2020.

Bennaceur, K., Clark, B., Orr, F.M., Ramakrishnan, T.S., Roulet, C. & Stout, E. 2005. *Hydrogen: a future energy carrier?* https://pdfs.semanticscholar.org/3a43/1edc56da50328db89dd9bd8aaa447d7b0d07.pdf Date of access: 11 Jul. 2018.

Bicakova, O. & Straka, P. 2010. Resources and methods of hydrogen production. *Acta Geodynamica Geomateriala*, 7(2):175-188.

BP (British Petroleum). 2017. *BP energy outlook.* https://www.bp.com/content/dam/bp/business-sites/en/global/corporate/pdfs/energy-economics/energy-outlook/bp-energy-outlook-2017.pdf Date of access: 01 Mar. 2021.

Calla, J. & Davis, R. 2005. Influence of Dihydrogen and Water Vapor on the Kinetics of CO Oxidation over Au/Al_2O_3. *Industrial & Chemical Engineering Research*, 44:5403-5410.

Capellán-Perez, I., Mediavilla, M., De Castro, C., Carpintero, O. & Miguel, L.J. 2014. Fossil fuel depletion and socio-economic scenarios: An integrated approach. *Energy*, 77: 641-666.

Caputo, T., Lisi, L., Pirone, R. & Russo, G. 2007. Kinetics of the Preferential Oxidation of CO over CuO/CeO_2 Catalysts in H_2-Rich Gases. *Industrial Engineering Chemical Resources*, 46:6793-6800.

Castaldi, M. 2010. Removal of Trace Contaminants from Fuel Processing Reformate: Prerential Oxidation (Prox). In: K. Liu, C. Song & V. Subramani, eds. *Hydrogen and Syngas Production and Purification Technologies*. Hoboken, NJ: John Wiley, pp. 329-356.

Chaubey, R., Sahu, S., James, O. & Maity, S. 2013. A review on development of industrial processes and emerging techniques for production of hydrogen from renewable and sustainable sources. *Renewable and Sustainable Energy Reviews*, 23:433-462.

Chauhan, N. & Singh, V. 2015. Fundamentals and Use of Hydrogen as a Fuel. *Journal of Mechanical Engineering*, 6(1):63-68.

Chen, A.; Miyao, T.; Higashiyama, K.; Yamashita, H. & Watanabe, M. 2010. High Catalytic Performance of Ruthenium-Doped Mesoporous Nickel-Aluminum Oxides for Selective CO methanation. *Angewandte Chemie*, 49:9895-9898.

Chen, G., Yuan, Q., Li, H. & S., L. 2004. CO selective oxidation in a microchannel reactor for PEM fuel cell. *Chemical Engineering Journal*, 101:101-106.

Cheng, Z.; Shi, Z.; Glass, N.; Zhang, L.; Zhang, J.; Song, D.; … Shen, J. 2007. A review of PEM hydrogen fuel cell contamination: Impacts, mechanisms, and mitigation. *Journal of Power Sources*, 165:739-756.

CHERIC. 2020. *Korean Thermophysical Properties Database*. www.cheric.org Date of access: 04 Mar. 2020.

Chin, S. Y., Alexeev, O. & Amiridis, M. 2005. Preferential oxidation of CO under excess H_2 conditions over Ru catalysts. *Applied Catalysis A: General*, 286: 157-166.

Chiuta, S., Everson, R., Neomagus, H. & Bessabarov, D. 2015. Performance evaluation of a high-throughput microchannel reactor for NH_3 decomposition over a commercial Ru-based catalyst. *International Journal of Hydrogen Energy*, 40:2921-2926.

Chiuta, S., Everson, R., Neomagus, H. & Bessarabov, G. 2014a. Experimental performance evaluation of an ammonia-fuelled microchannel reformer for hydrogen generation. *International Journal of Hydrogen Energy*, 39:7225-7235.

Chiuta, S., Everson, R.C., Neomagus, H.W.J.P., Le Grange, L.A. & Bessarabov, D.G. 2014b. A modelling evaluation of an ammonia-fuelled microchannel reformer for hydrogen generation. *International Journal of Hydrogen Energy*, 39:11390-11402.

Cipti, F. & Recupero, V. 2009. Design of a CO preferential oxidation reactor for PEFC systems: A modelling approach. *Chemical Engineering Journal*, 146:128-135.

Costello, C.K., Guzman, J., Yang, J.H., Wang, Y.M., Kung, M.C., Gates, B.G. & Kung, H.H. 2004. Activation of $Au/\gamma\text{-}Al_2O_3$ catalysts for CO oxidation: characterization by X-ray absorption near structure and TPR. *The Journal of Physical Chemistry. B*, 108:12529-12536.

Cruz, S., Sanz, O., Poyato, R., Laguna, O.H., Echave, F.J., Almeida, L.C., … Odriozola, J.A. 2011. Design and testing of a microchannel reactor for the PROX reaction. *Chemical Engineering Journal*, 167:634-642.

Dagle, R. et al. 2007. Selective CO methanation catalysts for fuel processing applications. *Applied Catalysis A: General*, 326:213-218.

Danaci, S. 2017. *Optimisation and integration of catalytic porous structures into structured reactors for CO conversion to methane*. Grenoble: Université Grenoble Alpes. (Thesis – PhD).

Dehghani, A., Bridjanian, H. & Farhi, A. 2012. Selection Separation Method for Hydrogen and Light Hydrocarbons Gases from Waste-Gas Streams of a Petroleum Refinery. *Petroleum Science and Technology*, 30(21):2196-2207.

Djinovic, P., Galletti, C., Specchia, S. & Specchia, V. 2011. Ru-based catalysts for CO selective methanation reaction in H_2-rich gases. *Catalysis Today*, 164:282-287.

Dritz, T., Kuhlmann, D., Daymo, E., McDaniel, J., Federov, A. & Paul, B. 2011. *Arrayed Microchannel Manufacturing: Enabling a New Efficiency Paradigm in the Chemical and Energy Industries*. https://www.nist.gov/system/files/documents/2017/05/09/215_arrayed_microchannel_manufacturing_enabling2.pdf Date of access: 02 Nov. 2020.

Dufour, J., Serrano, D.P., Galvez, J.L., Moreno, J. & Gonzales, A. 2011. Hydrogen Production from Fossil Fuels: Life Cycle Assessment of Technologies with Low Greenhouse Gas Emissions. *Energy & Fuels*, 25:2194-2202.

Edlund, D. 2010. Hydrogen Membrane Technologies and Application in Fuel Processing. In: K. Liu, C. Song & V. Subramani, eds. *Hydrogen and Syngas Production and Purification Technologies*. Hoboken, NJ: John Wiley, pp. 357-384.

Edwards, P., Kuznetsov, V. & David, W. 2007. Hydrogen Energy. *Philosophical Transaction of the Royal Society*, 365:1043-1056.

Edwards, P., Kuznetsov, V., David, W. & Brandon, N. 2008. Hydrogen and fuel cells: Towards a sustainable energy future. *Energy Policy*, 36(12):4356-4362.

Engelbrecht, N., Chiuta, S., Everson, R.C., Neogamus, H.W.J.P. & Bessarabov, D.G. 2017a. Experimentation and CFD modelling of a microchannel reactor for carbon dioxide methanation. *Chemical Engineering Journal*, 313:847-857.

Engelbrecht, N. 2017b. *Carbon dioxide methanation in a catalytic microchannel reactor.* Potchefstroom: North-West Universtity.(Dissertation - MEng)

Estifaee, P., Haghighi, M., Mohammadi, N. & Rahmani, F. 2014. CO oxidation over sonochemically synthesized Pd-Cu/Al_2O_3 nanocatalyst used in hydrogen purification: effect of Pd loading and ultrasound irradiation time. *Ultrasonics Sonochemistry*, 21:1155-1165.

Felseghi, R-A, Carcadea, E., Raboaca, M.S., Trufin, C.N. & Filote, C. 2019. Hydrogen Fuel Cell Technology for the Sustainable Future of Stationary Applications. *Energies*, 12:1-28.

Froment, G., Bischoff, K. & De Wilde, J. 2011. *Chemical Reactor Analysis and Design.* 3rd ed. Hoboken: John Wiley & Sons.

Fuller, E., Schettler, P. & Giddings, J. C. 1966. A new method for prediction of binary gas-phase diffusion coefficients. *Industrial and Engineering Chemistry*, 58(5):19-27.

Fuller, T., Hartnig, C., Ramani, V., Uchida, H., Gasteiger, H.A., Cleghorn, S., … Bele, C. 2009. Proton exchange membrane fuel cells 9: ECS transactions: Volume 25, Issue 1. Pennington, NY: The Electrochemical Society.

Galletti, C., Specchia, S., Saracco, G. & Specchia, V. 2010. CO-selective methanation over Ru/γ-Al_2O_3 catalyst in hydrogen-rich gas for PEMFC applications. *Chemical Engineering Science*, 65:590-596.

Galletti, C., Specchia, S. & Saracco, G. S. V. 2008. CO preferential oxidation in H_2-rich gas for fuel cell applications: Microchannel reactor performance with Rh-based catalyst. *International Journal of Hydrogen Energy*, 33:3045-3048.

Galletti, C., Specchia, S. & Specchia, V. 2011. CO selective methanation in H_2-rich gas for fuel cell applications: Microchannel reactor performance with Ru-based catalyst. *Chemical Engineering Journal*, 167:616-621.

Gao, J., Chunmiao, J., Zhang, M., Gu, F., Xu, G. & Su, F. 2013. Effect of nickel nanoparticle size in Ni/Al_2O_3 on CO methanation reaction for the production of synthetic natural gas. *Catalysis Science and Technology*, 3:2009-2015.

Gao, J., Jia, C., Li, J., Zhang, M., Gu, F., Xu, G., … Su, F. 2013. Ni/Al_2O_3 catalysts for CO methanation: Effect of Al_2O_3 supports calcined at different temperatures. *Journal of Energy Chemistry*, 22:919-927.

Gao, J., Wang, W., Ping, W., Hu, D., Xu, G., Gu, F. & Su, F. 2011. A thermodynamic analysis of methanation reactions of carbon oxides for the production of synthetic natural gas. *Royal Society of Chemistry Advances*, 2:2358-2368.

Gao, Z., Cui, L. & Ma, H. 2016. Selective methanation of CO over Ni/Al_2O_3 catalyst: effect of preparation method and Ru addition. *International Journal of Hydrogen Energy*, 41:5484-5493.

Garbis, P., Kern, C. & Jess, A. 2019. Kinetics and reactor design aspects of selective methanation of CO over Ru/Al_2O_3 catalyst on CO_2/H_2 in CO/H_2 rich gases. *Energies*, 12:1-15.

Garcia, D.A., Barbanera, F., Fabrizio, C., Di Matteo, U. & Nastasi, B. 2016. Expert Opinion Analysis on Renewable Hydrogen Storage System Potential in Europe. *Energies*, 9:1-22.

Giorgi, L. & Leccese, F. 2013. Fuel Cells: Technology and Applications. *The Open Fuel Cells Journal*, 6: 1-20.

Gokhale, S., Jayaraman, V., Tayal, R. & Kulkarni, B. 2005. Microchannel reactors: Application and Use in Process Development. *International Journal of Chemical Reactor Engineering*, 3(1):1-53.

Gorke, O., Pfeifer, P. & Schubert, K. 2005. Highly selective methanation by the use of a microchannel reactor. *Catalysis Today*, 110:132-139.

Grashoff, G., Pilkington, C. & Corti, C. 1983. A review of the technology emphasising the current of palladium membrane diffusion. *Platinum Metal Review*, 27(4):157-169.

Grisel, R. & Nieuwenhuys, B. 2001. Selective Oxidation of CO, over Supported Au Catalysts. *Journal of Catalysis*, 199:48-59.

Han, Y., Kahlich, M., Kinne, M. & Behm, R. 2002. Kinetic study of selective CO oxidation in hydrogen-rich gas on a Ru/Al_2O_3 catalyst. *Physical Chemistry Chemical Physics*, 4:389-397.

Han, Y., Kinne, M. & Behm, R. 2004. Selective oxidation of CO on Ru/gamma-Al_2O_3 in methanol reformate at low temperatures. *Applied catalysis B: Environmental*, 52:123-134.

Holladay, J., Wang, Y. & Jones, E. 2004. Review of Developments in Portable Hydrogen Production Using Microreactor Technology. *Chemical Reviews*, 104(10):4767-47890.

IEA (International Energy Agency). 2019. *The Future of Hydrogen. Seizing today's opportunities*. https://webstore.iea.org/download/direct/2803 Date of access: 05 Nov. 2020.

Inoue, H. & Funakoshi, M. 1984. Kinetics of methanation of carbon monoxide and carbon dioxide. *Journal of Chemical Engineering of Japan*, 17(6):602-610.

IRENA (International Renewable Energy Agency). 2017. *REthinking Energy 2017: Accelerating the global energy transformation*. https://www.climamed.eu/wp-content/uploads/files/IRENA_REthinking_Energy_2017.pdf Date of access: 05 Nov. 2020.

IRENA (International Renewable Energy Agency). 2018. *Hydrogen from renewable power: Technology outlook for the energy transition*. https://www.irena.org/-/media/Files/IRENA/Agency/Publication/2018/Sep/IRENA_Hydrogen_from_renewable_power_2018.pdf Date of access: 05 Nov. 2020.

IRENA (International Renewable Energy Agency). 2019a. *Innovation landscape brief: Renewable Power-to-Hydrogen*. https://www.irena.org/-/media/Files/IRENA/Agency/Publication/2019/Sep/IRENA_Power-to-Hydrogen_Innovation_2019.pdf?la=en&hash=D66B06F4B4D95AA05C67DAB4DE8E2934C79858D#:~:text=WHAT%20IS%20POWER%2DTO%2DHYDROGEN,complementary%20carrier%20of%20renewable%20energy Date of access: 05 Nov. 2020.

IRENA (International Renewable Energy Agency). 2019b. *Hydrogen: A renewable energy perspective*. https://www.irena.org/-/media/Files/IRENA/Agency/Publication/2019/Sep/IRENA_Hydrogen_2019.pdf Date of access: 05 Nov. 2020.

Jensen, K. 2001. Microreaction engineering - Is small better?. *Chemical Engineering Science*, 56:201-303.

Kalamaras, C. & Efstathiou, A. 2013. *Hydrogen production technologies: Current state and future developments*. http://downloads.hindawi.com/archive/2013/690627.pdf Date of access: 05 Nov. 2020.

Kim, Y. & Park, E. 2010. The effect of the crystalline phase of alumina on the selective CO oxidation in a hydrogen-rich stream over Ru/Al_2O_3. *Applied Catalysis B: Environmental*, 96:41-50.

Kim, Y., Park, J., Lee, C. & Choi, S. P. E. 2012. Active size-controlled Ru catalysts for selective CO oxidation in H_2. *Applied Catalysis B: Environmental*, 127:129-136.

Kumar, S. & Himabindu, V. 2019. Hydrogen production by PEM water electrolysis - A review. *Materials Science for Energy Technologies*, 2:442-454.

Kung, H., Kung, M. & Costello, C. 2003. Supported Au catalysts for low temperature CO oxidation. *Journal of catalysis*, 216:425-432.

Kuznecova, I. & Gusca, J. 2017. Property based ranking of CO and CO_2 methanation catalysts. *Energy Procedia*, 128:255-260.

Laguna, O.H., Hernandez, W.Y., Arzamendi, G., Gandia, L.M., Centeno, M.A. & Odriozola, J.A. 2014. Au supported on CuO_x/CeO_2 for the purification of hydrogen by the CO preferential oxidation reaction (PROX). *Fuel*, 118:176-185.

Laguna, O.H., Ngassa, E.M., Oraa, S., Alvarez, A., Dominguez, M.I., Romero-Saria, F., ... Odrizola, J.A. 2012. Preferential oxidation of CO (CO-PROX) over CuO_x /CeO_2 coated microchannel reactor. *Catalysis Today*, 180:105-110.

Lambert, M. 2018. Power-to-Gas: Linking Electricity and Gas in a Decarbonizing World. *Oxford Energy Insight*, 39:1-17.

Lazdans, A., Dace, E. & Gusca, J. 2016. Development of the experimental scheme for methanation process. *Energy Procedia*, 95:540-545.

Lee, C.-B., Cho, S.-H., Lee, D.-W., Hwang, K.-R., Park, J.-S. & Kim, S-H. 2014. Combination of preferential CO oxidation and methanation in hybrid MCR for CO clean-up. *Energy*, 78:421-425.

Lerou, J.J., Tonkovich, A.L., Silva, L., Perry, S. & McDaniel, J. 2010. Microchannel reactor architecture enables greener processes. *Chemical Engineering Science*, 65:380-385.

Le, T.A., Kim, S.M., Lee, S.H., Kim, T.W. & Park, E.D. 2017. CO and CO_2 methanation over supported Ni catalysts. *Catalysis Today*, 293-294:89-96.

Li, D., Zhu, Y., Wang, H. & Ding, Y. 2013. Nanoporous gold as an active low-temperature catalyst towards CO oxidation in hydrogen-rich streams. *Scientific Reports 3*. 3015:1-7

Li, Q., He, R., Gao, J.-A. & Jensen, J. 2003. The CO Poisoning Effect in PEMFC Operational at Temperatures up to 200°C. *Journal of the Electrochemical Society*, 150(12):A1599-A1605.

Liu, K., Song, C. & Subramani, V. 2010. *Hydrogen and Syngas Production and Purification Technologies*. Hoboken: John Wiley & Sons.

Liu, Q., Dong, X. & Lin, W. 2009. Highly Selective CO methanation over amorphous Ni-Ru-B/ZrO_2 catalyst. *Chinese Chemical Letters*, 20:889-892.

Liu, Q., Dong, X. & Liu, Z. 2014a. Performance of Ni/Nano-ZrO_2 catalyst for CO Preferential Methanation. *Chinese Journal of Chemical Engineering*, 22(2):131-135.

Liu, Q., Gu, F., Lu, X., Liu, Y., Li, H., Zhong, Z., …Fabing, S. 2014b. Enhanced performances of Ni/Al_2O_3 catalyst via addition of V_2O_3 for CO methanation. *Applied Catalysis A*, 488:37-47.

Liu, Q., Dong, X., Mo, X. & Lin, W. 2008. Selective catalytic methanation of CO in hydrogen-rich gases over Ni/ZrO_2 catalyst. *Journal of Natural Gas Chemistry*, 17:268-272.

Liu, Y. & Hinrichsen, O. 2014. CFD simulation of hydrodynamics and methanation reactions in a fluidized-bed reactor for the production of synthetic natural gas. *Industrial & Engineering Chemistry Research*, 53:9348-9356.

Liu, Z., Chu, B., Zhai, X., Jin, Y. & Cheng, Y. 2012. Total methanation of syngas to synthetic natural gas over Ni catalyst in a micro-channel reactor. *Fuel*, 95:599-605.

Manorahan, Y., Hosseini, S.E., Butler, B.L., Alzhahrani, H., Senior, B.T.F., Ashuri, T. & Krohn, J. 2019. Hydrogen Fuel Cell Vehicles; Current Status and Future Prospects. *Applied Sciences*, 9:1-17.

Marino, F., Descorme, C. & Duprez, D. 2004. Noble metal catalyst for preferential oxidation of carbon monoxide in the presence of hydrogen. *Applied Catalysis B: Environmental*, 54:59-66.

Men, Y., Kolb, G., Zapf, R., Hessel, V. & Lowe, H. 2007. Selective methanation of carbon oxides in a microchannel reactor - Primary screening and impact of gas additives. *Catalysis Today*, 125:81-87.

Miao, Y., Shi, L., Sun, Q. & Li, W. 2016. A highly efficient potassium-treated Au-Cu/Al_2O_3 catalyst for the preferential oxidation of carbon monoxide. *Royal Society of Chemistry*, 6:24603-24609.

Midilli, A., Ay, M., Dincer, I. & Rosen, M. 2005. On hydrogen and hydrogen energy strategy I.: Current status and needs. *Renewable and Sustainable Energy Reviews*, 9:255-271.

Mishra, A. & Prasad, R. 2011. A Review on Preferential Oxidation of Carbon Monoxide in Hydrogen Rich Gases. *Bulletin of Chemical Reaction Engineering & Catalysis*, 6(1):1-14.

Mohaideen, K., Kim, W., Koo, K. & Yoon, W. 2015. Highly dispersed Ni particles on Ru/NiAl catalyst derived from layered hydroxides for selective CO methanation. *Catalysis Communication*, 60(2015):8-13.

Moharana, M., Peela, N., Khandekar, S. & Kunzru, D. 2009. *Producing Hydrogen from Ethanol in a Microfuel Processor: Recent Developments and Challenges*. Paper delivered at 6th International Symposium on Multiphase Flow, Heat Mass Transfer and Energy Conversion, Xi'an. http://home.iitk.ac.in/~samkhan/Bio_data/publications/Khandekar_Conf_17.pdf Date of access: 05 Nov.2020

Ndlovu, I.M., Everson, R.C., Chiuta, S., Neogamus, H.W.J.P., Langmi, H.W., Ren, J., Engelbrecht, N. & Bessabarov, D. 2018. A Performance Evaluation of a Microchannel Reactor for the Production of Hydrogen from Formic Acid for Electrochemical Energy Applications. *International Journal of Electrochemical Science*, 13:485-497.

Noda, Z., Hirata, K., Hayashi, K., Takahashi, T., Nakazato, N., Saigusa, K., … Sasaki, K. 2017. Hydrogen pump-type impurity sensors for hydrogen fuels. *International Journal of Hydrogen Energy*, 42:3281-3293.

Nordio, M., Rizzi, F., Manzolini, G., Mulder, M., Raymakers, L., Annaland, M.V.S. & Gallucci, F. 2019. Experimental and modelling study of an electrochemical hydrogencompressor. *Chemical Engineering Journal*, 369:432-442.

O'Connell, M., Kolb, G., Schelhaas, K.-P., Wichert, M., Tiemann, D., Pennemann, H. & Zapf, R. 2012. Towards mass production of microstructured fuel processors for application in future distributed energy generation systems: A review of recent progress at IMM. *Chemical Engineering Research and Design*, 90:11-18.

Office of Energy Efficiency and Renewable Energy. 2020. *Hydrogen Production: Photobiological*. https://www.energy.gov/eere/fuelcells/hydrogen-production-photobiological Date of access: 30 Jul. 2018.

Ojeda, M., Zhan, B. & Iglesia, E. 2012. Mechanistic interpretation of CO oxidation turnover rates on supported Au clusters. *Journal of Catalysis*, 285:92-102.

Owens, B. & McGuiness, J. 2016. GE-Fuel Cells. *The Power of Tomorrow*. https://nanopdf.com/download/ge-fuel-cells-the-power-of-tomorrow_pdf Date of access: 06 Nov. 2020.

Panagiotopoulou, P., Kondarides, D. & Verikyos, X. 2008. Selective methanation of CO over supported noble metalcatalysts: Effects of the nature of the metallic phase on the catalytic performance. *Applied Catalysis A*, 344:45-54.

Panagiotopoulou, P., Kondarides, X. & Verykios, X. 2009. Selective methanation of CO over supported Ru catalysts. *Applied Catalysis B: Environmental*, 88:470-478.

Park, E., D., L. & Lee, H. 2008. Recent progress in selective CO removal in H_2-rich stream. *Catalysis Today*, 139:280-290.

Pasierb, P. & Rekas, M. 2011. High-Temperature Electrochemical Hydrogen Pumps and Separators. *International Journal of Electrochemistry*. 2011:1-10.

Qi, Z., He, C. & Kaufman, A. 2002. Effect of CO in the anode fuel on the performance of PEM fuel cell cathode. *Journal of Power Sources,* 111:239-247.

Ramanathan, K. & Charma, C. 2011. Kinetic Parameters Estimation for Three Way Catalyst Modeling. *Industrial & Engineering Chemistry Research,* 50:9960-9979.

Riis, T., Hagen, E., Vie, P. & Ulleberg, O. 2006. *Hydrogen Production and Storage: RD priorities and gaps*. http://ieahydrogen.org/pdfs/Special-Reports/Hydrogen_Gaps_and_Priorities.aspx Date of access: 05 Nov. 2020.

Ritchie, H. & Roser, M., 2018. *Renewables*. https://ourworldindata.org/renewables#global-renewable-energy-consumption-over-the-long-run Date of access: 30 July 2018.

Rosso, I., Massimiliano, A., Galletti, C., Saracco, G. & Specchia, V. 2004. Selective CO-oxidation over Ru-based catalysts in H_2 -rich gas for fuel cell applications. *Topics in Catalysis*, 30/31(1-4):475-480.

Rouge, A., Spoetzl, B., Gebauer, K., Schenk R. & Renken, A. 2001. Microchannel reactors for fast periodic operation: the catalytic dehydration of isopropanol. *Chemical Engineering Science*, 56:1419-1427.

Roy, S., Bauer, T. & Al-Dahhan, M. 2004. Monoliths as Multiphase Reactors: A Review. *Reactor, Kinetics, and Catalysis*, 50(11):2918-2938.

SBC Energy Institute. 2013. *Electricity Storage*. http://files.energystorageforum.com/SBC_Energy_Institute_Electricity_Storage%20Factbook_vf.pdf Date of access: 05 Nov. 2020

Sethuraman, V. & Weidner, J. 2010. Analysis of Sulfur Poisoning on a PEM Fuel Cell Electrode. *Electrochimica Acta,* 55(20):5683-5694.

Shafiee, S. & Topal, E. 2009. When will fossil fuel reserves be diminished? *Energy Policy*, 37:181-189.

Shreenag, U., Rakesh & Raj, M.A.L.A. 2015. Bio-hydrogen production in microbial electrolysis cell using waste water from sugar industry. *International Journal of Engineering Sciences & Research Technology*, 4(4):452-458.

Sircar, S. & Golden, T. 2010. Pressure Swing Adsorption Technology for Hydrogen Production. In: K. Liu, C. Song & V. Subramani, eds. *Hydrogen and Syngas Production and Purification Technologies*. Hoboken, NJ: John Wiley, pp. 414-450.

Snytnikov, P.V., Potemkin, D.I., Rebrov, E.V., Sobyanin, V.A., Hessel, V. & Shouten, J.C. 2010. Design, scale-out, and operation of a microchannel reactor with a Cu/CeO_{2-x} catalytic coating for preferential CO oxidation. *Chemical Engineering Journal*, 160:923-929.

Snytnikov, P.V., Sobynanin, V.A., Belyaev, V.D., Tsyrulnikov, P.G., Shitova, N.B. & Shlyapin, D.A. 2003. Selective oxidation of carbon monoxide in excess hydrogen over Pt-, Ru- and Pd-supported catalysts. *Applied Catalysis A: General* , 239:149-156.

Soliman, N. 2019. Factors affecting CO oxidation over nanosized materials: A review. *Journal of Material Research and Technology*, 8(2):2395-2407.

Song, C. 2010. Introduction to Hydrogen and Syngas Production and Purification Technologies. In: K. Liu, S. Chunshan & V. Subramani, eds. *Hydrogen and Syngas Production and Purification Technologies*. Hoboken, NJ: John Wiley, pp. 1-13.

Srinivas, S., Dhingra, A., Im, H. & Gulari, E. 2004. A scalable silicon microreactor for preferential CO oxidation: performance comparison with a tubular packed-bed reactor. *Applied Catalysis A*, 274:285-293.

Sun, L., Luo, K. & Fan, J. 2018. Production of synthetic natural gas by CO methanation over Ni/Al_2O_3 catalyst in a fluidized bed reactor. *Catalysis Communications*, 105:37-42.

Tada, S., Kikuchi, R., Urasaki, K. & Satokawa, S. 2011. Effect of reduction pretreatment and support materials on selective CO methanation over supported Ru catalysts. *Applied Catalysis A: General*, 404:149-154.

Tada, S., Kikuchi, R., Wada, R., Osada, K., Akiyama, K., Satokawa, S. & Kawashima, Y. 2014. Long-term durability of Ni/TiO_2 and $Ru-Ni/TiO_2$ catalysts for selective CO methanation. *Journal of Power Sources*, 264:59-66.

Tomasic, V. & Jovic, F. 2006. State-of-the-art in the monolithic catalysts/reactors. *Applied Catalysis A: General* , 311:112-121.

Tonkovich, A., Kuhlmann, D., Rogers, A., McDaniel, J., Fitzgerald, S., Arora, R. & Yuschak, T. 2005. Microchannel technology scale-up to commercial capacity. *Chemical Engineering Research and Design*, 83:634-639.

Uriz, I., Arzamendi, G., Dieguez, P.M., Laguna, O.H., Centeno, M.A., Odriozola, J.A. & Gandia, L.M. 2013. Preferential oxidation of CO over $Au/CuO_x–CeO_2$ catalyst in microstructured reactors studied through CFD simulations. *Catalysis Today*, 216:283-291.

Wang, X., Baker, P., Zhang, X., Garces, H.F., Bonville, L.J., Pasaogulari, U. & Molter, T.M. 2014. An experimental overview of the effects of hydrogen impurities on polymer electrolyte membrane fuel cell performance. *International Journal of Hydrogen Energy*, 39:19701-19713.

Weidner, E., Cebolla, O. & Davies, J. 2019. *Global deployment of large capacity stationary fuel cells - Drivers of, and barriers to,stationary fuel cell deployment* https://publications.jrc.ec.europa.eu/repository/bitstream/JRC115923/jrc115923_stationary_fuel_cells_16042019_final_pubsy_online.pdf Date of access: 05 Nov. 2019

Xu, C., Su, J., Xu, X., Liu, P., Zhao, H., Tian, F. & Y., Ding. 2007. Low Temperature CO Oxidation over Unsupported Nanoporous Gold. *Journal of American Chemical Society*, 129:42-43.

Xu, G. & Zhang, Z.-G. 2006. Preferential CO oxidation on Ru/Al_2O_3 catalyst: An investigation by considering the simultaneously involved methanation. *Journal of Power Sources*, Volume 157:64-77.

Xu, J. & Froment, G. 1989. Methane Steam Reforming, Methanation and Water-Gas Shift: I. Intrinsic Kinetics. *American Institute of Chemical Engineers Journal*, 35(1):88-96.

Yao, X., Zhang, Y., Du, L., Liu, J. & Yao, J. 2015. Review on the application of microreactors. *Renewable and Sustainable Energy Reviews*, 47:519-539.

Zhu, H., Ma, Z., Clark, J.C., Pan, Z., Overbury, S.H. & Dai, S. 2007. Low-temperature CO oxidation on Au/fumed SiO_2-based catalysts prepared from $Au(en)_2Cl_3$ precursor. *Applied Catalysis A: General*, 326:89-99.

Zou, X., Qi, S., Suo, Z., An, L. & Li, F. 2007. Activity and deactivation of Au/Al_2O_3 catalyst for low-temperature CO oxidation. *Catalysis communications*, 8:784-788.

Zou, X., Qi, S., Xu, J., Suo, Z., An, L. & Li, F. 2010. Study on Au/Al_2O_3 catalysts for low-temperature CO oxidation in situ FT-IR. *Journal of Natural Gas Chemistry*, 19:307-312.

APPENDIX

Appendix A. CO conversions obtained using published reaction rate parameters (Baughman *et al.*, 2010:403 and Garbis *et al.*, 2019:8)

The following conversions were calculated using published reaction rate parameters. Inaccurate predictions of CO conversions can be noticed both in the low- and high-temperature ranges. Optimizing parameters of the CO oxidation and RWGS was necessary in order to improve the model predictions.

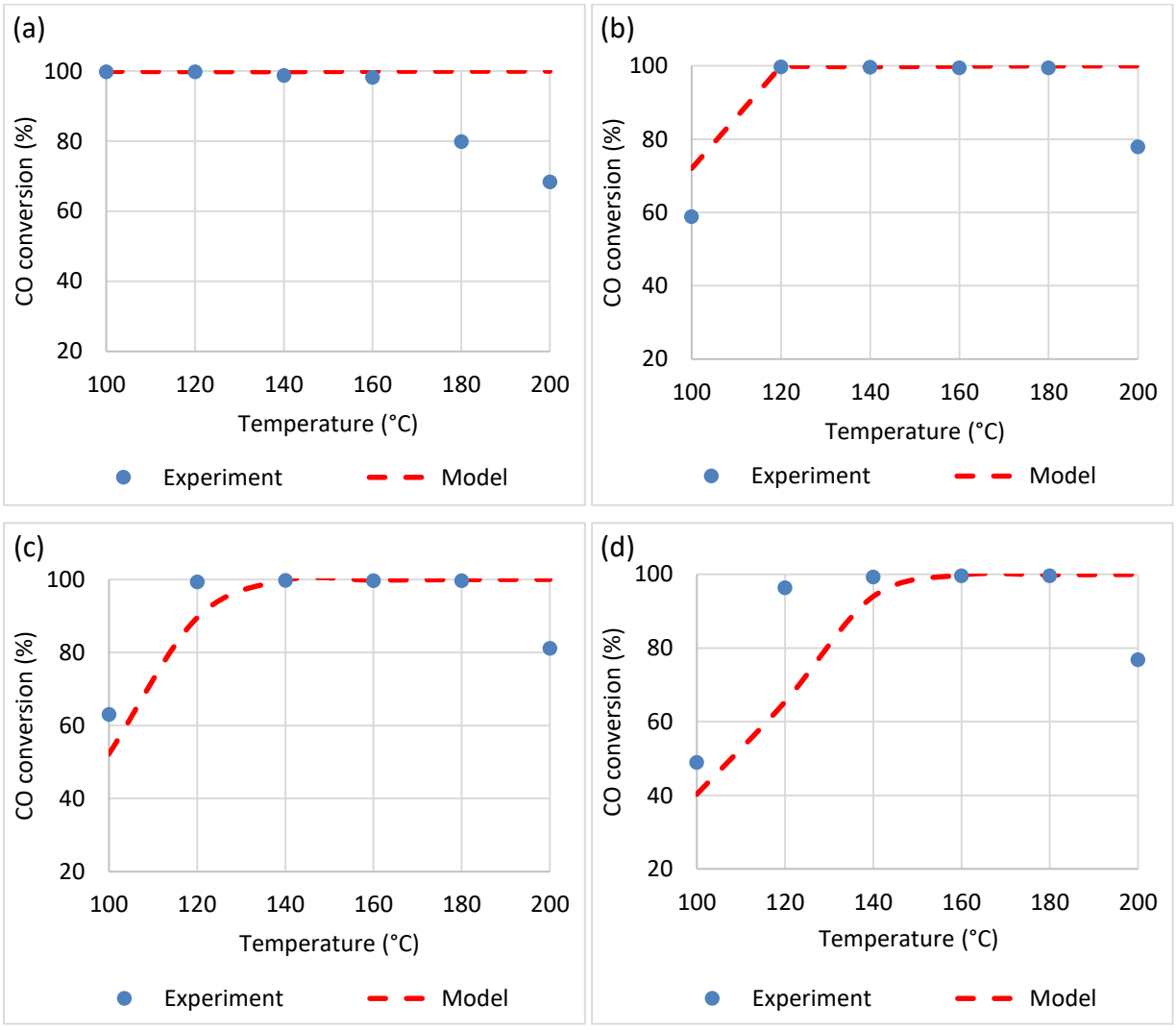

Fig. A.1. Comparison between experimental CO conversions and those calculated using parameters published by Baughman et al. (2010:403) and Garbis et al. (2019:8). Space velocities (a) 32.6, (b) 65.2, (c) 97.8 and (d) 130.4 NL.g_{cat}^{-1}.h^{-1}.

Appendix B. CO conversions calculated using manually-estimated parameters

The CO conversions calculated using parameters modified manually resulted in a decrease in the sum of squared residuals. These parameters were used as initial values in the Nelder-Mead regression in COMSOL Multiphysics® 4.4.

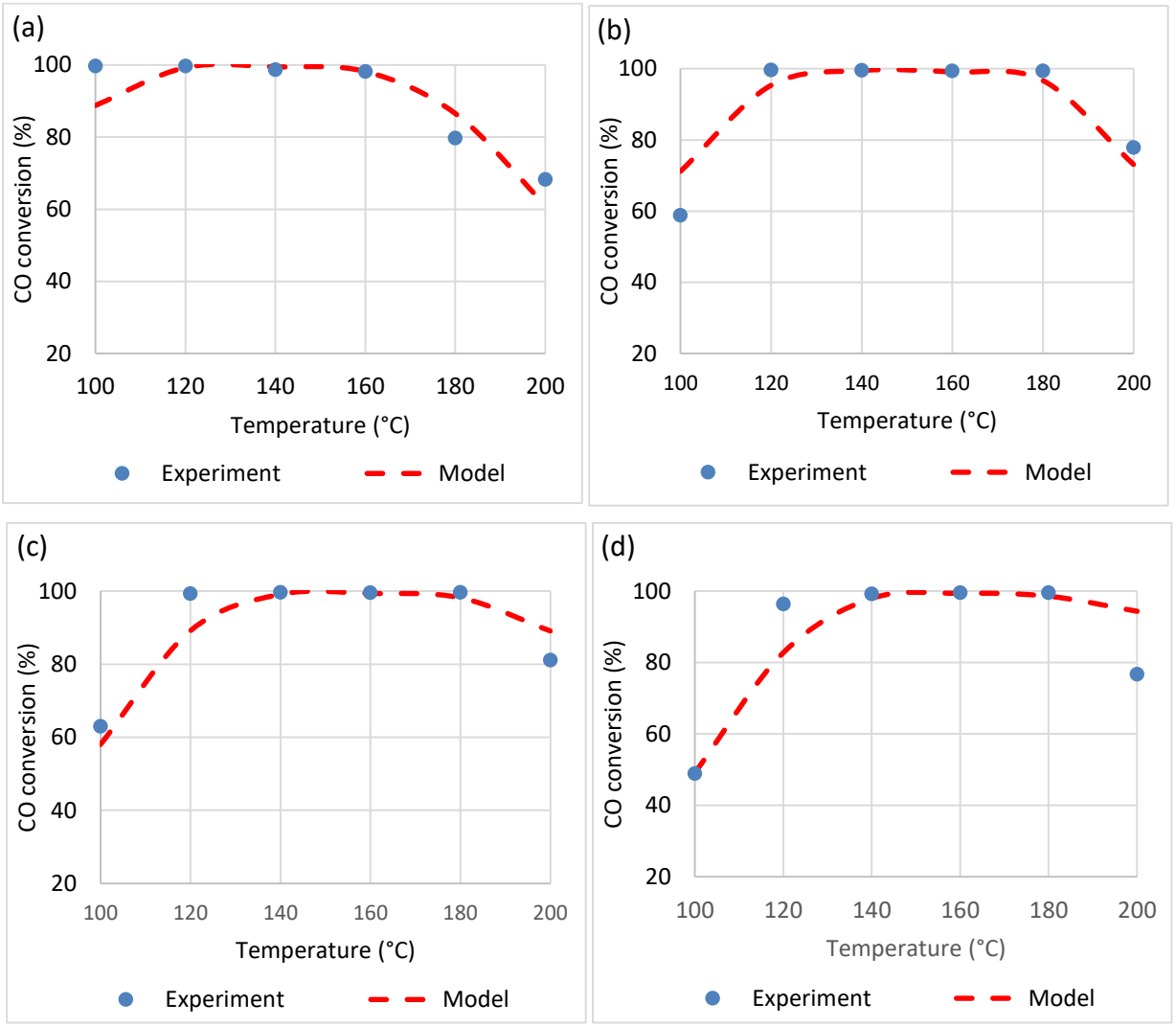

Fig. B.1. Comparison between experimental CO conversions and those calculated using manually-estimated parameters.
Space velocities (a) 32.6, (b) 65.2, (c) 97.8 and (d) 130.4 NL.g_{cat}^{-1}.h^{-1}.

Appendix C. CO conversions calculated from using CO and H_2 oxidations only, neglecting the RWGS reaction.

From Fig. C.1, it can be deduced that the effect of the H_2 oxidation on CO conversion is insignificant and that RWGS reaction is responsible for the decrease in CO conversions at higher temperatures (i.e. >160°C, depending on the space velocity).

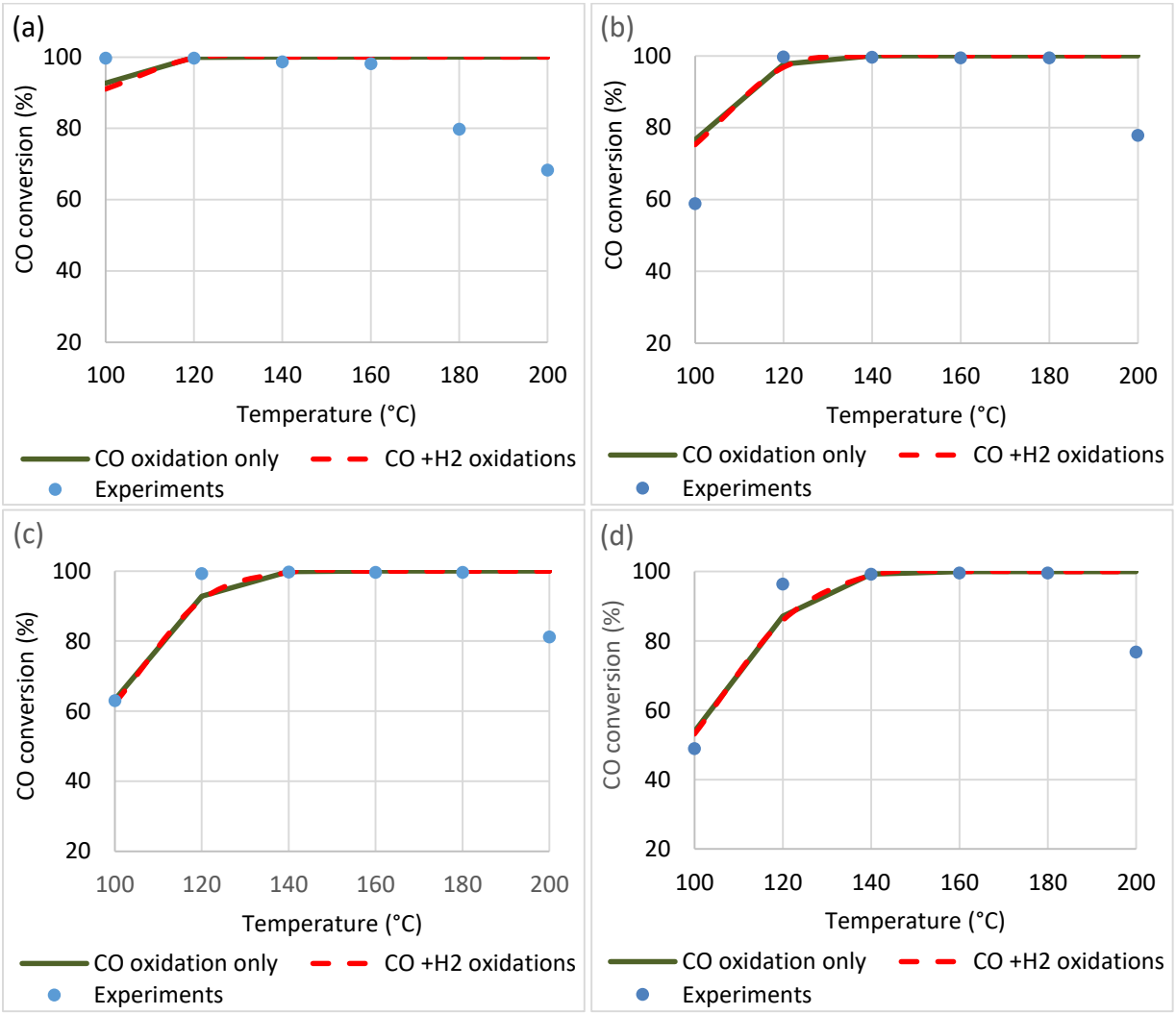

Fig. C.1. Comparison between experimental CO conversions and those calculated CO oxidation only and a combination of CO and H_2 oxidations, while neglecting the RWGS reaction. Space velocities (a) 32.6, (b) 65.2, (c) 97.8 and (d) 130.4 $NL.g_{cat}^{-1}.h^{-1}$.

Appendix D. Attempt to estimate the goodness of fit using F-test

Model formulation

Suppose the relationship between CO conversions (*X*), temperatures (*T*) and flow rates (*F*) can be described by:

$$X_{g,h} = f(T_g, F_h|\theta) + e_{g,h}$$

where: g = 1,…6; h = 1,…4,

θ = [E_C, E_D, k_C, k_D],

$e_{g,h}$ are uncorrelated normally distributed errors with constant variance.

If $\hat{\theta}$ is the value θ which minimizes the sum of squared residuals, then the residuals are defined by:

$$e_{g,h} = X_{g,h} - \hat{X}_{g,h},$$

where:

$$\hat{X}_{g,h} = f(T_g, F_h|\hat{\theta}).$$

Goodness-of-fit test

In order for the F-test to be applied to the model results, the residuals ($e_{g,h}$) must be uncorrelated, normally distributed, having a zero-mean and constant variance.

The decision to decide whether the model is significant, is based on the following test statistic (Froment *et al.*, 2010:122):

$$F^* = \frac{\sum_g \sum_h \left(\hat{X}_{g,h} - \bar{X}_{g,h}\right)^2 / p}{\sum_g \sum_h \left(X_{g,h} - X_{g,h}\right)^2 / (n-p)} \sim F(p, n-p),$$

where:

- $F(p, n-p)$ is the asymptotic null distribution of F^*.

- $\bar{X}_{g,h}$ is the mean of observations $X_{g,h}$.
- *n* is the number of experiments (24) and *p*, the number of parameters (4).

The following hypotheses are tested:

- H_0: $The\ model\ does\ not\ describe\ the\ relationships\ adequately$
- H_a: $The\ model\ does\ describe\ the\ relationships\ adequately$

The term "relationship" refer to the nonlinear relationship that exist between conversion, temperature and flow rate.

If the realized value of the test statistic F^* is larger than the $(1-\alpha)$ quantile of this distribution (p-value < α), the null hypothesis is rejected and the fitted model is adequate. Considering a 95% confidence level (α = 0.05), the results of this test can be found in the table below.

Table D.1. Results of the F-test for the optimized model

Residual sum of squares	**Regression sum of squares**	F^* **statistic**	**p-value**
949.5	4560.65	24.02	$2.79\ 10^{-7}$

Where:

- $residual\ sum\ of\ squares = \sum_g\ \sum_h\ \left(X_{g,h} - \hat{X}_{g,h}\right)^2$
- $regression\ sum\ of\ squares = \sum_g\ \sum_h\ \left(\hat{X}_{g,h} - X_{g,h}\right)^2$

To test whether these assumptions are true, model diagnostics need to be done. For example, to test whether errors $\epsilon_{g,h}$ are uncorrelated and have constant variance, the residuals $e_{g,h}$ can be plotted against temperature T_g as shown in Fig. D.1.

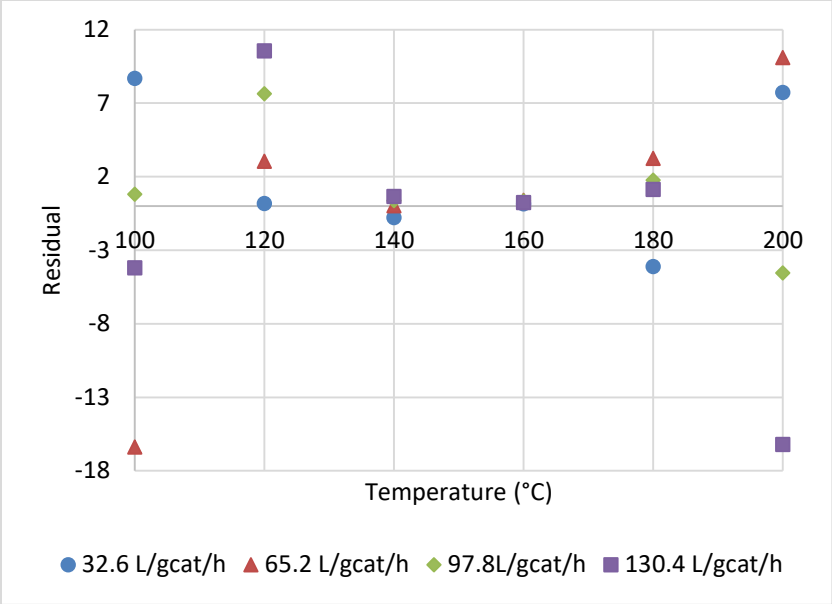

Fig.D.1. Residuals plotted against reaction temperature of 100–200°C for space velocities of 32.6–130.4 NL.g_{cat}^{-1}.h^{-1}

From this plot, it is clear that the variance is not constant and that residuals depend on temperature. Therefore, the assumptions are not true, and this has a negative impact on the trustworthiness of the goodness of fit results.

Conclusion

Due to the nonlinearity of the model as well as the assumptions that are not met, the comparison between the sums of squared residuals (Table D.2) is a more reliable method for choosing the best model.

Table D.2. Comparison between residual sum of squares for the different parameters used in the model

Models	**Residual sum of squares**
Published parameters	4248.3
Manually estimated parameters	1112.3
Regressed parameters	949.5

Appendix E. Three-dimensional plots for CO conversion

The following 3D plots were generated in Excel, using the experimental CO conversions as well as those calculated in the CFD model. From these plots, specific combinations of operational parameters (temperature and space velocity) can be selected to maximize the CO conversion.

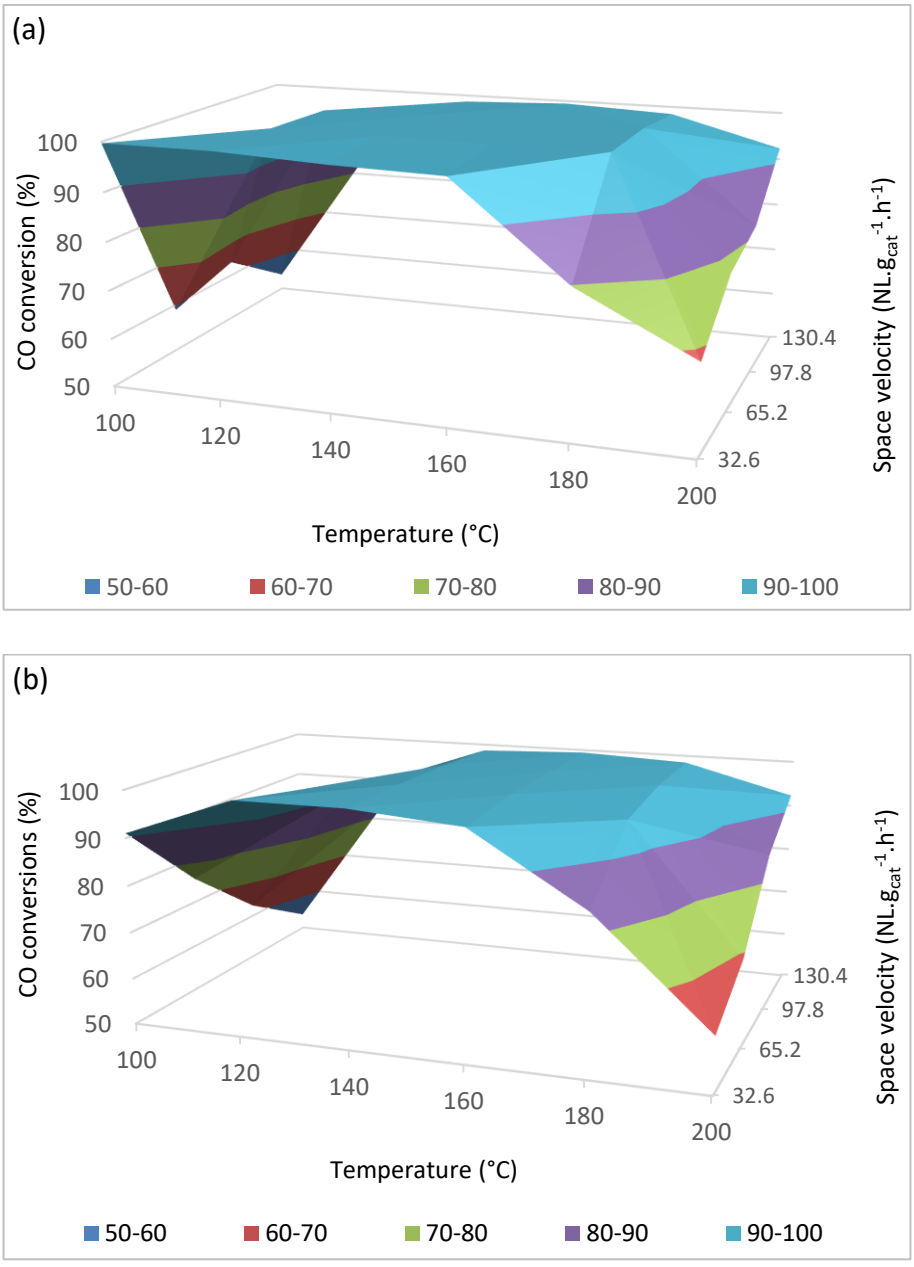

Fig. E.1. 3D plots showing the dependence of (a) the experimental CO conversions (b) simulated CO conversions on the space velocity and temperature.

Appendix F. Tabulated of experimental CO, H_2 conversions, CO product concentrations and selectivities

Tables F.1, F.2, F.3 and F.4 present respectively the values of the CO conversions, CO outlet concentrations, H_2 conversions and CO selectivities calculated or measured during CO PROX experiments. These data are tabulated versions of Figs 4.3, 4.4, and 4.5.

Table F.1. Tabulated experimental CO conversions for all space velocities and temperatures considered in this study

CO conversion (%)				
Temperature (°C)	**32.6 $NL.g_{cat}^{-1}.h^{-1}$**	**65.2 $NL.g_{cat}^{-1}.h^{-1}$**	**97.8 $NL.g_{cat}^{-1}.h^{-1}$**	**130.4 $NL.g_{cat}^{-1}.h^{-1}$**
80	38.5	-	-	-
100	99.7	58.9	63.0	48.9
120	99.7	99.7	99.3	96.4
140	98.7	99.6	99.7	99.2
160	98.2	99.4	99.6	99.6
180	79.8	99.5	99.7	99.6
200	68.3	77.9	81.1	76.8

Table F.2. Tabulated experimental CO product concentrations for all space velocities and temperatures considered in this study

CO outlet concentration (ppm)				
Temperature (°C)	**32.6 $NL.g_{cat}^{-1}.h^{-1}$**	**65.2 $NL.g_{cat}^{-1}.h^{-1}$**	**97.8 $NL.g_{cat}^{-1}.h^{-1}$**	**130.4 $NL.g_{cat}^{-1}.h^{-1}$**
80	9004.3	-	-	-
100	45.2	5826.3	5118	6990.0
120	44.0	41.4	96.1	501.5
140	195.8	56.6	42.2	106.0
160	273.3	79.7	51.8	55.9
180	3033.5	77	47.5	61.4
200	4782	3207.8	2698.2	6990.0

Table F.3. Tabulated experimental H_2 conversions for all space velocities and temperatures considered in this study

H_2 conversion (%)				
Temperature (°C)	**32.6 $NL.g_{cat}^{-1}.h^{-1}$**	**65.2 $NL.g_{cat}^{-1}.h^{-1}$**	**97.8 $NL.g_{cat}^{-1}.h^{-1}$**	**130.4 $NL.g_{cat}^{-1}.h^{-1}$**
80	3.44	-	-	-
100	5.57	1.94	-0.14	-0.75
120	5.52	2.07	-0.06	0.96
140	5.81	3.36	1.57	1.65
160	5.76	2.48	0.63	2.51
180	5.35	4.39	2.36	2.81
200	6.50	3.98	2.39	3.57

Table F.4. Tabulated experimental CO selectivities for all space velocities and temperatures considered in this study

CO selectivity (%)				
Temperature (°C)	**32.6 $NL.g_{cat}^{-1}.h^{-1}$**	**65.2 $NL.g_{cat}^{-1}.h^{-1}$**	**97.8 $NL.g_{cat}^{-1}.h^{-1}$**	**130.4 $NL.g_{cat}^{-1}.h^{-1}$**
80	18.6	-	-	-
100	25.2	39.2	26.1	25.7
120	27.0	50.3	44.7	41.5
140	25.8	37.9	37.3	39.7
160	25.9	46.1	34.9	35.1
180	23.4	31.8	35.0	34.8
200	17.7	28.7	28.6	25.7

Appendix G. Comparison between highest CO conversions and the calculated equilibrium conversions

The following graphs illustrates how close the experimental CO conversions came to the equilibrium conversions at different temperatures. Despite the optimum reactor conditions used, the combination of the effects of the CO oxidation and RWGS reaction kinetics caused the high CO conversions not to reach equilibrium values.

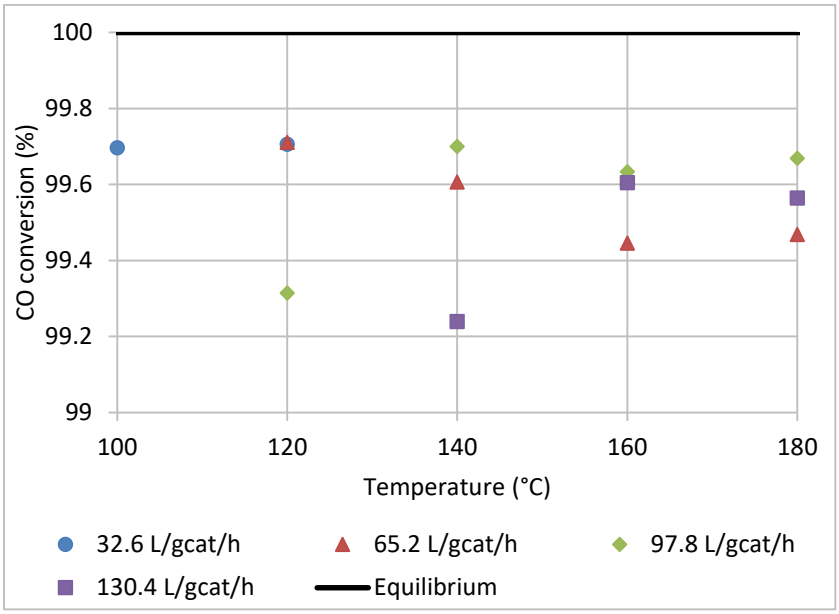

Fig. G.1. Comparison between equilibrium and highest experimental CO conversions